



**Australian Government**  
**Department of Defence**  
Defence Science and  
Technology Organisation

# **Coherent Change Detection: Theoretical Description and Experimental Results**

*Mark Preiss and Nicholas J. S. Stacy*

Intelligence, Surveillance and Reconnaissance Division  
Defence Science and Technology Organisation

**DSTO-TR-1851**

## **ABSTRACT**

This report investigates techniques for detecting fine scale scene changes using repeat pass Synthetic Aperture Radar (SAR) imagery. As SAR is a coherent imaging system two forms of change detection may be considered, namely incoherent and coherent change detection. Incoherent change detection identifies changes in the mean backscatter power of a scene typically via an average intensity ratio change statistic. Coherent change detection on the other hand, identifies changes in both the amplitude and phase of the transduced imagery using the sample coherence change statistic. Coherent change detection thus has the potential to detect very subtle scene changes to the sub-resolution cell scattering structure that may be undetectable using incoherent techniques. The repeat pass SAR imagery however, must be acquired and processed interferometrically. This report examines the processing steps required to form a coherent image pair and describes an interferometric spotlight SAR processor for processing repeat pass collections acquired with DSTO Ingara X-band SAR. The detection performance of the commonly used average intensity ratio and sample coherence change statistics are provided as well as the performance of a recently proposed log likelihood change statistic. The three change statistics are applied to experimental repeat pass SAR data to demonstrate the relative performance of the change statistics.

**APPROVED FOR PUBLIC RELEASE**

*Published by*

*Defence Science and Technology Organisation*

*PO Box 1500*

*Edinburgh, South Australia 5111, Australia*

*Telephone: (08) 8259 5555*

*Facsimile: (08) 8259 6567*

*© Commonwealth of Australia 2006*

*AR No. 013-634*

*August, 2006*

***APPROVED FOR PUBLIC RELEASE***

# Coherent Change Detection: Theoretical Description and Experimental Results

## EXECUTIVE SUMMARY

In this report techniques for detecting fine scale scene changes using repeat pass spotlight Synthetic Aperture Radar (SAR) imagery are examined. Change detection is an application to which SAR is particularly well suited since SARs can consistently produce high quality fine resolution imagery from multiple repeat pass collections. Furthermore the precise flight track measurements necessary for synthetic aperture formation allows imagery to be acquired with good radiometric and geometric calibration as well as good geolocation accuracy.

As SAR is a coherent imaging system two forms of change detection may be considered, namely incoherent and coherent change detection. Incoherent change detection identifies changes in the mean backscatter power of a scene. Typically the average image intensity ratio of the image pair is computed to detect such changes. Coherent change detection on the other hand, identifies changes in both the amplitude and phase of the transduced imagery that arise in the interval between collections. The sample coherence of the image pair is commonly used to quantify such changes. As the SAR image amplitude and phase are sensitive to changes in the spatial distribution of scatterers within a resolution cell, coherent change detection has the potential to detect very subtle scene changes that may remained undetected using incoherent techniques. In order to realise the full potential of coherent change detection however, SAR imagery must be acquired and processed interferometrically. In particular the image pair must be acquired with careful control of the repeat pass imaging geometries. Furthermore additional processing steps are required to model, estimate and compensate for any mismatch between the SAR acquisition functions and image formation processors employed to form the primary and repeat image pair.

This report describes the processing steps required to form a coherent image pair suitable for interferometric processing. In particular imaging collection constraints are discussed and the various sources of image decorrelation present in a repeat pass image pair are described and quantified. A practical interferometric SAR processor for processing repeat pass collections obtained from the DSTO Ingara X-band SAR is described. Results from a change detection experiment conducted with Ingara are given in which changes, possibly due to the movement of sheep, are presented.

The theoretical detection performance of the incoherent average image intensity ratio and the sample coherence are quantified in terms of receiver operator curves (ROC) i.e., the probability of detection plotted against probability of false alarm. A third recently proposed coherent log likelihood change statistic is described and its theoretical detection performance is shown to be superior to the commonly used average image intensity ratio and the sample coherence.

The three change statistics are applied to two different experimental repeat pass SAR collections each with controlled scene changes created using a rotary hoe and lawn mower. In the first collection the repeat pass delay is 24 hours and for a false alarm rate of 1 in 20 the probability of detecting the rotary hoe changes is 0.23 in the sample coherence image

and 0.71 in the log likelihood ratio image. The changes are also detected in the averaged image intensity ratio image with a probability of detection of 0.42. The second collection was acquired over a different scene with a repeat pass delay of 2 hours. In this experiment the rotary hoe changes are only detected in the sample coherence and log likelihood ratio change images. For a false alarm rate of 1 in 55 the probability of detection in the sample coherence image is 0.3 and in the log likelihood change image it is 0.68. Theoretical and simulated ROC plots for the two experimental cases show that for a fixed probability of detection of 0.7 the log likelihood change statistic has approximately an order of magnitude lower false alarm rate than the sample coherence. The improved detection performance of the log likelihood change statistic is a step towards robust computer assisted exploitation of coherent change detection data.

# Authors

## Mark Preiss

*Intelligence, Surveillance and Reconnaissance Division*

Mark Preiss received the B.E. (Hons) and Ph.D. degrees in electrical engineering from the University of Adelaide, Adelaide, Australia, in 1994 and 2004, respectively. From 1994 to 1996, he was with the Communications Division of the Australian Defence Science and Technology Organisation (DSTO), working on HF modem design and testing. Since 1996 he has been with the Imaging Radar Systems group at the DSTO supporting the ongoing development of the Ingara X-band Synthetic Aperture Radar (SAR) and conducting research into imaging radar techniques. His research interests include SAR image formation, interferometric change detection techniques and multi-channel/multibaseline interferometric SAR.

---

## Nicholas J. S. Stacy

*Intelligence, Surveillance and Reconnaissance Division*

Nick Stacy received the B.E. (Hons), M.S. and Ph.D. degrees in electrical engineering from the University of Adelaide in 1984, Stanford University in 1985 and Cornell University in 1993 respectively. From 1985 to 1986 he was with the National Astronomy and Ionosphere Center at Arecibo Observatory and from 1987 to 1989 with British Aerospace Australia. His work included the acquisition and analysis of Arecibo Observatory radar observations of the Moon and the analysis of Arecibo and Magellan radar data of Venus. He joined the Australian Defence Science and Technology Organisation (DSTO) in 1993 where he has worked in the field of imaging radar processing and analysis primarily using the Ingara airborne radar system. He was the Australian sensor lead for the Global Hawk deployment to Australia in 2001 and currently leads the Imaging Radar Systems group. His research interests include the signal processing and analysis of polarimetric and interferometric imaging radar.

---

# Contents

<b>1</b>	<b>Introduction</b>	<b>1</b>
<b>2</b>	<b>Spotlight SAR Image Formation</b>	<b>3</b>
2.1	SAR Data Acquisition and Range Processing . . . . .	3
2.2	The Polar Format Algorithm . . . . .	6
2.3	Comments on the PFA . . . . .	12
<b>3</b>	<b>Spotlight SAR Interferometry</b>	<b>13</b>
3.1	Forming an Interferometric Image Pair . . . . .	14
3.2	Interferometric Processing Modes . . . . .	16
3.3	Processing Effects . . . . .	20
3.3.1	Receiver Noise Decorrelation . . . . .	21
3.3.2	Baseline Decorrelation . . . . .	21
3.3.3	Registration . . . . .	23
3.3.4	Higher Order Effects . . . . .	24
3.4	A Model for a Repeat Pass Image Pair . . . . .	24
3.5	A Practical Interferometric Processor . . . . .	25
3.5.1	Compute Acquisition Apertures of Support . . . . .	25
3.5.2	Determine the Common Overlapping Aperture of Support . . . . .	26
3.5.3	Image Formation . . . . .	26
3.5.4	Image Pair Registration . . . . .	27
3.5.5	Interferogram Estimation . . . . .	28
3.6	Experimental Results . . . . .	29
<b>4</b>	<b>Interferometric Change Detection</b>	<b>37</b>
4.1	Statistical Description of Interferometric Image Pair . . . . .	37
4.2	Incoherent Change Detection . . . . .	39
4.3	Coherent Change Detection . . . . .	45
4.3.1	The Sample Cross Correlation Coefficient Change Statistic . . . . .	46

<b>5</b>	<b>Log Likelihood Change Statistic</b>	<b>52</b>
5.1	PDF of Clairvoyant Log Likelihood Change Statistic . . . . .	54
5.1.1	Special Case of Equal Mean Backscatter Power . . . . .	58
5.2	Detection Performance of the Clairvoyant Detector . . . . .	59
5.3	Generalised Log Likelihood Change Statistic . . . . .	61
<b>6</b>	<b>Application to Experimental Data</b>	<b>63</b>
6.1	Repeat Pass Image Pair 1 . . . . .	67
6.1.1	Joint Statistics of the Repeat Pass Image Pair . . . . .	67
6.1.2	Change Detection Performance . . . . .	76
6.2	Repeat Pass Image Pair 2 . . . . .	80
6.2.1	Joint Statistics of the Repeat Pass Pair . . . . .	86
6.2.2	Change Detection Performance . . . . .	89
<b>7</b>	<b>Summary and Future Work</b>	<b>94</b>
7.1	Future Work . . . . .	94
<b>8</b>	<b>Acknowledgements</b>	<b>95</b>
	<b>References</b>	<b>96</b>

## Appendices

<b>A</b>	<b>Comparison of Theoretical PDFs and Histogram Estimates</b>	<b>100</b>
----------	---	------------

## Figures

1	A typical spotlight SAR imaging geometry. As the radar moves past the scene the antenna is steered so as to continually illuminate the same ground patch. The radar location at a particular transmit/receive point is given by the spherical coordinates $(R_0, \theta_0, \psi_0)$ . . . . .	4
2	Plan view of spotlight mode imaging collection. At each transmit/receive point along the collection aperture the radar transduces the integrated reflectivity function $p_{pol}(r)$ . The value of $p_{pol}(r)$ at a given range is the superposition of all scattering contributions lying along a contour of equirange from the radar transmit/receive point. . . . .	5

3	Range compressed raw echo data collected for three point scatterers where the demodulation reference function is the transmit chirp waveform delayed by the propagation distance to the scene centre. The point at the scene centre undergoes no range migration, while the scatterers offset in azimuth and range undergo a sinusoidal like range migration. . . . .	6
4	The acquired deramp demodulated range echo $P_{pol}(k_r, \theta_0, \psi_0)$ obtained at location $(R_0, \theta_0, \psi_0)$ evaluates the scene's reflectivity in the spatial frequency domain along the radial in the direction $(\theta_0, \psi_0)$ . . . . .	7
5	As the radar moves past the scene the acquired deramp demodulated echo data are samples of the scene's reflectivity evaluated over an acquisition surface in the scene's spatial frequency domain. . . . .	8
6	Polar to rectangular resampling of the acquired deramp demodulated range echo data. . . . .	9
7	Repeat pass spotlight SAR imaging geometry acquired with an across track baseline $B_x$ and an above track baseline of $B_z$ . The acquired range echo data in the primary and repeat pass are samples of the scene's complex reflectivity evaluated over two offset acquisition planes in the scene's spatial frequency domain. . . . .	14
8	Apertures of support in the $(k_x, k_y)$ plane for the acquisition and image formation transfer functions for a repeat pass image pair after baseband translation. Also shown is the common overlapping aperture of support. . . . .	17
9	Apertures of support in the $(k_x, k_y)$ plane for the acquisition and image formation transfer functions for a repeat pass image pair after baseband translation. Also shown is the common overlapping aperture of support. . . . .	22
10	Flow chart of the processing steps required to generate an image pair repeat pass SAR data suitable for applying interferometric change detection algorithms. . . . .	26
11	Primary collection intensity image. The image has been processed to a resolution of 0.58 m (range) by 0.150 m (azimuth) with a Hamming window applied. . . . .	30
12	Repeat pass collection intensity image. The image has been processed to a resolution of 0.58 m (range) by 0.150 m (azimuth) with a Hamming window applied. The temporal baseline for the repeat pass interferometric pair is approximately 12 minutes. . . . .	31
13	Magnitude image of the sample complex cross correlation coefficient obtained by spatially averaging over a sliding estimation window (2 by 6 pixels in range and azimuth respectively). . . . .	32
14	Phase image of the sample complex cross correlation coefficient obtained by spatially averaging over a sliding estimation window (2 by 6 pixels in range and azimuth respectively). . . . .	33
15	Enlarged view of the coherence map over the dirt track that appears along the top of the scene image. . . . .	34



16	Enlarged view of the coherence map over the low coherence random tracks appearing in middle portion of the scene. . . . .	35
17	Enlarged view of the coherence map as well as the primary and repeat pass intensity images over one of the track like disturbances. . . . .	36
18	Simulated and theoretically obtained density functions for the mean backscatter ratio change statistic corresponding to an unchanged scene and a scene with a 3 dB change in the backscatter. The number of independent averages used in the intensity estimates is $N = 9$ . . . . .	42
19	Simulated and theoretical ROC curves for the intensity ratio change statistic obtained using an $N = 9$ and mean backscatter power changes of 1, 3, 5 and 10 dB. . . . .	44
20	Simulated and theoretical ROC curves for the intensity ratio change statistic for a mean backscatter power change of 3 dB and values of $N$ of 9, 16, 25 and 36. . . . .	44
21	Phase component of the cross correlation coefficient of an interferometric image pair where the scatterers in the scene have been subject to a random Gaussian displacement in range and imaged with depression angles of 15 and 45 degrees. The RMS displacement has been normalised to the effective radar wavelength. . . . .	48
22	Expected value of the coherence estimate plotted against the underlying true coherence for a range of sample estimate sizes. . . . .	48
23	Simulated and theoretical probability density functions of the sample coherence corresponding to a true underlying coherence of 0 and 0.6. The sample estimate has been obtained by averaging over $N = 9$ independent pixel pairs. . . . .	49
24	Simulated and theoretical ROC curves for sample coherence change statistic obtained with an unchanged scene partial coherence $\gamma_{unchanged} = 0.45, 0.6, 0.75$ and $0.9$ , a changed scene coherence of $\gamma_{changed} = 0$ and an estimation window size of $N = 9$ independent pixels . . . . .	51
25	Simulated and theoretical ROC curves for sample coherence change statistic obtained with an unchanged scene partial coherence of $\gamma_{unchanged} = 0.6$ , a changed scene coherence of $\gamma_{changed} = 0$ and estimation window sizes of $N = 4, 9, 16$ and $25$ independent pixels . . . . .	51
26	Simulated and theoretical density functions of the likelihood ratio change statistic for the unchanged $H_0$ hypothesis and the changed $H_1$ hypothesis. The mean backscatter ratio of the primary and repeat pass images is 1.04 dB under $H_0$ and 3.77 dB under $H_1$ , $N = 9$ and $\gamma = 0.45$ . . . . .	56
27	Simulated and theoretical density functions of the sample coherence for the unchanged $H_0$ hypothesis and the changed $H_1$ hypothesis. Under $H_0$ the true underlying coherence is $\gamma = 0.45$ while under $H_1$ $\gamma = 0$ and $N = 9$ . . . . .	57

28	Simulated and theoretical density functions of the ratio statistic $r$ for the unchanged $H_0$ hypothesis and the changed $H_1$ hypothesis. The mean backscatter ratio of the primary and repeat pass images is 1.04 dB under $H_0$ and 3.77 dB under $H_1$ and $N = 9$ . . . . .	57
29	Density functions for the decision statistic under $H_0$ and $H_1$ for the case of equal backscatter powers $\sigma_f^2 = \sigma_g^2$ with a partial coherence under $H_0$ of $\gamma = 0.45$ and $N = 9$ . . . . .	58
30	Theoretical and simulated ROC curves for equal channel powers and coherence values of 0.45, 0.6, 0.75 and 0.9 with $N = 9$ . . . . .	61
31	Theoretical and simulated ROC curves for equal channel powers and $N = 4, 9, 16, 25$ with a coherence of 0.6. . . . .	62
32	Theoretical and simulated ROC curves for a scene change scenario where the mean backscatter ratio of the primary and repeat pass images is 1.04 dB under $H_0$ and 3.77 under $H_1$ , $N = 9$ and $\gamma = 0.45$ . . . . .	62
33	Average ROC curves for the log likelihood change statistic obtained using Monte-Carlo simulation techniques. Sample window sizes of $M_0 = M_1 = 25, 64, 121$ and 400 have been used to estimate $Q_0$ and $Q_1$ and a window size of $N = 7$ has been used to compute the log likelihood statistic. The unchanged scene coherence is $\gamma = 0.62$ and it has been assumed that $\sigma_f^2 = \sigma_{g_0}^2 = \sigma_{g_1}^2$ . . .	64
34	Intensity SAR image of the scene used for repeat pass interferometry experiments. Superimposed on the image is a schematic showing the scene changes carried out with the rotary hoe and lawn mower. . . . .	65
35	Intensity SAR image of the scene used for repeat pass interferometry experiments. Superimposed on the image is a schematic showing the scene changes carried out with the rotary hoe and lawn mower. . . . .	66
36	Intensity SAR image generated from the primary pass collection processed to a 3 dB resolution of 0.61 m (range) by 0.15 m (azimuth) with a Hamming window applied. Also shown is the image subchip selected for further processing and change detection analysis. . . . .	68
37	Intensity SAR image generated from the repeat pass collection processed to a 3 dB resolution of 0.61 m (range) by 0.15 m (azimuth) with a Hamming window applied. Also shown is the image subchip selected for further processing and change detection analysis. . . . .	69
38	Mean backscatter power ratio change statistic evaluated over the primary and repeat pass image pair. . . . .	70
39	Sample coherence evaluated over the repeat pass image pair using a 3 by 7 pixel spatial estimation window. . . . .	71
40	Sample interferometric phase evaluated over the repeat pass image pair using a 3 by 7 pixel spatial estimation window. . . . .	72
41	Ground truth observations of the scene disturbances. . . . .	73

42	Amplitude and phase histograms for the primary and repeat pass image subchips. Superimposed on the histograms are the theoretical Rayleigh amplitude and uniform phase density functions that are associated with complex Gaussian scattering behaviour. . . . .	75
43	Histogram and theoretical density function of the sample coherence. The estimated true coherence and ENL used to calculate the theoretical fit are 0.45 and 7 respectively. . . . .	76
44	Histograms and theoretical density functions of the sample interferometric phase obtained by partitioning the image subchips into four equally sized, non-overlapping quadrants. . . . .	77
45	Theoretical and simulated ROC curves of the three change statistics obtained using the covariance matrix estimates given in equation (140) with an ENL=7. . . . .	78
46	The images on the left hand side show, from top to bottom, the mean backscatter power ratio, sample coherence and log likelihood change statistic maps evaluated over the subsampled subchip image pair using a 3 by 3 pixel sliding estimation window. Scene changes are identified as dark pixels. The images on the right hand side show the detections obtained by applying a threshold to the corresponding change maps. The threshold has been experimentally selected to give a false alarm rate of 0.05. . . . .	79
47	Intensity SAR image generated from the primary pass imaging collection processed to a resolution of 0.52 m (range) by 0.150 m (azimuth) with a Hamming window applied. . . . .	81
48	Intensity SAR image generated from the repeat pass imaging collection processed to a resolution of 0.52 m (range) by 0.150 m (azimuth) with a Hamming window applied. . . . .	82
49	Mean backscatter power ratio change statistic evaluated over the primary and repeat pass image pair using a 2 (range) by 6 (azimuth) pixel spatial estimation window. The resolution of the estimate is 0.57 m by 0.22 m with a pixel spacing of 0.343 m by 0.34 m. . . . .	83
50	Sample coherence evaluated over the repeat pass image pair using a 2 by 7 pixel spatial estimation window. The resolution of the estimate is 0.57 m by 0.22 m with a pixel spacing of 0.343 m by 0.34 m. . . . .	84
51	Sample interferometric phase evaluated over the repeat pass image pair using a 2 by 7 pixel spatial estimation window. The resolution of the estimate is 0.57 m by 0.22 m with a pixel spacing of 0.343 m by 0.34 m. . . . .	85
52	Thin plate spline models describing the spatial variation of the mean backscatter power of the primary pass image subchip, indicated on the left and repeat pass image subchip indicated on the right. . . . .	86
53	Amplitude histograms for a 100 by 100 pixel primary and repeat pass image region. Superposed on the histograms are the theoretical Rayleigh amplitude distributions corresponding to Gaussian scattering. . . . .	88

54	Phase histograms for a 100 by 100 pixel primary and repeat pass image region. Superposed on the histograms is the theoretical uniform phase probability density function. . . . .	88
55	Amplitude histograms for a 100 by 100 pixel primary and repeat pass image region. Superposed on the histograms are the theoretical K amplitude distributions. . . . .	89
56	Histogram and theoretical density functions for the sample coherence evaluated from the primary and repeat pass image subchips. A true coherence of 0.62 and an $ENL = 7$ have been used to specify the theoretical sample coherence density function. . . . .	90
57	The image on the left hand side indicates sample estimates of the interferometric phase obtained using a 3 by 3 pixel sliding estimation window. On the right hand side is a thin plate spline fit to the sample estimates of the interferometric phase. . . . .	91
58	Theoretical and simulated ROC curves of the sample coherence and log likelihood change statistics using the change scenario specified by the covariance matrices given in (145) and (146). . . . .	92
59	The images on the left hand side show, from top to bottom, the sample coherence and log likelihood change statistic maps evaluated over the subchip image pair using a 3 by 3 pixel spatial estimation window. The images on the right hand side show the detections obtained by applying a threshold to the corresponding change maps. The thresholds have been experimentally selected to give a false alarm rate of 0.018 . . . . .	93

## Tables

1	System parameters for the Ingara airborne SAR as configured for the repeat pass interferometry experiments. . . . .	64
2	Theoretical and experimental threshold levels and probability of detection values of the three change statistics corresponding to a false alarm probability of 0.05 over the 20 m by 20 m modified area. . . . .	80

# 1 Introduction

Synthetic Aperture Radar (SAR) is a coherent standoff imaging technique capable of generating fine resolution images of the complex radar backscatter (i.e. magnitude and phase) of a scene from large standoff ranges. An important application of SAR is the detection of temporal changes in a scene. Change detection is an application to which SAR is particularly well suited as SARs can consistently produce high quality, well calibrated imagery with good geolocation accuracy.

Two forms of change detection in repeat pass SAR imagery may be considered, namely coherent and incoherent change detection. Incoherent change detection identifies changes in the mean backscatter power of the scene by comparing sample estimates of the mean backscatter power taken from the repeat pass image pair. Typically the sample estimates are obtained by spatially averaging the image pixel intensities (amplitude squared) over local regions in the image pair. The mean backscatter power of a scene is determined by the structural and dielectric properties of the scene and thus may be used to detect changes in soil or vegetation moisture content or surface roughness. Coherent Change Detection (CCD), on the other hand, uses the magnitude of the sample complex cross correlation of an interferometric SAR image pair to quantify changes in the transduced amplitude and phase of the image pixels. Since the transduced pixel amplitude and phase is sensitive to the relative spatial geometry of the scattering contributions within a pixel CCD has the potential to detect very subtle scene changes.

The average mean backscatter power ratio and the magnitude of the sample cross correlation coefficient, commonly referred to as the sample coherence, have been employed in the literature to detect a variety of different types of scene change as well as classify different target types. A number of papers [1], [2], [3] have demonstrated the ability to discriminate between different crops and vegetation types using the sample mean backscatter power and coherence and classifiers have been proposed [4], [5]. The scene coherence has also been used to identify areas inundated by flood [6] and its use in monitoring urban development has been examined [7]. The sensitivity of the scene coherence in detecting subtle man-made scene changes has been demonstrated in [8] in which ERS-1,2 imagery was processed interferometrically and the passage of vehicles over an open field was detected. While in [9] interferometric processing of 1 m resolution airborne X-band SAR imagery was used to identify changes in an earthworks site.

In order to realise the full potential of CCD the primary and repeat pass imagery must be acquired and processed interferometrically. Since CCD identifies scene changes through changes in the transduced amplitude and phase of the image pixels the technique is highly sensitive to mismatch in the acquisition apertures and processing aberrations in the image formation. Coherent change detection thus requires additional interferometric processing steps to mitigate these sources of image decorrelation. In particular differences in the imaging geometry between the primary and repeat pass collections result in a loss of coherence of the image pair, commonly referred to as baseline decorrelation. This can be largely mitigated by extracting a common collection aperture from the two data sets, which may result in degraded image resolution. Decorrelation between the image pair may also arise as a result of residual uncompensated phase errors in the primary and repeat pass images. Such phase errors may occur through errors in the platform navigation information

or due to approximations in the design image formation processor. The impact of these errors can be minimised by constraining the image size and resolution and also by using autofocus techniques. Coherent change detection also requires the primary and repeat pass images to be registered to sub-resolution accuracy, typically a tenth of a resolution cell is required [10].

The requirements on the image acquisition and focusing for incoherent change detection on the other hand are less severe. The imagery should be acquired with approximately the same imaging geometry to ensure false detections due to variations in radar shadowing, occlusion and differences in transduced backscatter power due to variations in incidence angle are minimised. The constraint on the baseline offset between the image collections however, is less severe than that associated with CCD. The impact of residual phase errors is also less severe as change detection is based on a comparison the image intensity data only. Furthermore registration accuracy needs to be only of the order of a resolution cell for reliable change detection performance.

The detection performance of a change statistic is dependent on its ability to discriminate between those areas of the scene affected by the change of interest and those areas which are affected by other noise sources. These noise sources may include other sources of scene change for example weathering due to wind and rain as well as the multiplicative and additive system noise sources discussed above. The mean backscatter power and complex correlation coefficient are sensitive to different properties of a scene thus the detection performance of these change statistics will vary depending on the nature of the scene changes and noise sources. Indeed Rignot [11] cites examples of repeat pass imagery in which changes are detected in a scene via changes in the mean backscatter power without a corresponding change in the sample coherence and vice versa. Thus as scene changes may affect a broad range of scene properties both coherence and incoherent change detection statistics should be considered to properly characterise scene changes. Discrimination between scene changes of interest and other sources of change in the transduced imagery may also be assisted by spatial averaging, i.e., evaluating the change statistics over a local spatial neighbourhood. In detecting fine-scale scene changes such as, for example vehicle tracks however, the spatial estimation window must be commensurate with the size of the scene changes. Otherwise the change statistic incorporates contributions from a mixture of scene change processes thereby limiting the change statistic's ability to distinguish between them.

In this report the detection of fine-scale scene changes using both coherent and incoherent change detection techniques is examined. In Section 2 the formation of fine resolution spotlight SAR imagery using the Polar Format Algorithm (PFA) is examined. This allows the imaging equations describing a repeat pass interferometric pair to be specified in Section 3. From the imaging equations the decorrelation resulting from mismatch between the acquisition and image formation functions is quantified and techniques to minimise these effects are discussed. A practical interferometric SAR processor developed to process repeat pass SAR data acquired with the DSTO Ingara X-band airborne SAR is described in Section 3. Results from a change detection experiment conducted with Ingara are given in which changes, possibly due to the movement of sheep, are presented. Section 4 describes the commonly used mean backscatter power ratio and sample coherence change statistics for detecting scene changes. Assuming the primary and repeat pass images in an interferometric pair are described by a jointly Gaussian random process, the theoretical

detection performance for these change statistics is derived. Section 5 describes a recently proposed log likelihood change statistic for detecting scene changes in an interferometric SAR image pair. The theoretical detection performance is given and shown to be superior to the commonly used mean backscatter power ratio and sample coherence change statistics. The three change statistics namely the mean backscatter power ratio, the sample coherence and log likelihood ratio change statistics are applied to experimental repeat pass data acquired with the Ingara X-band SAR in Section 6.

## 2 Spotlight SAR Image Formation

Synthetic Aperture Radar (SAR) imaging is a two step process of coherent data acquisition and subsequent coherent processing of a series of radar range echoes to recover a fine resolution image of a scene. The resolution of the focused SAR imagery is an important parameter in determining the interpretability of the imagery and the quality of the information that may be extracted [12]. In particular the performance of post processing applications such as target detection, classification [13] as well as interferometry applications such as change detection [1], [9] are all sensitive to the image resolution.

Synthetic aperture radar transduces a fine resolution image of the complex radar backscatter of a scene. Fine range resolution is readily achieved using large bandwidth transmit pulses and pulse compression techniques. Indeed airborne radars with 1.8 GHz transmit bandwidths have been demonstrated with corresponding range resolutions of 0.1 m [14], [15]. The transduced range echoes however contain contributions from all scatterers illuminated by the antenna footprint. The range echo data thus represents an integrated scene response and the ability to resolve scatterers displaced in azimuth, without further processing, is limited by the size of the antenna footprint as determined by the antenna beamwidth and the slant range to the scene. Finer azimuth resolution may be achieved by using a spatially longer antenna to obtain a narrower azimuth beamwidth. For typical SAR standoff ranges however, the antenna size required to achieve azimuth resolutions commensurate with commonly achieved range resolutions is generally impractical.

In synthetic aperture radar fine azimuth resolution is achieved using an antenna of modest size by coherently processing a series of range echoes obtained as the radar moves past the scene. The coherent processing combines the information from the series of range echoes to, in effect, synthesize a large spatial array. This permits the inversion of the integrated scene response into a fine resolution two dimensional estimate of the complex reflectivity of the scene. In spotlight SAR, in which the antenna is continually steered onto the scene as the radar moves past, very large spatial arrays may be synthesized to achieve very fine azimuth resolution imagery over a limited spatial area.

### 2.1 SAR Data Acquisition and Range Processing

In the typical airborne spotlight SAR data acquisition geometry the SAR antenna is steered, nominally perpendicular to the flight path, so as to continually illuminate a ground patch using the side looking geometry shown in Figure 1. While moving past the scene the SAR periodically transmits a wide bandwidth electromagnetic pulse, typically a chirp

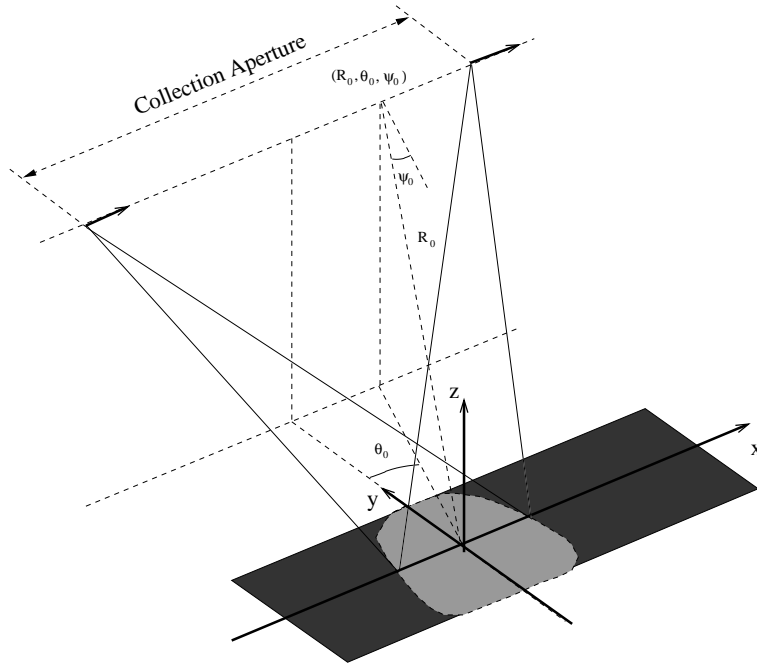


**Figure 1:** A typical spotlight SAR imaging geometry. As the radar moves past the scene the antenna is steered so as to continually illuminate the same ground patch. The radar location at a particular transmit/receive point is given by the spherical coordinates  $(R_0, \theta_0, \psi_0)$ .

signal, of duration  $T$  at the radar centre frequency  $f_0$ . The transmit chirp signal may be represented by,

$$s(t) = \text{rect}\left(\frac{t}{T}\right) \cos\left(2\pi\left(f_0 t + \alpha t^2\right)\right). \quad (1)$$

where  $s(t)$  is zero outside the interval  $-T/2 \leq t \leq T/2$  and  $\alpha$  is the chirp rate. The instantaneous bandwidth of the signal is given by  $f_{bw} = 2\alpha T$ . A small portion of the transmitted energy, incident on the scene, is re-radiated back towards the radar by the scattering elements in the scene. The received signal at location  $(R_0, \theta_0, \psi_0)$  (where  $R_0$  is the line of sight distance to the scene centre and  $\theta_0$  and  $\psi_0$  are the azimuth and elevation angles respectively as shown in Figure 1) along the radar flight track may thus be considered to be the superposition of delayed copies of the transmit chirp waveform each modulated by a complex value describing the complex reflectivity of the scattering elements in the scene.

The task of the SAR processor is to recover a two dimensional image of the scene's complex reflectivity from the transduced echoes. The first step to achieving this is to demodulate the received echoes and apply range compression. In spotlight SAR, as the image patch size is typically small, a demodulation technique commonly referred to as deramp demodulation [9], [16] is used. In this approach the received signal is demodulated by mixing it with a delayed copy of the transmit waveform where the delay is the two way propagation delay to the scene centre. A range compressed range echo is subsequently obtained by applying an inverse Fourier transform to the demodulated echo.



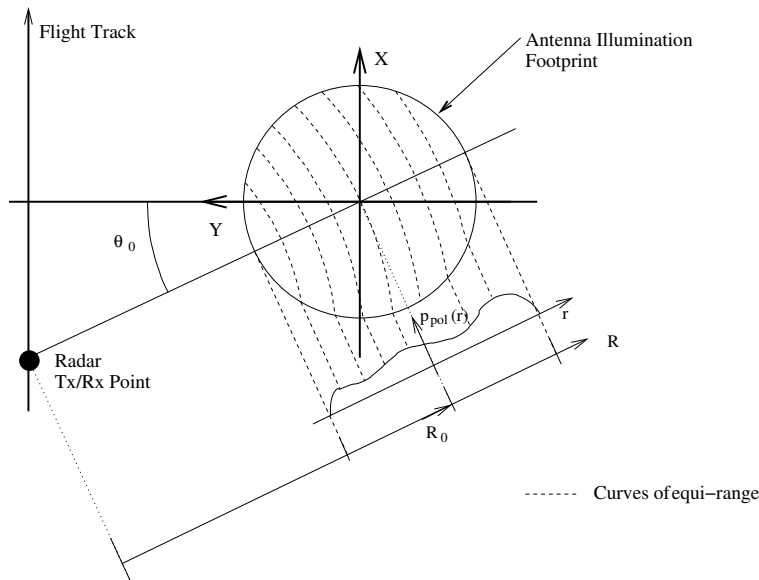


**Figure 2:** Plan view of spotlight mode imaging collection. At each transmit/receive point along the collection aperture the radar transduces the integrated reflectivity function  $p_{pol}(r)$ . The value of  $p_{pol}(r)$  at a given range is the superposition of all scattering contributions lying along a contour of equirange from the radar transmit/receive point.

With reference to Figure 2 the deramp demodulated and inverse Fourier transformed signal obtained at the transmit/receive location  $(R_0, \theta_0, \psi_0)$  is given by  $p_{pol}(r)$ . The variable  $r$  is the propagation range measured along the radar's line of sight to the scene centre. At a given value of  $r$ ,  $p_{pol}(r)$  is the superposition of all scatterer contributions lying along the equi-range contour  $R = R_0 - r$  centred about the radar location  $(R_0, \theta_0, \psi_0)$ . Figure 3 shows the unfocused image (plot of range compressed echoes as a function of propagation range  $r$  and position along the synthetic aperture) obtained from a series of deramp demodulated inverse Fourier transformed range echo pulses collected as the radar moves past the scene. In this case the variation in the propagation range  $r = R - R_0$  determines the range migration of the individual scatterer responses in the range compressed signal history. It can be seen from Figure 3 that scatterers displaced in azimuth with respect to the focus point are subject to a sinusoidal range variation while scatterers displaced in range are subject to a co-sinusoidal response. A scatterer at the scene centre however is compensated for exactly and is subject to no pulse-to-pulse range variation over the collection aperture.

The task of the spotlight image formation processor is to “compress” each of the “smeared” scatterer responses to a point and so recover a focused image. The complexity of SAR processing algorithms arises due to the significant migration of the scatterer responses through range resolution cells over the synthetic aperture. Also the nature of the range echo response varies as a function of the scatterer's spatial location relative to the scene centre. Most imaging algorithms employ some degree of approximation to the scattering response to allow a computationally efficient processor to be implemented.

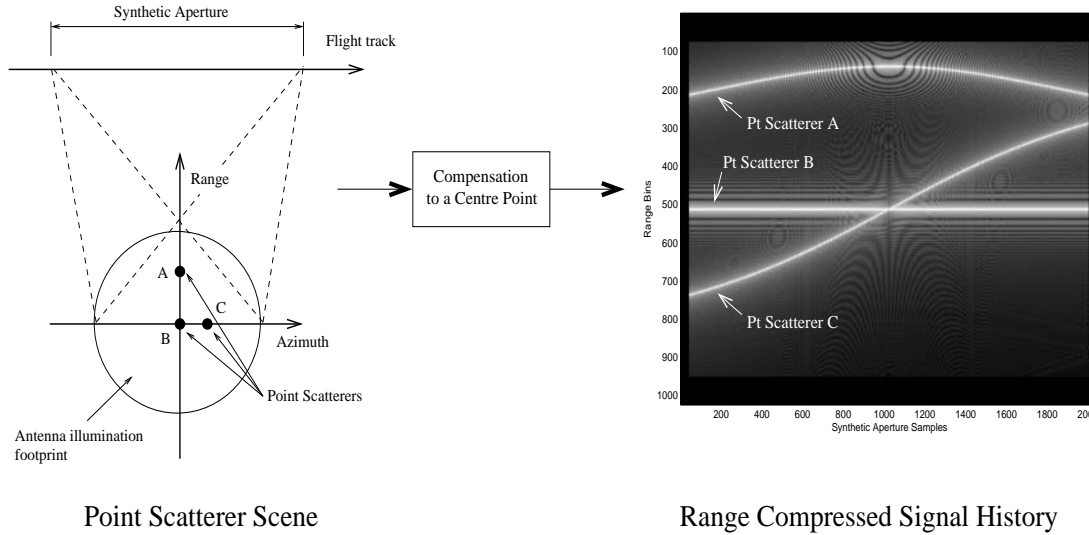


**Figure 3:** Range compressed raw echo data collected for three point scatterers where the demodulation reference function is the transmit chirp waveform delayed by the propagation distance to the scene centre. The point at the scene centre undergoes no range migration, while the scatterers offset in azimuth and range undergo a sinusoidal like range migration.

## 2.2 The Polar Format Algorithm

The Polar Format Algorithm (PFA) for spotlight SAR image formation is an efficient, readily implemented algorithm for the focusing of deramp demodulated echo data. The PFA compensates for the migration of the scatterer's response through range resolution cells for all scatterers in the scene via resampling operations carried out in the frequency domain i.e., on the deramp demodulated range echoes obtained prior to the inverse Fourier transform.

The origins of the polar format technique may be traced back to research conducted by the University of Michigan in the early 1960s into fine resolution imaging of rotating objects using radar. In this research the coherent doppler filtering of fine resolution range echo data collected from targets placed on a rotating platform was found to produce poorly focused imagery. This was attributed to the pronounced scatterer migration through range resolution cells as the scene rotated past the radar. In [17], Walker proposed placing the range echo data in a polar grid to compensate for the observed sinusoidal variation of the range migration. This effectively compensates for the range cell migration in a simple and efficient step for all scatterers in the illuminated scene, obviating the need for a two dimensional focusing correlation kernel. Subsequent range doppler processing generates the desired fine resolution spotlight SAR imagery using simple Fourier transform techniques.

Considerable insight into the spotlight mode SAR image formation problem and the inherent polar alignment of the data was gained by the discovery that the image formation problem could be formulated as a tomographic reconstruction problem. In [16] Munson was able to demonstrate that the deramp demodulated range echo samples could be related directly to the spatial frequency domain description of the scene reflectivity via the

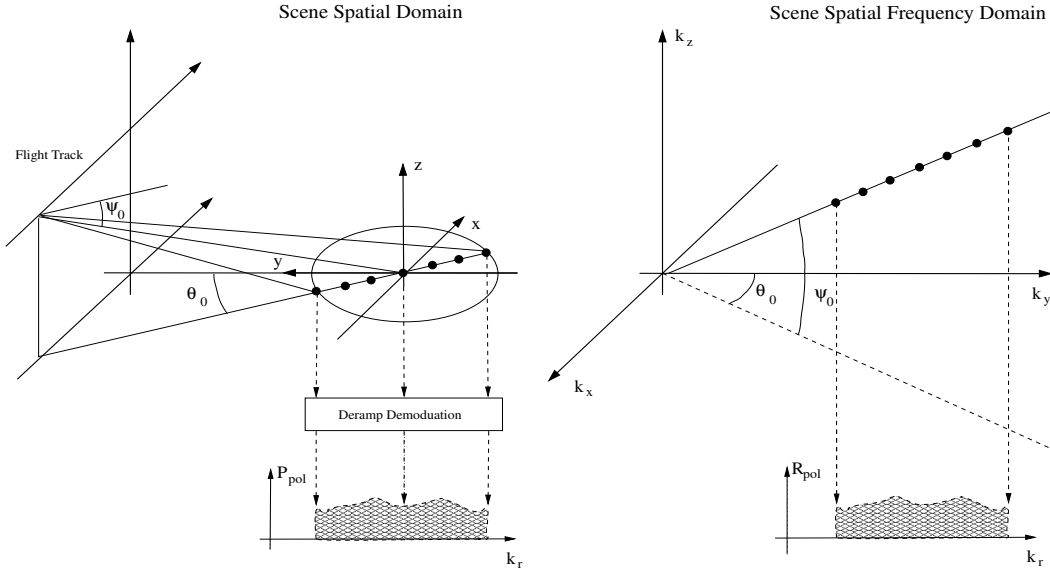


**Figure 4:** The acquired deramp demodulated range echo  $P_{pol}(k_r, \theta_0, \psi_0)$  obtained at location  $(R_0, \theta_0, \psi_0)$  evaluates the scene's reflectivity in the spatial frequency domain along the radial in the direction  $(\theta_0, \psi_0)$ .

projection-slice theorem. In the context of spotlight SAR imaging the projection-slice theorem states that the deramp demodulated range echo data collected in a given look direction  $(\theta, \psi)$ , measured from the scene focus point to the radar, is equal to the scene's reflectivity in the spatial frequency domain measured along a radial with the same look direction  $(\theta, \psi)$ . The offset of the data samples along the frequency domain radial from the origin is proportional to the radar centre frequency  $f_0$  while the length of support along the radial is determined by the chirp signal bandwidth  $f_{bw}$ . This is illustrated in the Figure 4.

In Figure 4 the scene is described by a reflectivity function  $r(x, y, z)$  while  $p_{pol}(r, \theta_0, \psi_0)$  denotes the deramped inverse Fourier transformed scene response as the radar location  $(R_0, \theta_0, \psi_0)$ . The scene response after deramp demodulation, prior to the inverse Fourier transform may be denoted by  $P_{pol}(k_r, \theta_0, \psi_0)$  where  $k_r$  is the Fourier transform variable associated with  $r$  in  $p_{pol}$ . The function  $P_{pol}(k_r, \theta_0, \psi_0)$  is related to the scene reflectivity  $r(x, y, z)$  via the slice projection theorem. That is, applying a Fourier transform to  $r(x, y, z)$  to give  $R(k_x, k_y, k_z)$  and defining a change of variables from cartesian  $(k_x, k_y, k_z)$  to spherical coordinates  $(k_r, \theta, \psi)$  where,

$$\begin{bmatrix} k_x \\ k_y \\ k_z \end{bmatrix} = \begin{bmatrix} k \cos \psi \sin \theta \\ k \cos \psi \cos \theta \\ k \sin \psi \end{bmatrix}, \quad (2)$$

gives  $R_{pol}(k_r, \theta, \psi)$ . The projection-slice theorem states that  $P_{pol}(k_r, \theta_0, \psi_0)$  equals  $R_{pol}$  evaluated at along the radial in the three dimensional Fourier space defined by the look angles  $(\theta, \psi) = (\theta_0, \psi_0)$  i.e.,

$$P_{pol}(k_r, \theta_0, \psi_0) = \text{rect}\left(\frac{k_r - k_0}{k_{bw}}\right) R_{pol}(k_r, \theta_0, \psi_0), \quad (3)$$

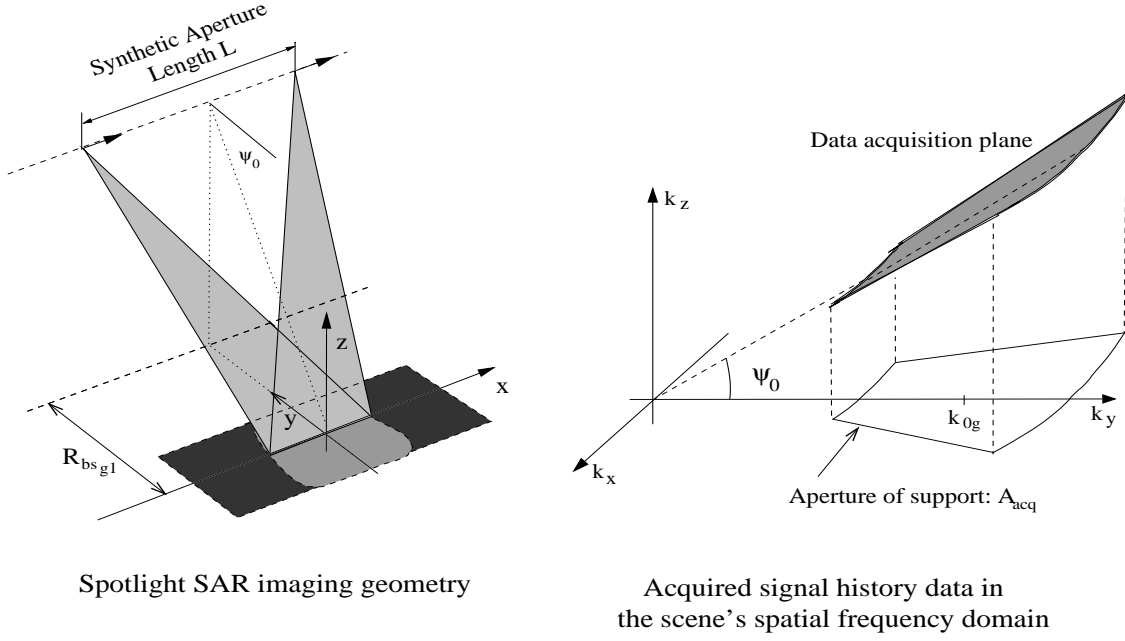


**Figure 5:** As the radar moves past the scene the acquired deramp demodulated echo data are samples of the scene's reflectivity evaluated over an acquisition surface in the scene's spatial frequency domain.

where  $k_0 = 2\pi f_0/c$  and  $k_{bw} = 2\pi f_{bw}/c$ .

As the radar moves past the scene the range echo data samples will sweep out a polar raster grid in the spatial frequency domain defined by variation in the azimuth and elevation angles  $\theta$  and  $\psi$  respectively, i.e., the imaging geometry. This is illustrated in Figure 5.

Fast, efficient image reconstruction subsequently proceeds by direct Fourier domain reconstruction: The collected deramp data  $P_{pol}(k_r, \theta, \psi)$  residing on the polar grid are firstly resampled onto a uniformly spaced rectangular grid  $(k_x, k_y)$  in the  $k_z = 0$  plane, see Figure 6.

$$P_{pol}(k_r, \theta, \psi) \longrightarrow P(k_x, k_y, k_z = 0). \quad (4)$$

An image of the scene may subsequently be recovered by applying a two dimensional inverse Fourier transform to a subset or windowed portion of the available interpolated data set  $P(k_x, k_y, k_z = 0)$ .

The nature of the image recovered by the PFA may be ascertained by considering a scene consisting of an elementary point scatter with reflectivity  $q_s \exp(j\phi_s)$  at location  $(x_s, y_s, z_s)$ ,

$$r(x, y, z) = q_s \exp(j\phi_s) \delta(x - x_s, y - y_s, z - z_s), \quad (5)$$

where  $\delta(x, y, z)$  is the Dirac delta function. In the Fourier domain the reflectivity function is given by,

$$R(k_x, k_y, k_z) = \iiint r(x, y, z) \exp(-j(xk_x + yk_y + zk_z)) dx dy dz,$$

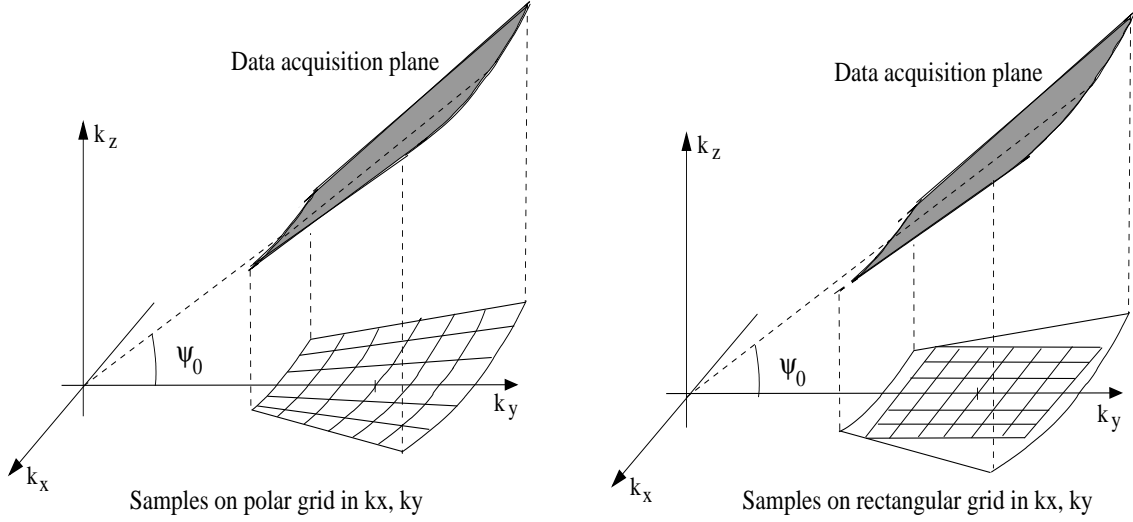


**Figure 6:** Polar to rectangular resampling of the acquired deramp demodulated range echo data.

$$= q_s \exp(j\phi_s) \exp(-j(x_s k_x + y_s k_y + z_s k_z)). \quad (6)$$

The deramp demodulated data set acquired over a collection aperture can be expressed in terms of the scene reflectivity as,

$$P(k_x, k_y, k_z) = A_{acq}(k_x, k_y, k_z) R(k_x, k_y, k_z), \quad (7)$$

where  $A_{acq}$  describes the acquisition aperture in the three dimensional Fourier space. For the case of straight and level flight without squint the elevation angle varies in such a way that the polar grid lies in a plane in the three dimensional spatial Fourier domain given by,

$$k_z = \beta_0 k_y, \quad (8)$$

where  $\beta_0 = \tan \psi_0$  with  $\psi_0$  being the elevation angle at aperture centre. The aperture of support  $A_{acq}$  may subsequently be expressed as,

$$A_{acq}(k_x, k_y, k_z) = A_{ac}(k_x, k_y) \delta(k_z - \beta_0 k_y). \quad (9)$$

Given that the aperture of support for the collected data in the spatial frequency domain is offset from the origin, as illustrated in Figure 5, it is convenient to define the following baseband form of equation (7),

$$\begin{aligned} P_b(k_x, k_y, k_z) &= P(k_x, k_y + k_{0_g}, k_z), \\ &= A_{acq}(k_x, k_y + k_{0_g}, k_z) R(k_x, k_y + k_{0_g}, k_z). \end{aligned} \quad (10)$$

The variable  $k_{0_g}$  is the location of the aperture centre along the  $k_y$  axis as shown in Figure 5. An image is recovered from the collected data  $P_b(k_x, k_y, k_z)$  by applying a window

function  $A_{ifp}(k_x, k_y)$  typically chosen to be a rectangular region lying wholly within the acquisition aperture of support in the  $(k_x, k_y)$  plane (see Figure 6) such that,

$$A_{ifp}(k_x, k_y)A_{acq}(k_x, k_y + k_{0_g}, k_z) = A_{ifp}(k_x, k_y)\delta(k_z - \beta_0(k_y + k_{0_g})). \quad (11)$$

For an unweighted window function  $A_{ifp}(k_x, k_y)$  is defined as,

$$A_{ifp}(k_x, k_y) = \text{rect}\left(\frac{k_x}{k_{bw_x}}\right) \text{rect}\left(\frac{k_y}{k_{bw_y}}\right). \quad (12)$$

The recovered image of the point scatterer is subsequently obtained by applying an inverse Fourier transform to  $A_{ifp}(k_x, k_y, k_z)P_b(k_x, k_y, k_z)$ , i.e.,

$$f(x, y, z) = \iiint A_{ifp}(k_x, k_y, k_z)P_b(k_x, k_y, k_z)\exp(j(xk_x + yk_y + zk_z))dk_x dk_y dk_z. \quad (13)$$

Substituting (10) for  $P_b$  in (13) gives

$$\begin{aligned} f(x, y, z) &= \iiint A_{ifp}(k_x, k_y)A_{acq}(k_x, k_y + k_{0_g}, k_z)R(k_x, k_y + k_{0_g}, k_z) \\ &\quad \exp(j(xk_x + yk_y + zk_z))dk_x dk_y dk_z. \end{aligned} \quad (14)$$

Substituting (6) and (11) into (14) gives,

$$\begin{aligned} f(x, y, z) &= q_s \exp(j\phi_s) \iiint A_{ifp}(k_x, k_y)\delta(k_z - \beta_0(k_y + k_{0_g}))\exp(-jy_s k_{0_g}) \\ &\quad \exp(j((x - x_s)k_x + (y - y_s)k_y + (z - z_s)k_z))dk_x dk_y dk_z, \\ &= q_s \exp(j\phi_s)\exp(-j(y_s + z_s\beta_0)k_{0_g}) \iint A_{ifp}(k_x, k_y) \\ &\quad \exp(j((x - x_s)k_x + (y - y_s + z_s\beta_0 + z_s\beta_0)k_y))dk_x dk_y. \end{aligned} \quad (15)$$

The inverse Fourier transform expression in (15) may expressed as a convolution of a SAR point spread function with a modified form of the point scatterer reflectivity,

$$f(x, y, z) = a(x, y) \otimes f_p(x, y, z). \quad (16)$$

The function  $a(x, y)$  is the inverse Fourier transform of the aperture window  $A_{ifp}(k_x, k_y)$  and may be interpreted as the point spread function of the SAR image processor,

$$a(x, y) = \frac{1}{4\pi^2} \iint A_{ifp}(k_x, k_y)\exp(j(xk_x + yk_y))dk_x dk_y. \quad (17)$$

For the rectangular windowing function in (12) the point spread function  $a(x, y)$  takes the form of a two dimensional sinc function,

$$\begin{aligned} a(x, y) &= \frac{1}{4\pi^2} \iint A_{ifp}(k_x, k_y)\exp(j(xk_x + yk_y))dk_x dk_y, \\ &= \frac{k_{bw_x}k_{bw_y}}{4\pi^2} \text{sinc}\left(\frac{xk_{bw_x}}{2\pi}\right) \text{sinc}\left(\frac{yk_{bw_y}}{2\pi}\right). \end{aligned} \quad (18)$$

The resolution of the recovered PFA image is defined by the distance from the mainlobe peak to the first null of the point spread function  $a$  i.e.,

$$\text{Azimuth Resolution: } \rho_x = \frac{2\pi}{k_{bw_x}}, \quad (19)$$

$$\text{Range Resolution: } \rho_y = \frac{2\pi}{k_{bw_y}}. \quad (20)$$

The point scatterer reflectivity, as transduced by the radar, is given by the function  $f_p(x, y)$  in (16) where,

$$f_p(x, y, z) = q_s \exp(j\phi_s) \exp(j(y_s + z_s\beta_0)k_{0_g}) \delta(x - x_s, y - y_s + z\beta_0 - z_s\beta_0). \quad (21)$$

The point scatterer appears in the recovered image at location,

$$x = x_s \quad (22)$$

$$y = y_s + (z_s - z)\beta_0 \quad (23)$$

Observe that the location of the point scatterer in the  $z$  dimension is not uniquely determined, i.e., it is not possible to resolve the scatterer's location above the ground plane  $z = 0$  based on the single collection  $P_b(k_x, k_y, k_z)$ . To determine the scatterer's height  $z_s$ , two or more collections over a range of elevation angles  $\psi$  is required [18]. This allows an aperture in the  $k_z$  dimension of Figure 5 to be formed. The acquired data from the multiple collections can be placed in a three dimensional data “cube” in the Fourier space and a three dimensional image formed via a three dimensional inverse Fourier transform. For the case of a single collection however, since the height location of the scatterer is not uniquely determined it is common to consider forming a ground plane image for which  $z$  in (21) is set to zero. It can be seen from (23) that in a ground plane image the scatterer appears, not at its true location of  $(x_s, y_s)$ , but at location  $(x_s, y_s + z_s\beta_0)$ . This is the layover phenomenon in which elevated targets appear laid over towards the radar thus appearing in range bins closer to the radar.

From (21) the point scatterer as transduced by the radar is also subject to a phase modulation  $\phi = (y_s + z_s\beta_0)k_{0_g}$ . While this phase is of no significance in the case of a single image collection if two images are acquired of the scene with slightly different depression angles  $\psi_0$  and  $\psi_1$  and the images “interfered” then the phase difference between the image pair is related to the depression angle difference and the point scatterer height. This forms the basis for the terrain height mapping application of SAR interferometry which shall be discussed in Section 3.

While equation (16) describes the spotlight SAR image of a point scatterer the analysis may be extended to encompass an scene of arbitrary reflectivity. Of particular interest are scenes described by a surface reflectivity  $r_s(x, y)$  as well as a terrain height function  $h(x, y)$ ,

$$r(x, y, z) = r_s(x, y) \delta(z - h(x, y)). \quad (24)$$

The same approach as described in equations (6) to (16) may be applied to (24) to determine the transduced SAR image. It may be shown [9] that the ground plane SAR image takes the form,

$$\hat{r}(x, y + \Delta_y) = a(x, y) \otimes r'_s(x, y). \quad (25)$$

The function  $a(x, y)$  is the SAR point spread function as defined in (18) while  $r'_s(x, y)$  is related to the surface reflectivity,

$$r'_s(x, y) = r_s(x, y) \exp(-j(y + \beta_0 h(x, y))k_{0_g}). \quad (26)$$

$\Delta_y$  is the layover term and is given by  $\beta_0 h(x, y)$ .

## 2.3 Comments on the PFA

The PFA is an efficient readily implemented algorithm for forming imagery using de-ramp demodulated data. In particular the range cell migration correction required (see Figure 3) is efficiently carried out in the frequency domain via the resampling operation which transforms the data  $G_{pol}(k_r, \theta, \psi)$  acquired on a polar grid into data sampled on a rectangular, cartesian grid  $G(k_x, k_y, k_z)$ . In practice this operation is typically carried out in a two step process using one dimensional interpolators [9]. Indeed this represents a considerable portion of the overall computational burden of the PFA. The design of the interpolators, in particular the use of more appropriate three dimensional interpolators, as well as the use of fast Fourier transforms for use on irregular sample grids remains an active area of research.

Critical to the PFA is the projection-slice theorem which relates the evaluation of a line integral of a two dimensional function to the Fourier transform of the function. In the context of spotlight SAR the projection-slice is applied in an approximate sense. Provided the imaged scene is sufficiently small and the radar sensor is sufficiently far away from the scene then the propagating electromagnetic waves incident on the scene and received by the radar may be modelled as plane waves. Under this approximation the transduced reflectivity at propagation range delay will be given by the integral of the scene reflectivity over a line perpendicular to the direction of wave propagation. and the projection-slice theorem may be applied. A more accurate description of the incident electromagnetic wave however, is to use a spherically propagating wave model. In this model the integrated scene response at a given demodulation delay is formed by taking an integral along a circular arc rather than along a straight line. In this case the PFA doesn't completely compensate for the range migration and the associated phase modulation of the scatterer response in the acquired signal history data. As a consequence the recovered PFA image is subject to a defocus and geometric distortion that varies spatially over image [9]. Two conditions must be satisfied if the line integral approximation is to be applied. Firstly, the range migration error due to wavefront curvature over the imaged scene must be less than the resolution cell size. Secondly, over the coherent processing interval the range error due to wavefront curvature for a particular scatterer must vary by no more than a small fraction of a wavelength. With these constraints [19] limits on the resolution and image patch size that may be recovered using the PFA can be derived,

$$x < \rho_x \sqrt{\frac{R_{bs_g} k_{0_g}}{2\pi \cos^2 \psi_0}}, \quad (27)$$

$$y < \frac{\rho_x}{\cos \psi_0} \sqrt{\frac{R_{bs_g} k_{0_g}}{2\pi \cos^2 \psi_0}}, \quad (28)$$



where  $R_{bsg}$  is the standoff range of the radar from the scene centre measured in the ground plane at the aperture centre. For imaging scenarios beyond these limits image formation algorithms must address the effects of wavefront curvature on the scatterer point response in the acquired signal history data.

### 3 Spotlight SAR Interferometry

Synthetic Aperture Radar Interferometry (InSAR) employs two complex valued SAR images to derive additional information about a scene by exploiting differences in the amplitude and phase of the image pair. The information made available by the joint processing of an interferometric image pair is determined by the difference between the imaging geometries used for each collection and any scene changes arising in the temporal delay between the collections.

In single pass interferometry the two complex SAR images are acquired simultaneously via two independent receive antennas located on the same moving platform. In the terrain mapping application of SAR interferometry the antennas are configured to give an across and/or above track baseline offset. Due to these baseline offsets the scene is viewed with a slightly different imaging geometry. In particular the two imaging collections have slightly different mid-aperture elevation angles  $\psi_1$  and  $\psi_2$  as well as slightly different standoff ranges. Given accurate measurements of  $\psi_1$  and  $\psi_2$  an estimate of terrain height as a function of ground plane location  $h(x, y)$  may be retrieved from the pixel-wise phase difference between the image pair. The accuracy of this approach is of the order of the radar wavelength and thus can potentially provide highly accurate estimates of the scatterer elevation.

An alternative application of the joint processing of a SAR image pair arises when the image pair are acquired at different times but using the same imaging geometry. In this imaging modality differences in the amplitude and phase between the image pair may be attributed to changes in the scene that arise in the time interval between collections. For example, by placing two antennas, displaced in the along track direction, on the same sensor platform image pairs may be acquired with a temporal delay of the order of a few milliseconds. Such Along Track Interferometers (ATI) allow the suppression of static, stable clutter scattering contributions to identify the presence of slow moving targets in a scene [20], [21] and may also be used for mapping ocean currents [22]. Alternatively, using repeat pass collections, changes in the scene that occur over hours, days and even years may be transduced by using coherent change detection techniques. In coherent change detection scene changes are detected by comparing the amplitude and phase of a repeat pass image pair using the complex cross correlation coefficient change detection metric. As the transduced pixel phase is sensitive to displacements of scattering elements in the scene of the order of a fraction of the radar wavelength, coherent change detection may be used to detect very subtle disturbances such as the vehicle tracks and other subtle surface deformations [23], [24] and [25].

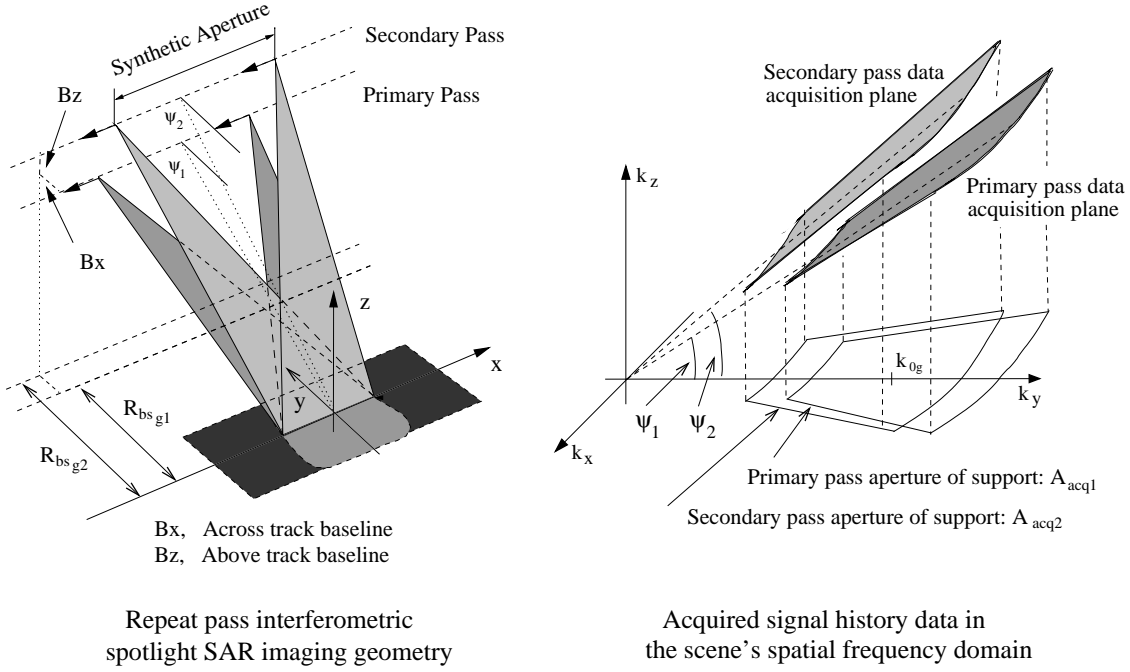


**Figure 7:** Repeat pass spotlight SAR imaging geometry acquired with an across track baseline  $B_x$  and an above track baseline of  $B_z$ . The acquired range echo data in the primary and repeat pass are samples of the scene's complex reflectivity evaluated over two offset acquisition planes in the scene's spatial frequency domain.

### 3.1 Forming an Interferometric Image Pair

Figure 7 illustrates an interferometric spotlight SAR collection in which the primary and secondary collection apertures have an across and above track baseline offset of  $B_x$  and  $B_z$  respectively. In the case of single pass interferometry these offsets are defined by the relative locations of the two receive antennas on the radar platform. In a repeat pass interferometric acquisition on the other hand, the offsets would represent the differences between the primary and repeat pass flight tracks of the radar platform. Due to these baseline offsets the scene is viewed with a slightly different imaging geometry in each acquisition. In particular the primary and secondary acquisitions have slightly different mid-aperture elevation angles of  $\psi_1$  and  $\psi_2$  respectively as well as slightly different standoff ranges:  $R_{bsg1}$  in the primary collection and  $R_{bsg2}$  in the secondary collection. As a consequence, using the projection-slice theorem, the acquired deramped signal history data in the primary and secondary acquisitions are samples of the scene's spatial frequency domain representation on two slightly different planes defined by  $k_z = \tan \psi_1 k_y$  and  $k_z = \tan \psi_2 k_y$  respectively as illustrated in Figure 7 (assuming straight and level flight without squint).

Defining the scene complex reflectivity in the primary acquisition as,

$$r_1(x, y, z) = r_{1s}(x, y)\delta(z - h(x, y)), \quad (29)$$

and in the secondary acquisition as,

$$r_2(x, y, z) = r_{2s}(x, y)\delta(z - h(x, y)), \quad (30)$$

(Note that in the case of single pass interferometry the scene reflectivity is the same in each channel in which case  $r_1(x, y, z) = r_2(x, y, z)$ .) the acquired deramp signal history data for the two acquisitions may be written as,

$$P_1(k_x, k_y, k_z) = A_{acq1}(k_x, k_y, k_z)R_1(k_x, k_y, k_z), \quad (31)$$

and,

$$P_2(k_x, k_y, k_z) = A_{acq2}(k_x, k_y, k_z)R_2(k_x, k_y, k_z), \quad (32)$$

where  $R_1(k_x, k_y, k_z)$  and  $R_2(k_x, k_y, k_z)$  are the Fourier transforms of  $r_1(x, y, z)$  and  $r_2(x, y, z)$  respectively. Note it has been assumed that there has been no surface deformation in the interval between collections so that the terrain height  $h(x, y)$  is the same in both acquisitions.

Due to the different acquisition geometries, the offsets as well as the dimensions of the apertures of support in the  $(k_x, k_y)$  plane for the acquired deramp demodulated signal history differ, as illustrated in Figure 7. In defining the baseband signal history  $P_{1b}$  and  $P_{2b}$  for the primary and secondary acquisitions however, a common baseband spatial frequency  $k_{0g}$  is employed and is chosen to be the centre of the overlapping portion of the acquisition apertures such that,

$$\begin{aligned} P_{1b}(k_x, k_y, k_z) &= P_1(k_x, k_y + k_{0g}, k_z), \\ &= A_{acq1}(k_x, k_y + k_{0g}, k_z)R_1(k_x, k_y + k_{0g}, k_z), \end{aligned} \quad (33)$$

and,

$$\begin{aligned} P_{1b}(k_x, k_y, k_z) &= P_2(k_x, k_y + k_{0g}, k_z), \\ &= A_{acq2}(k_x, k_y + k_{0g}, k_z)R_2(k_x, k_y + k_{0g}, k_z). \end{aligned} \quad (34)$$

As a consequence the acquisition apertures of support for  $P_{1b}$  and  $P_{2b}$  are misaligned in the baseband spatial frequency domain as illustrated in Figure 8. The primary and secondary ground plane image formation window functions  $A_{ifp1}$  and  $A_{ifp2}$  may be defined as,

$$A_{ifp1}(k_x, k_y)A_{acq1}(k_x, k_y + k_{0g}, k_z) = A_{ifp1}(k_x, k_y)\delta(k_z - \beta_1(k_y + k_{0g})), \quad (35)$$

$$A_{ifp2}(k_x, k_y)A_{acq2}(k_x, k_y + k_{0g}, k_z) = A_{ifp2}(k_x, k_y)\delta(k_z - \beta_2(k_y + k_{0g})), \quad (36)$$

where, using an unweighted rectangular window function,  $A_{ifp1}(k_x, k_y)$  and  $A_{ifp2}(k_x, k_y)$  have the form,

$$A_{ifp1}(k_x, k_y) = \text{rect}\left(\frac{k_x}{k_{bw_{x1}}}\right)\text{rect}\left(\frac{k_y - \Delta_1}{k_{bw_{y1}}}\right), \quad (37)$$

$$A_{ifp2}(k_x, k_y) = \text{rect}\left(\frac{k_x}{k_{bw_{x2}}}\right)\text{rect}\left(\frac{k_y + \Delta_2}{k_{bw_{y2}}}\right). \quad (38)$$

The image formation window dimensions  $(k_{bw_{x1}}, k_{bw_{y1}})$  and  $(k_{bw_{x2}}, k_{bw_{y2}})$  are chosen such that window functions  $A_{ifp1}(k_x, k_y)$  and  $A_{ifp2}(k_x, k_y)$  lie wholly within the acquisition apertures of support as illustrated in Figure 8. The terms  $\Delta_1$  and  $\Delta_2$  describe the offset of the window functions from the baseband  $k_y$  origin that arises due to the use of the common baseband spatial frequency  $k_{0g}$ , see Figure 8.

Applying the image formation windows to the primary and secondary acquisition signal history data given in (33) and (34) followed by an inverse Fourier transform gives the following ground plane interferometric image pair,

$$f(x, y + \Delta_{1y}) = a_1(x, y) \otimes r_{1s}(x, y) \exp(-j(y + \beta_1 h(x, y))k_{0g}), \quad (39)$$

$$g(x, y + \Delta_{2y}) = a_2(x, y) \otimes r_{2s}(x, y) \exp(-j(y + \beta_2 h(x, y))k_{0g}), \quad (40)$$

where  $\otimes$  is the convolution operator and  $\Delta_{1y}$  and  $\Delta_{2y}$  are the layover terms associated with the terrain height function  $h(x, y)$  given by,

$$\Delta_{1y} = h(x, y)\beta_1, \quad (41)$$

$$\Delta_{2y} = h(x, y)\beta_2. \quad (42)$$

The convolution kernels  $a_1(x, y)$  and  $a_2(x, y)$  are the point spread functions of the primary and secondary acquisitions respectively and are given by,

$$\begin{aligned} a_1(x, y) &= \frac{1}{8\pi^3} \iiint A_{ifp1}(k_x, k_y) A_{acq1}(k_x, k_y + k_{0g}, k_z) \\ &\quad \exp(j(xk_x + yk_y)) dk_x dk_y dk_z, \\ &= \frac{k_{bw_{x1}} k_{bw_{y1}}}{4\pi^2} \text{sinc}\left(\frac{xk_{bw_{x1}}}{2\pi}\right) \text{sinc}\left(\frac{yk_{bw_{y1}}}{2\pi}\right) \exp(jy\Delta_1), \end{aligned} \quad (43)$$

and,

$$\begin{aligned} a_2(x, y) &= \frac{1}{8\pi^3} \iiint A_{ifp2}(k_x, k_y) A_{acq2}(k_x, k_y + k_{0g}, k_z) \\ &\quad \exp(j(xk_x + yk_y)) dk_x dk_y dk_z, \\ &= \frac{k_{bw_{x2}} k_{bw_{y2}}}{4\pi^2} \text{sinc}\left(\frac{xk_{bw_{x2}}}{2\pi}\right) \text{sinc}\left(\frac{yk_{bw_{y2}}}{2\pi}\right) \exp(-jy\Delta_2). \end{aligned} \quad (44)$$

## 3.2 Interferometric Processing Modes

It can be seen that the interferometric image pair in equations (39) and (40) contain terms that are dependent on the imaging geometry as well as the surface reflectivity of the scene and the terrain height. The imaging geometry manifests as a height dependent phase modulation in the transduced imagery as well as a height dependent misregistration in the range dimension. The elevation angle also contributes to the size and overlap of the aperture of support functions  $A_{ifp1}$  and  $A_{ifp2}$  which define the point spread functions  $a_1$  and  $a_2$  respectively. By “interfering” the images the scene reflectivity component that is common to both images may be cancelled. The nature of the common scene reflectivity

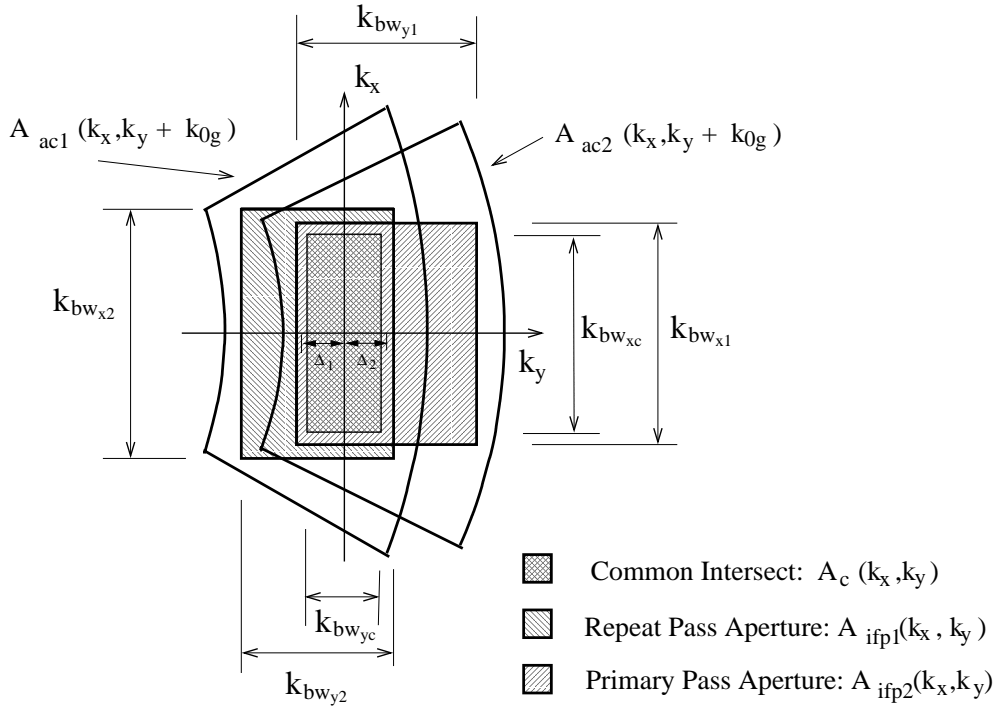


**Figure 8:** Apertures of support in the  $(k_x, k_y)$  plane for the acquisition and image formation transfer functions for a repeat pass image pair after baseband translation. Also shown is the common overlapping aperture of support.

component that is removed by interferometric processing and hence the information content of the interferometric product is dependent on the temporal and geometric baseline between the collections.

The application of SAR interferometry that has received the most attention in the literature has been the topographic mapping application as this allows digital elevation maps of a scene to be generated with unprecedented accuracy, resolution and coverage. Interferometric terrain height mapping is most effective when the image pair acquired simultaneously i.e., without a temporal baseline so that  $r_{1s} = r_{2s}$ , and with a carefully controlled geometric baseline i.e., with a small difference in the depression angle. Returning to equations (39) and (40) and setting  $r_{1s} = r_{2s}$  the phase term  $\phi = (-j\beta_1 h(x, y)k_{0g})$  may be added and subtracted from (40) giving,

$$f(x, y + \Delta_{1y}) = a_1(x, y) \otimes r_{1s}(x, y) \exp(-j(y + \beta_1 h(x, y))k_{0g}), \quad (45)$$

$$g(x, y + \Delta_{2y}) = a_2(x, y) \otimes r_{1s}(x, y) \exp(-j(y + \beta_1 h(x, y))k_{0g}) \exp(j(\Delta\beta)h(x, y)k_{0g}). \quad (46)$$

where  $\Delta\beta = \beta_1 - \beta_2$ . Assuming that the terrain height function varies slowly over the scene and that  $\Delta\beta$  is small then the term  $\exp(j(\Delta\beta)h(x, y)k_{0g})$  may be taken out of the convolution to give,

$$f(x, y + \Delta_{1y}) = a_1(x, y) \otimes r_{1s}(x, y) \exp(-j(y + \beta_1 h(x, y))k_{0g}), \quad (47)$$

$$g(x, y + \Delta_{2_y}) = \exp(j(\Delta\beta)h(x, y)k_{0_g}) [a_2(x, y) \otimes r_{1_s}(x, y) \exp(-j(y + \beta_1 h(x, y))k_{0_g})] . \quad (48)$$

By employing an image registration and resampling algorithm the misregistration  $(\Delta_{1_y} - \Delta_{2_y})$  may be estimated and removed. The image pair thus differ by the phase term,

$$\Delta\Phi = (\beta_1 - \beta_2)h(x, y)k_{0_g}, \quad (49)$$

and the point spread functions  $a_1$  and  $a_2$ . Techniques referred to as aperture trimming may be applied in the image formation algorithm to achieve a common point spread function in which case the image pair differ only by the phase term  $\Delta\Phi$ .

The elevation angles  $\psi_1$  and  $\psi_2$  that determine  $\beta_1$  and  $\beta_2$  in (49) may be computed from the radar platform navigation information while  $k_{0_g}$  is dependent on the radar centre frequency and the common baseline offset chosen during image formation. It is thus possible to compute  $h(x, y)$  given  $\Delta\Phi$ . The phase difference between the interferometric image pair is obtained as the phase of the pixel-wise complex conjugate product of the registered, aperture trimmed image pair,

$$\Delta\Phi_{mod} = \arg\{f(x_1, y_1)g^*(x_1, y_1)\}, \quad (50)$$

where  $(x_1, y_1)$  are the spatial dimensions of the registered image pair. However, the phase of the complex conjugate product only gives  $\Delta\Phi$  modulo  $2\pi$ . The terrain elevation must subsequently be retrieved via application of a phase unwrapping algorithm to remove the  $2\pi$  ambiguity.

The first demonstration of interferometric SAR applied to topographic mapping was obtained using radar observations of the Moon in 1972 [26], [27], [28]. In [27], [28] a radar interferometer was constructed using the Haystack radar system and a nearby communications antenna with subsequent interferometric height measurements yielding an accuracy of better than 500 m. In 1974 Graham [29] applied the technique to radar data of the Earth acquired using an airborne platform followed by more extensive demonstrations of the technique in 1986 by Zebker and Goldstein [30]. However, it wasn't until the launch of the ERS-1 C-band SAR satellite in 1991 by the European Space Agency that high quality, modest resolution imagery, suitable for repeat pass interferometric processing become readily available. The high stability of the satellite and accurate knowledge of its orbital parameters allowed the generation of high quality interferometric phase estimates to assist in the development of phase unwrapping algorithms for the retrieval of terrain topography.

While the terrain mapping application of SAR interferometry uses the geometric baseline to determine terrain height, the change detection application utilises a temporal baseline to measure and detect scene disturbances. By utilising repeat pass acquisitions, each having the same imaging geometry, differences in the amplitude and phase of the transduced imagery may be associated with changes in the scene that arise in the interval between collections.

This method of change detection, commonly referred to as coherent change detection, has the potential to detect very subtle scene changes. From equations (39) and (40) it can be seen that the SAR image is essentially a two dimensional, bandpass filtered version

of the scene's radar reflectivity. In the case of natural distributed scenes such as forests, agricultural fields and bare earth surfaces the scene reflectivity may be decomposed into a large number of independent randomly oriented scatterers each with a random complex reflectivity value. The transduced reflectivity in a given SAR image resolution cell is thus a coherent sum of scattering contributions where the contribution of a given scattering centre is weighted by the point spread function. The transduced reflectivity in a given resolution cell  $f(x, y)$  may be described as a random walk in the complex plane where the measured return is given by vector sum,

$$f(x, y) = \sum_{k=1}^N A_k \exp(j\phi_k). \quad (51)$$

The amplitude  $A_k$ , of each step in the random walk, is given by the amplitude of the scattering centre and the weighting imposed by the SAR point spread function. The phase  $\phi_k$  is determined by the phase of the scattering centre as well as a geometrical component dependent on the line of sight distance from the radar to the scattering centre measured in terms of the radar wavelength. Since the scattering centres are randomly located throughout the scattering scene the phase values  $\phi_k$  are completely random. From this description it can be seen that any disturbance in the scene, such as a random re-arrangement of the scatterers, can lead to significant changes in the phase associated with each scattering centre. This in turn leads to changes in the random walk and hence the transduced amplitude and phase in a given resolution cell. Furthermore while a re-arrangement in the scatterer locations will result in a change in the random walk the total backscattered energy from the scene will not necessarily change as the amplitude of the individual scatterers  $A_k$  has not changed. Consequently such changes will not necessarily be detected by conventional incoherent change detection schemes such as image intensity change detection.

While the coherent change detection technique potentially allows for the detection of very subtle man-made scene changes the sensitivity of the technique also makes it susceptible to high false alarm rates. In particular changes in the scattering nature of the scene due to environmental effects such as wind and rain can obscure changes of interest and lead to false detections. Furthermore the presence of receiver noise in the transduced imagery as well as acquisition and image formation differences that arise due to slight differences in the acquisition geometries can also lead to differences in the transduced amplitude and phase in each resolution cell.

In order to provide some measure of discrimination between such sources of difference in the image pair and accommodate the random noise fluctuations the degree of similarity between the image pair is quantified by the sample coherence. The sample coherence is defined as the magnitude of the sample complex cross correlation coefficient between the image pair,

$$\hat{\gamma} = \frac{|\sum_{k=1}^N f_k g_k^*|}{\sqrt{\sum_{k=1}^N |f_k|^2 \sum_{k=1}^N |g_k|^2}}. \quad (52)$$

The sample cross correlation coefficient measures the average correlation between an image pair over an  $N$  pixel local area in the scene and encodes the degree of scene similarity as a value in the range 0 to 1. Where a scene disturbance causes significant

change in the scattering behaviour the cross correlation coefficient tends to zero. In the absence of scene changes the presence of receiver noise, processing differences will tend to cause small differences between the image pair resulting in coherence values close to but less than one. Environmental effects on the other hand can cause scene changes with the extent of the decorrelation depending on the severity of the effects and the nature of the backscattering scene. In general however, man-made changes of interest such as vehicle tracks can generally be identified as localised areas of low coherence against “undisturbed” areas exhibiting some modest loss of coherence. The scene changes can thus be detected by applying a simple threshold to the sample coherence map evaluated over the scene.

While the potential of interferometric change detection for detecting very subtle scene changes has been known for some time [9] only a few applications of the technique have been reported in the literature. In [1] Corr was able to use imagery acquired with the European ERS-1,2 tandem satellites to detect scene changes caused by the movement of large vehicles over a grassed area in Salisbury Plain, United Kingdom. The modest resolution of the ERS imagery (20 m in range by 6 m in azimuth) however ultimately limited the detection performance achieved by Corr. In order to realise the full potential of the interferometric change detection technique fine resolution imagery commensurate with the size of the changes to be detected is required. This can be seen from an inspection of (52), where if the scene change only occupies a fraction of the local  $N$  pixel area under test then the sample cross correlation coefficient contains a mixture of changed and unchanged pixels thereby giving a non-zero coherence. In [9] results from a coherent change detection experiment carried out using a 1 m resolution X-band airborne SAR developed by Sandia National Laboratories were presented. In these results, changes arising due to earthworks in a land fill site are readily identified including tracks made by a self-loading earthmover as well as the grading of an unpaved road. The finer resolution measurements facilitate the formation of a more robust coherence estimate through increased spatial averaging as well as improving the detection of finer scale scene disturbances.

### 3.3 Processing Effects

In the previous section the utility of the sample cross correlation coefficient for identifying areas subject to scene change was discussed. The sample cross correlation coefficient is an estimate of the true or expected cross correlation coefficient obtained by averaging over a local  $N$  pixel neighbourhood. The true cross correlation coefficient may be decomposed into three main components [2],

$$\gamma = \gamma_{snr} \gamma_{temp} \gamma_{proc}. \quad (53)$$

In the coherent change detection application of interferometry the temporal correlation  $\gamma_{temp}$  is the correlation term of interest as it provides information about scene disturbances. It can be related to the relative backscatter contributions of the stable unchanged scatterers in the scene and the unstable changed scatterers in the scene. Where there are no unstable scatterers  $\gamma_{temp} = 1$  while if there are no stable scatterers  $\gamma_{temp} = 0$ . In the transduced image pair however,  $\gamma_{temp}$  is modulated by the noise and processing correlations  $\gamma_{snr}$  and  $\gamma_{proc}$  respectively. These terms reduce the overall correlation of the transduced image pair and so limit the contrast between regions free of scene change and those subject to some



disturbance. As a consequence the performance of  $\gamma$  and hence its sample estimate  $\hat{\gamma}$  as a change detection statistic is degraded by these terms.

The noise correlation  $\gamma_{snr}$  is a real valued quantity that is determined by the radar hardware and thus is fixed for a given sensor and imaging geometry. The processing correlation  $\gamma_{proc}$  on the other hand is a complex quantity determined by the mismatch between the transfer functions of the primary and repeat pass SAR image formation processors. This mismatch is a source of decorrelation and phase bias in the complex correlation estimate that shall vary spatially over the image. The mismatch must therefore be adequately compensated for if the full potential of interferometric processing is to be realised.

### 3.3.1 Receiver Noise Decorrelation

Coherent radar echo data acquired at each transmit/receive point along the coherent processing aperture is subject to radar receiver noise. The level of this noise is determined by the RF hardware, in particular the amplifying stages in the receive chain, as well as the operating temperature of the system [31]. In the transduced imagery the presence of radar receiver noise is generally modelled as an independent, additive noise source and the cross correlation coefficient associated with the noise terms is given by,

$$\gamma_{snr} = \frac{1}{\sqrt{1 + SNR_1^{-1}} \sqrt{1 + SNR_2^{-1}}}, \quad (54)$$

where  $SNR_1$  and  $SNR_2$  are the signal to noise ratios in the primary and repeat pass images respectively. Generally for a repeat pass SAR system the noise levels in each acquisition are the same thus the noise component of the cross correlation may be simplified to,

$$\gamma_{snr} = \frac{1}{1 + SNR^{-1}}, \quad (55)$$

where  $SNR = SNR_1 = SNR_2$ . Radar systems are generally designed to satisfy some prescribed system noise level in absolute power. Thus the signal to noise power ratio varies as a function of the scene backscatter power. As a consequence the noise component of the cross correlation can vary spatially over the scene as the backscattering nature of the scene changes.

### 3.3.2 Baseline Decorrelation

In acquiring image pairs for change detection analysis it is desirable to acquire the data using exactly the same imaging flight tracks. In this case there is no geometric baseline offset hence the point spread functions and the height dependent image domain phase modulation and layover are the same. Amplitude and phase differences between the image pair may thus be attributed to changes in the scene. In practice however it is not possible to fly the same flight track due to inaccuracies in the platform navigation information. This is particularly true in airborne systems where the effects of wind and turbulence can result in significant flight track offsets. Thus both across and above track offsets can exist between the repeat pass image pair.

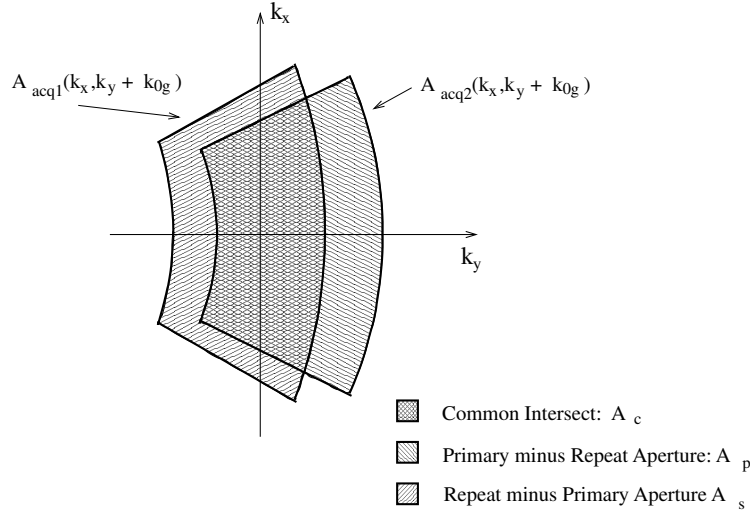


**Figure 9:** Apertures of support in the  $(k_x, k_y)$  plane for the acquisition and image formation transfer functions for a repeat pass image pair after baseband translation. Also shown is the common overlapping aperture of support.

As a consequence the acquired signal history data in the primary and repeat pass acquisitions evaluate samples of the scene's spatial frequency domain representation on two slightly different surfaces. In the ground plane projection ( $k_z = 0$ ) the acquisition apertures of support may be partitioned into three non-overlapping areas: an area common to both the ground plane projection apertures of support,  $A_c$  in Figure 9; an area present in the primary acquisition and not in the secondary acquisition  $A_p$  in Figure 9; an area present in the secondary acquisition and not in the primary acquisition  $A_s$  in Figure 9.

For natural terrain where the scene is described by a large number of independent scatterer elements the scene reflectivity varies independently from resolution cell to resolution cell without any spatial correlation between neighbouring cells. In the spatial frequency domain the energy of the scene is therefore distributed over all frequencies. Furthermore the scene energy at any one frequency is independent of the energy at any other frequency. In forming primary and repeat pass images from the full available apertures  $A_c + A_p$  and  $A_c + A_s$  respectively it is therefore only the common overlapping area  $A_c$  that contributes to the correlation of the image pair. The non-overlapping areas  $A_p$  and  $A_s$  on the other hand only contribute uncorrelated components to the images. It can be shown that the correlation of an image pair formed with a baseline offset is given by,

$$\gamma_{baseline} = \frac{A_c}{\sqrt{(A_c + A_p)(A_c + A_s)}}. \quad (56)$$

It can be seen from Figure 9 that increasing the depression angle difference  $\Delta\psi = \psi_1 - \psi_2$  between the image acquisitions reduces the overlapping aperture size  $A_c$  and hence  $\gamma_{baseline}$ . As the difference is increased a critical baseline is reached for which  $A_c = 0$  and the correlation of the interferometric pair falls to zero. Image pairs suitable for interferometric processing must be acquired so that  $\Delta\psi$  is within the critical baseline limits.

A simple approach to mitigating the baseline decorrelation is to restrict the image

formation processors to only process the common overlapping portion of the acquired data aperture defined by  $A_c$ , such that,

$$A_{ipf_1}(k_x, k_y) = A_{ipf_2}(k_x, k_y) = A_c(k_x, k_y), \quad (57)$$

in which case  $\gamma_{baseline} = 1$ . This method is commonly referred to as aperture trimming. While this approach reduces the processed range and azimuth spatial frequency bandwidth, leading to a reduction in the range and azimuth resolution of the images, the improvement in the processing correlation improves the quality of the subsequent interferometric products.

Another approach to minimising baseline decorrelation proposed in [32] is to consider a Tunable Interferometric SAR system in which the radar transmit frequency is shifted by an amount corresponding to the collection aperture mismatch. In this case the full system bandwidth may be processed giving full resolution interferogram at the expense of increased radar hardware complexity. The approach also facilitates the processing of interferometric pairs with larger baselines than is allowed in a fixed frequency radar collection.

### 3.3.3 Registration

A crucial step to forming an interferometric image pair is to accurately register the image pair. In the presence of geometric baseline offsets geometric misregistration between an image pair naturally arises as a consequence of the differential layover that exists. For a target at location  $(x_s, y_s, h_s)$  imaged with a mid-aperture depression angle of  $\psi_1$ , the target appears at location  $(x_s, y_s + h_s \tan \psi_1)$  in the resulting ground plane image. The differential layover for the same target imaged at a different mid-aperture depression angle  $\psi_2$  is  $\Delta y = h_s(\tan \psi_1 - \tan \psi_2) = h_s \Delta \beta$ . The resulting decorrelation arising from this range misregistration  $\Delta y$  is governed by the point spread function of the acquisition and image formation processor. For the case of an unweighted aperture the decorrelation takes the form of a sinc function namely,

$$\gamma_{rego} = \text{sinc} \left( \frac{h_s \Delta \beta}{\rho_{res}} \right). \quad (58)$$

Observe that for a misregistration of one resolution cell  $h_s \Delta \beta = \rho_{res}$  the correlation falls to zero. An important aspect of the design and implementation of a practical interferometric processor is the estimation and compensation of image misregistration. For fine resolution SAR systems small, sub-resolution cell image misregistrations can have a significant deleterious effect on the performance of interferometric processing. In the change detection application of interferometry, the loss in correlation between a misregistered interferometric pair reduces the contrast between changed and unchanged regions in the scene. Similarly for terrain mapping the loss in correlation contributes to a noisier estimate of the interferometric phase. Aside from layover, other sources contributing to image misregistration in range and azimuth include deviations from the ideal desired flight path as well as navigation measurement errors. An accuracy of 0.1 of a resolution cell is generally considered necessary to achieve high quality coherence estimates [10], [33].

### 3.3.4 Higher Order Effects

Image misregistrations and baseline decorrelation represent the dominant first order effects that must be accurately measured and compensated for to reliably generate good quality coherence estimates. Additional decorrelation sources arise as a result of unmodelled phase terms due to mismatch between the acquisition and image formation functions. In particular the PFA image formation algorithm used in the development of the imaging equations in Section 2 is based on a plane wave model to describe the propagation of the transmitted and received electromagnetic radiation to and from the scene. In the case of wide-band, wide-angle, near-field imaging the plane wave propagation assumption begins to break down and unmodelled wavefront curvature effects appear in the acquisition function which will remain uncompensated by the PFA processor. In the case of SAR interferometry these uncompensated terms manifest themselves as a relative image defocus and misregistration between the primary and secondary images which varies spatially over the images and become progressively larger at the outer edges of the image. These effects however, can be mitigated by using alternative image formation algorithms that explicitly account for wavefront curvature effects.

## 3.4 A Model for a Repeat Pass Image Pair

With accurate image domain registration and aperture trimming the image pair model given in equation (48) may be written as,

$$\begin{aligned} f(x_1, y_1) &= r'_{1_s}(x, y), \\ g(x_1, y_1) &= r'_{2_s}(x, y) \exp(j\Phi), \end{aligned} \quad (59)$$

where  $(x_1, y_1)$  describe the spatial dimensions of the registered image pair, The angle  $\Phi$  is the interferometric height dependent phase term,

$$\Phi = (\beta_1 - \beta_2)h(x, y)k_{0_g}. \quad (60)$$

The scene reflectivity functions  $r'_{1_s}(x, y)$  and  $r'_{2_s}(x, y)$  are given by,

$$r'_{1_s}(x, y) = a(x, y) \otimes r_{1_s}(x, y) \exp(-j(y + \beta_1 h(x, y))k_{0_g}), \quad (61)$$

$$r'_{2_s}(x, y) = a(x, y) \otimes r_{2_s}(x, y) \exp(-j(y + \beta_1 h(x, y))k_{0_g}), \quad (62)$$

where  $a(x, y)$  is the point spread function defined by the common aperture of support obtained after aperture trimming.

In practice however, the common overlap cannot be precisely defined due to errors in the knowledge of the baseline offsets of the image pair over the acquisition apertures. As a result  $r_1$  and  $r_2$  in (59) will contain uncorrelated contributions. Furthermore errors can arise both in the estimation of the image misregistration as well as in the subsequent resampling of the images onto a common spatial grid. Finally additive receiver noise will also contribute to the decorrelation of the primary and repeat pass image pair. Assuming that all these sources of scene decorrelation are independent and contribute as additive decorrelation components to the image pair they can be modelled in the image domain as

additive, mutually independent noise sources  $n_1$  and  $n_2$  in the primary and repeat pass images respectively. Thus a more accurate model to describe the image pair is,

$$f(x_1, y_1) = r'_{1_s}(x, y) + n_1(x_1, y_1), \quad (63)$$

$$g(x_1, y_1) = r'_{2_s}(x, y)\exp(j\Phi) + n_2(x_2, y_2), \quad (64)$$

where  $n_1$  and  $n_2$  are mutually independent of each other and the scene reflectivity functions  $r'_{1_s}(x, y)$  and  $r'_{2_s}(x, y)$ .

Comparing the amplitude and phase of the image pair by taking the complex conjugate product gives,

$$fg^* = r'_{1_s}r'^*_{2_s}\exp(-j\Phi) + r'_{1_s}n_2^* + n_1r'^*_{2_s} + n_1n_2^*. \quad (65)$$

The first term in (65) depends on the scene's reflectivity function and thus contains the useful interferometric information, i.e., it represents the useful signal component in  $fg^*$ . The useful signal component however, is corrupted by contributions dependent on the noise terms  $n_1$  and  $n_2$ . Thus taking the pixel-wise complex conjugate product yields only a poor estimate of the interferometric information. In order to extract the useful interferometric information averaging over a local  $N$  pixel area must be carried out to form a sample complex conjugate product. Considering image pixels in a local area in the scene where the terrain height is approximately constant and the area is subject to the same degree of scene change then the average complex conjugate product is,

$$\sigma_{fg}^2 = E\{fg^*\} \approx \sum_{k=1}^N f_k g_k^*. \quad (66)$$

In this case the useful signal components associated with each pixel in the window will add coherently (in phase) while the noise contributions will add incoherently. The useful interferometric signal component is thus "emphasised" by the summation and yields more robust estimates of the interferometric information. Note that while increasing the estimation window size  $N$  yields improved sample estimates, the size of the window must be restricted to homogeneous areas, that is areas which have the same backscattering characteristics, are subject to the same temporal change processes and have the same terrain height.

## 3.5 A Practical Interferometric Processor

Figure 10 is a flow chart describing the interferometric processing chain required to process the repeat pass interferometric SAR data. The details of the components in the processing chain shall now be discussed.

### 3.5.1 Compute Acquisition Apertures of Support

Given the radar deramp demodulated echo data and associated navigation data the first step in the interferometric processing chain is the computation of the pointing vectors  $[R, \theta, \psi]^T$  describing the location of the radar with respect to the scene focus point at each

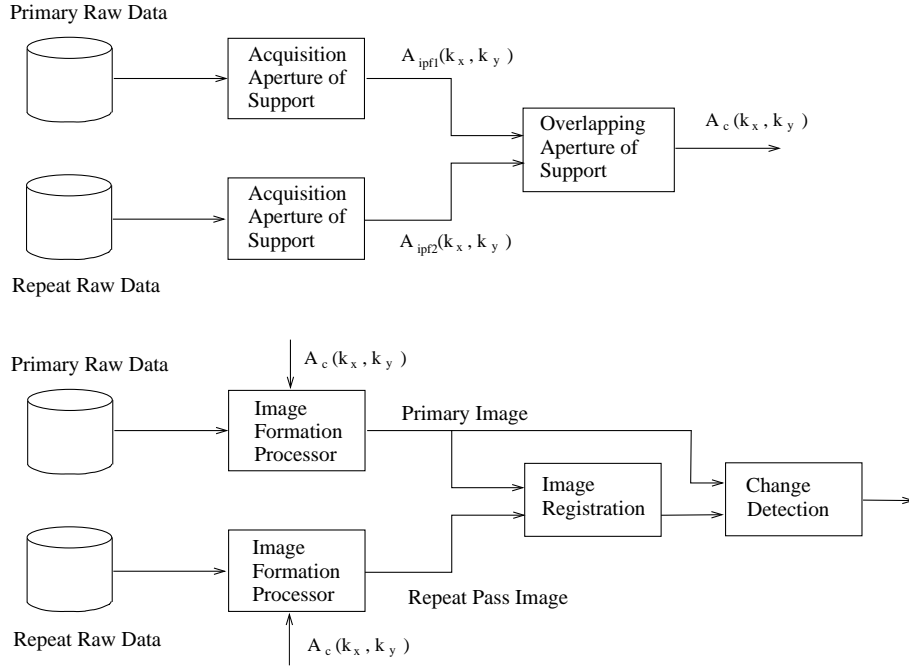


**Figure 10:** Flow chart of the processing steps required to generate an image pair repeat pass SAR data suitable for applying interferometric change detection algorithms.

transmit/receive point along the radar flight track. The radar flight track is measured with high precision using the combined INU and GPS information recorded during the data collection and a common scene focus point is used for the imaging collections. Over a coherent processing interval the pointing vectors associated with each imaging collection define the acquisition apertures of support  $A_{acq1}(k_x, k_y, k_z)$  and  $A_{acq2}(k_x, k_y, k_z)$  for the primary and repeat pass collections respectively.

### 3.5.2 Determine the Common Overlapping Aperture of Support

Given the acquisition apertures of support  $A_{acq1}(k_x, k_y, k_z)$  and  $A_{acq2}(k_x, k_y, k_z)$  for the primary and repeat pass collections the next step is to compute the centre frequency  $k_{0g}$  and bandwidths  $k_{bw_{xc}}$  and  $k_{bw_{yc}}$  of the region given by the common overlapping intersection of  $A_{acq1}$  and  $A_{acq2}$  in the  $(k_x, k_y)$  plane. The depression angles at mid aperture will determine the acquisition aperture mismatch along the  $k_y$  axis and hence the location and size of the common overlapping region.

### 3.5.3 Image Formation

The choice of image formation processor is governed by the processor's ability to adequately focus the scatterer signal history over the coherent processing interval. Generally, efficient frequency domain processors, such as the PFA, make approximations to the scatterer signal history which break down in wideband, wide-angle, near-field imaging. Under these scenarios the imagery suffers from distortion, defocus and a loss in contrast, while

interferometric products suffer from a loss in coherence and increased noise and bias on the interferometric phase estimates. It is thus necessary to ensure the image formation algorithm is able to adequately focus the imagery to the required resolutions given the image size and standoff range, (see (27) and (28)).

### 3.5.4 Image Pair Registration

A plethora of registration techniques exists in the literature for estimating the pixel by pixel misregistration and the subsequent resampling step. In [9] the misregistration over a local neighbourhood of pixels is found by maximizing the complex cross correlation between the image pair over the local area. By obtaining a number of such local spot estimates of the misregistration distributed over the scene a model of the misregistration at all points in the transduced image pair may be obtained by fitting a two dimensional surface function to the sample estimates. An alternative approach proposed in [10] makes use of the phase information available in interferograms obtained from different spectral subapertures. The phase differences may be used to obtain local estimates of the misregistration.

The registration processor used to process the repeat interferometric pairs considered in this work uses a multistage approach similar to that described in [9]:

1. Estimate a coarse global misregistration of the image pair by finding the range and azimuth shift that maximizes the cross correlation of the intensity images.
2. Based on the global misregistration partition the image pair into multiple corresponding image subchips. Compute the intensity cross correlation of the image subchips as a function of misregistration in range and azimuth. Interpolation of the cross correlation map to find the sub-resolution cell location of the correlation map maximum gives a fine registration estimate.
3. Using the multiple local misregistration estimates obtained over the entire scene model the misregistration using a pair of thin plate splines [34], [35]. These splines will describe, for each pixel  $(x, y)$  in the primary image, the location  $(x + \Delta x, y + \Delta y)$  of the corresponding scene resolution cell in the repeat pass image.
4. Using the spline warping function resample the complex repeat pass image onto the sample grid of the primary image using a two dimensional truncated sinc interpolator.
5. Using the complex registered image pair estimate any dominant relative linear phase term between the primary image and the resampled repeat pass image and remove this linear phase term from the repeat pass image.
6. Having removed the dominant relative linear phase from the repeat pass image, recompute the fine registration estimates for the image subchips used in step 2 based on cross correlation of the complex image pair. Cross correlation of the complex transduced imagery produces a sharper correlation peak than cross correlating the image intensities as the cross correlation estimate is now computed using coherent, or vector addition, as opposed to scalar addition. As a consequence a more accurate estimate of the correlation peak lag can be obtained.

7. Recompute the warping surface to describe the misregistration and resample the images to obtained a registered image pair.

### 3.5.5 Interferogram Estimation

A sample complex cross correlation coefficient is formed from an aperture trimmed, registered interferometric image pair by computing,

$$\hat{\gamma} \exp(j\hat{\phi}) = \frac{\sum_{k=1}^N f_k g_k^*}{\sqrt{\sum_{k=1}^N |f_k|^2 \sum_{k=1}^N |g_k|^2}}, \quad (67)$$

over a sliding estimation window. The size of the estimation window is a compromise between obtaining a sufficiently fine resolution cross correlation map, capable of tracking the spatial variation in the underlying complex correlation coefficient and the required accuracy of the estimated quantities. For example, in the change detection application of SAR interferometry wherein man-made scene disturbances such as vehicle tracks are to be detected, the scene correlation can be highly spatially non-stationary with spatially small isolated, abrupt changes. Thus a small window commensurate with the spatial size of the scene disturbances is required. However, if the number of independent pixel samples in the window is too small the estimate will be excessively noisy making it difficult to distinguish between the changed and unchanged regions of the scene.

Another consideration in the formation of an interferogram is the image pixel sampling requirements to ensure alias free interferometric measurements. Given the bandlimited image pair  $f$  and  $g$ , with range and azimuth bandwidths of  $k_{bw_{cx}}$  and  $k_{bw_{cy}}$  respectively, the coherence is estimated by firstly forming the three product images  $|f|^2 = f \cdot f^*$ ,  $|g|^2 = g \cdot g^*$  and  $f g^*$ . These product images are noisy single point estimates of the mean backscatter and cross correlation of the primary and repeat pass images. As multiplication in the image domain corresponds to convolution in the spatial frequency domain the range and azimuth bandwidth of the product images are  $2k_{bw_{cy}}$  and  $2k_{bw_{cx}}$  respectively. Thus in order to avoid aliasing in the product images the image pair  $f$  and  $g$  must first be oversampled by a factor of two.

While the range and azimuth bandwidths of the product images are  $2k_{bw_{cy}}$  and  $2k_{bw_{cx}}$  respectively the underlying scene statistics are assumed to vary only slowly over the spatial estimation window and are modeled as being stationary in increments [36]. High spatial frequency energy in the product images may thus be attributed to noise, while low spatial frequency energy corresponds to the slow variations in the scene statistics permitted by the stationary in increments model. The product images  $|f|^2 = f \cdot f^*$ ,  $|g|^2 = g \cdot g^*$  and  $f g^*$  may thus each be spatially averaged using a  $N$  pixel sliding estimation window which simply functions as a low pass filter that attenuates the high spatial frequency “noise” content of the product image and gives an improved local estimate of the slowly varying scene statistics. As the product images have been low pass filtered they may be used directly in (67) to compute the interferogram without significant aliasing.



### 3.6 Experimental Results

Experimental repeat pass interferometric SAR data collected with the DSTO Ingara SAR has been processed using the techniques discussed in the previous section. Figures 11 and 12 shows the intensity images of a registered, aperture trimmed primary and repeat pass interferometric image pair collected at a nominal depression angle of 30 degrees. The images have been processed using the PFA algorithm and have a 3 dB resolution of 0.58 m in range and 0.15 m in azimuth with a Hamming spectral window applied and a pixel spacing of 0.41 m by 0.1 m. The image is of an open field with a building visible in the lower middle of the image. A drainage trench runs along the left side of the image and a dirt track lies in the upper portion of the image. Both of these scene features appear in the images as areas of low backscatterer return. In the case of the drainage trench the area of low backscatter corresponds to radar shadow while in the case of the dirt track the low backscatterer is possibly due to the passage of vehicles compacting and smoothing the soil and the absence of vegetation in these areas. The baseline offset for this image pair is very small with a depression angle difference of 0.012 degrees and a ground range offset difference of 4.59 m. The temporal baseline for this collection is only 12 minutes corresponding to the time required to maneuver the aircraft back to the start of the imaging track for the repeat pass collection. For this experiment no controlled scene changes were carried out and no ground truth observations were made during the collection interval.

Figures 13 and 14 show the sample coherence and interferometric phase obtained from the repeat pass pair using a 2 (range) by 6 (azimuth) pixel spatial estimation window. The coherence in the field is measured at 0.94 consistent with the small temporal delay and baseline offset between the repeat pass collections. Figure 15 is an enlarged view of the coherence map over the dirt track in the upper portion of the scene. As the track has a low backscatter power the transduced image has a low signal to noise level in these regions and hence there is significant decorrelation. On the other hand the areas between the tracks show high coherence due to the stronger vegetation and ground returns in these areas.

A feature of particular interest in Figure 13 is the random track-like areas of low coherence in the middle of the field. Figure 16 shows an enlarged view of these track-like disturbances. The tracks appear to have a low but non zero coherence possibly because the tracks are on a much finer scale than the resolution of the sample coherence map so the estimation window includes pixels containing both changed and unchanged scattering contributions. In addition a number of the tracks appear to be terminated by a somewhat larger area of very low coherence. It is believed that these low coherence tracks may be due to the movement of sheep while grazing during the 12 minute temporal baseline with the “ends” of the tracks being the sheep themselves. Figure 17 shows an enlarged view of the primary and repeat pass intensity images obtained over one of the tracks. It can be seen that the speckle pattern of the pair of intensity images is nearly identical and there is a significantly stronger return (approximately 3.9 dB stronger) appearing in the centre of the repeat pass image subchip shown in Figure 17 that is absent in the primary intensity image. Unfortunately no ground truth observation were made on the day of the repeat pass collections however grazing sheep were present in the field on the following day.



**Figure 11:** Primary collection intensity image. The image has been processed to a resolution of 0.58 m (range) by 0.150 m (azimuth) with a Hamming window applied.



**Figure 12:** Repeat pass collection intensity image. The image has been processed to a resolution of 0.58 m (range) by 0.150 m (azimuth) with a Hamming window applied. The temporal baseline for the repeat pass interferometric pair is approximately 12 minutes.



**Figure 13:** *Magnitude image of the sample complex cross correlation coefficient obtained by spatially averaging over a sliding estimation window (2 by 6 pixels in range and azimuth respectively).*

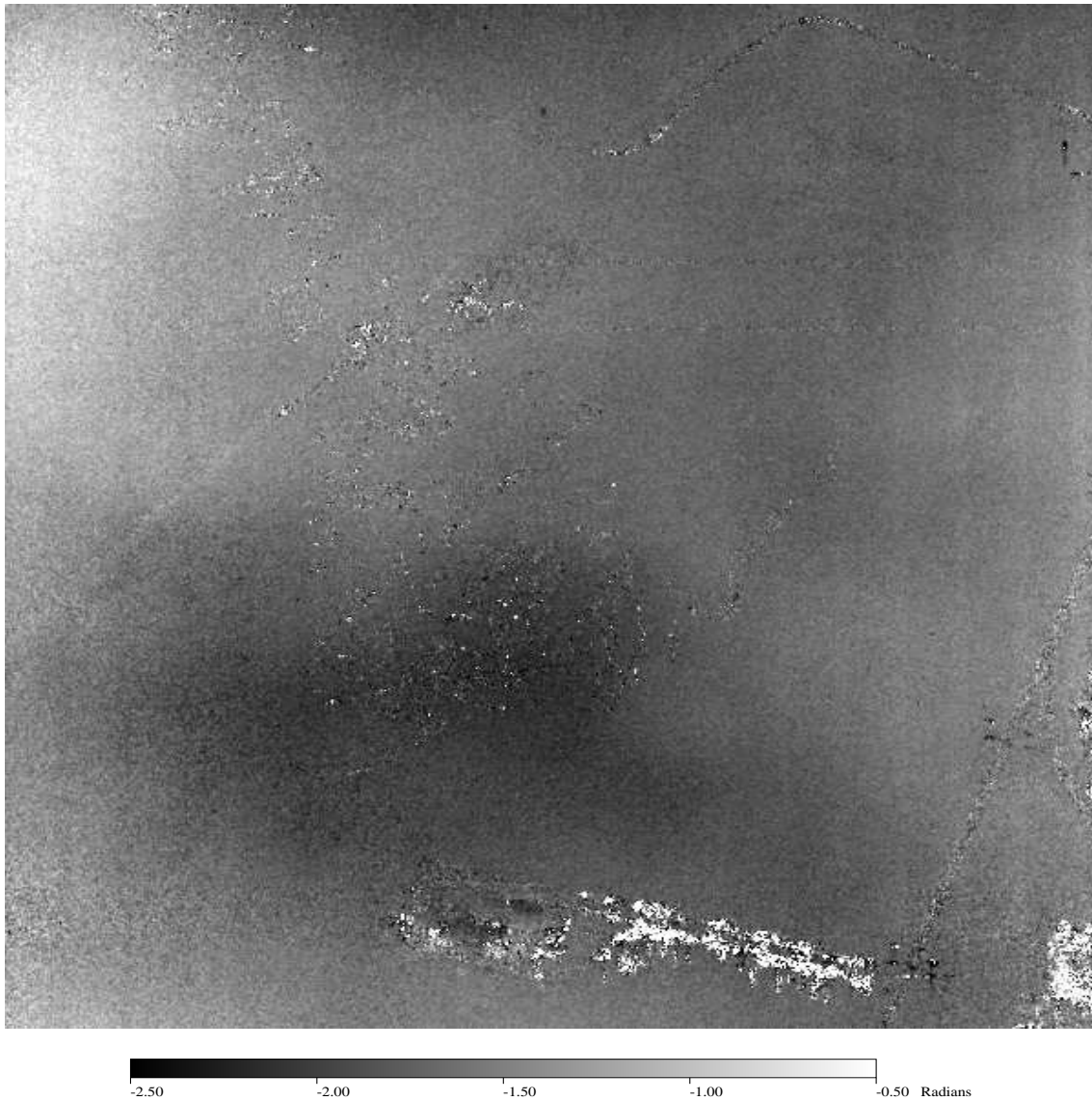


**Figure 14:** Phase image of the sample complex cross correlation coefficient obtained by spatially averaging over a sliding estimation window (2 by 6 pixels in range and azimuth respectively).



**Figure 15:** *Enlarged view of the coherence map over the dirt track that appears along the top of the scene image.*

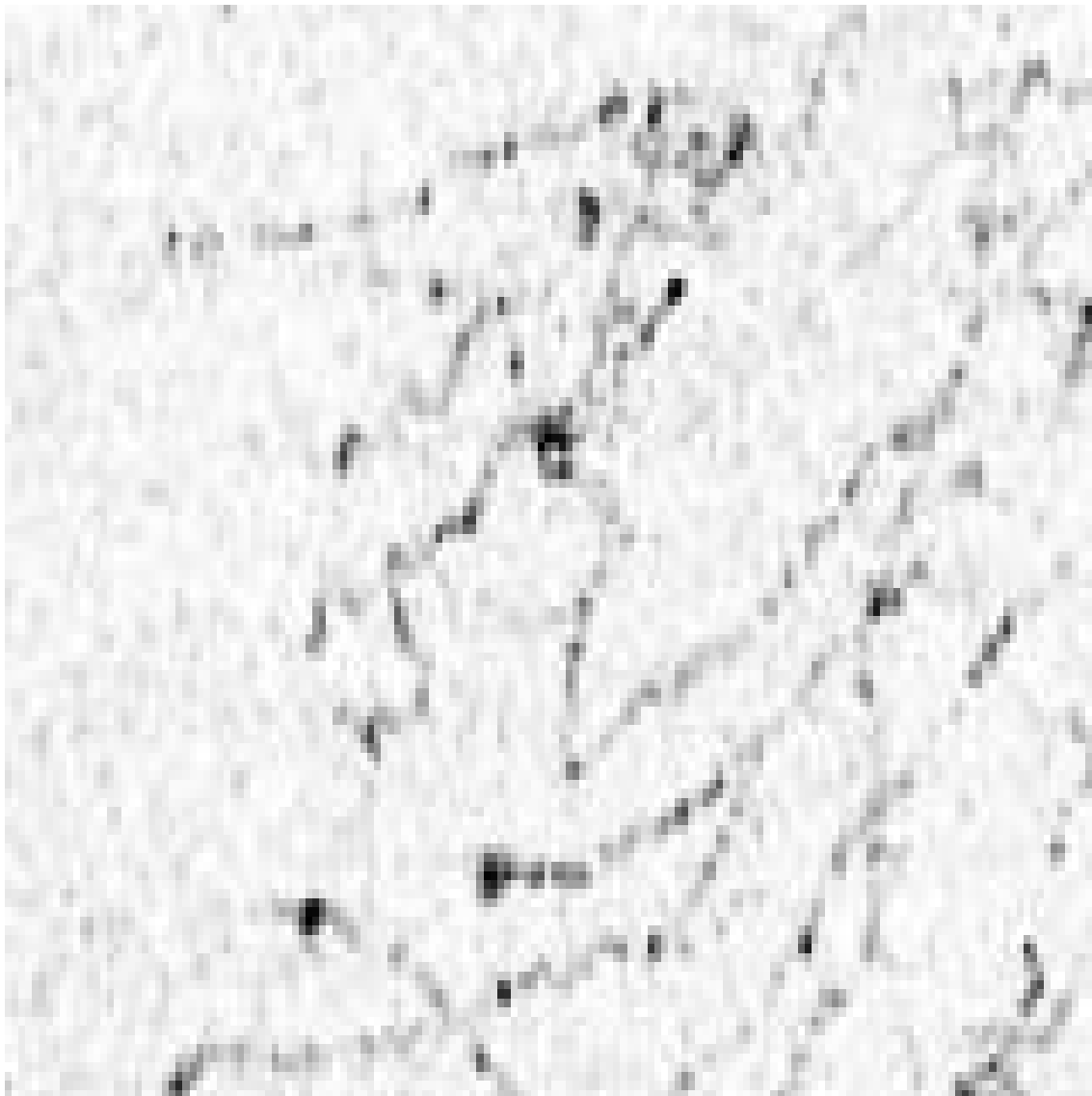


**Figure 16:** *Enlarged view of the coherence map over the low coherence random tracks appearing in middle portion of the scene.*

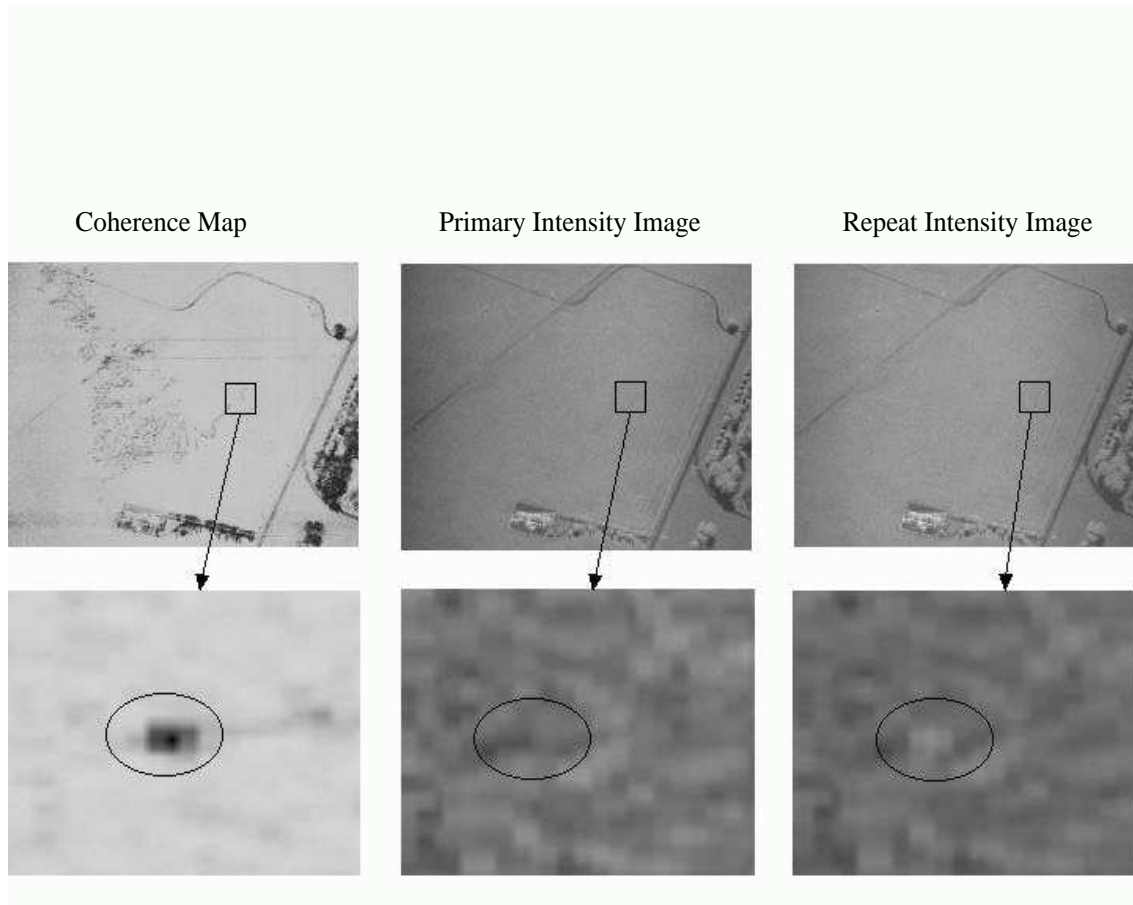


**Figure 17:** Enlarged view of the coherence map as well as the primary and repeat pass intensity images over one of the track like disturbances.



## 4 Interferometric Change Detection

The design of appropriate change statistics for repeat pass interferometric SAR requires an understanding of the information content in a SAR image pair. In the previous section a description of natural distributed scenes was discussed and it was demonstrated that the interferometric information in the repeat pass pair could be recovered by computing the sample complex cross correlation coefficient. In particular the phase of the sample complex cross correlation coefficient could be related to the terrain height while the coherence (i.e., the magnitude sample complex cross correlation coefficient) is a measure of the degree of similarity in the image pair. The scene coherence could subsequently be used as a scene change statistic to identify areas of disturbance in the scene. In this section the distributed target model will be considered to derive a statistical description for repeat pass interferometric SAR in terms of a few key underlying statistical parameters. These parameters may subsequently be used in conjunction with proper statistically based decision/detection theory to obtain scene change metrics and also allow the derivation of their theoretical detection performance.

### 4.1 Statistical Description of Interferometric Image Pair

In Section 3 the random walk model describing the transduced reflectivity in a resolution cell was described for natural distributed scenes such as forests, agricultural fields, soil and rock surfaces. In this model the transduced reflectivity  $f$  in a resolution cell is the coherent sum of a large number of scattering contributions,

$$f = \sum_{k=1}^N A_k \exp(j\phi_k). \quad (68)$$

The amplitude  $A_k$  is the  $k^{th}$  point scatterer amplitude weighted by the SAR point spread function while  $\phi_k$  is determined by the phase of the point scatterer and its line of sight distance from the radar. In the transduced image the scattering centres however, cannot be resolved. Therefore they are not directly observable and a unique description for each scatterer in terms of its spatial location and complex reflectivity is unattainable. Furthermore an arbitrary number of scattering centre realisations will yield the same transduced backscatter in a given resolution cell. The observed scattering behaviour in a resolution cell thus may only be described in a statistical sense in terms of its average characteristics which may be estimated from the transduced image.

Assuming that the scatterers are randomly distributed throughout the scene and given that a resolution cell is typically many wavelengths across, the phase contributions of the scatterers may be considered to be uniformly distributed. Assuming also that the scattering amplitude and phase are statistically independent then, for large  $N$ , it may be shown [37], [38] that the real and imaginary components of the transduced scene reflectivity  $f_r = \Re\{f\}$  and  $f_i = \Im\{f\}$ , are asymptotically, jointly circular zero mean Gaussian random variables with probability density function given by,

$$p(f) = \frac{1}{\pi\sigma_f^2} \exp\left(-\left(\frac{f_r^2 + f_i^2}{\sigma_f^2}\right)\right), \quad (69)$$

where the  $\sigma_f^2$  is the expected value of  $ff^*$ ,

$$\begin{aligned}\sigma_f^2 &= E\{f(x, y)f^*(x, y)\}, \\ &= \sigma_q^2 \iint |a(x, y)|^2 dx dy.\end{aligned}\quad (70)$$

The term  $\sigma_q^2$  is the backscatter power per unit area associated with the point scatterers in the scene while the integral in (70) describes the area footprint of a resolution cell. The distributed scene is thus completely described by a single parameter, namely  $\sigma_f^2$ , which is the mean power in a resolution cell of the transduced image. With this result in mind the transduced scene backscatter may be re-written as,

$$f = \sigma_f(n_r + jn_i), \quad (71)$$

where  $n_r$  and  $n_i$  are jointly circular, zero mean Gaussian random variables with variances of  $\frac{1}{2}$ . In this form the transduced reflectivity may be interpreted as a mean backscatter value  $\sigma_f$  that is modulated by a random noise like term  $(n_r + jn_i)$  that manifests in the transduced imagery as speckle noise. In a single SAR image the noise term does not contribute any useful information to the analysis and interpretation of the imagery, other than indicating that the resolution cells are made up of many individual scattering centres.

In a repeat pass interferometric SAR collection it can be shown that, under certain conditions [12], the joint distribution of the complex interferometric image pair  $\underline{X} = [f, g]^T$  is a jointly circular, zero mean, Gaussian random vector with density function given by,

$$p(\underline{X}) = \frac{1}{\pi^2|Q|} \exp\left(-\underline{X}^H Q^{-1} \underline{X}\right), \quad (72)$$

where  $Q$  is the covariance matrix of the transduced pixel pair given by,

$$Q = E\{\underline{X} \underline{X}^H\} = \begin{bmatrix} \sigma_f^2 & \sigma_f \sigma_g \gamma \exp(j\Phi) \\ \sigma_f \sigma_g \gamma \exp(-j\Phi) & \sigma_g^2 \end{bmatrix}, \quad (73)$$

and  $|Q|$  is the determinant of  $Q$ . The terms down the leading diagonal of  $Q$ , namely  $\sigma_f^2$  and  $\sigma_g^2$ , are the mean backscatter power transduced by the SAR in a pixel for the primary and repeat pass image respectively and have the form,

$$\begin{aligned}\sigma_f^2 &= E\{ff^*\}, \\ &= \sigma_p^2 \iint |a_1(x, y)|^2 dx dy,\end{aligned}\quad (74)$$

and

$$\begin{aligned}\sigma_g^2 &= E\{gg^*\}, \\ &= \sigma_q^2 \iint |a_2(x, y)|^2 dx dy,\end{aligned}\quad (75)$$

where  $\sigma_p^2$  and  $\sigma_q^2$  are the mean backscatter power per unit area associated with the point scatterers in the primary and repeat pass collections respectively. The functions  $a_1$  and  $a_2$  are the point spread functions of the SAR processor in the primary and repeat pass

collections respectively. The additional information made available by considering the interferometric image pair is encapsulated in the complex cross channel correlated coefficient,  $\gamma \exp(j\Phi)$ , given by,

$$\gamma \exp(j\Phi) = \frac{E\{fg^*\}}{\sqrt{E\{|f|^2\}E\{|g|^2\}}}, \quad (76)$$

where  $\gamma$  takes values in the range 0 to 1 from the Cauchy-Schwartz inequality.

An examination of the statistical description of a repeat pass interferometric SAR image pair given in (72) and (73) shows that it is possible to identify man-made scene changes by comparing the mean backscatter power terms  $\sigma_f^2$  and  $\sigma_g^2$  of the primary and repeat pass images and/or by identifying areas of low coherence  $\gamma$ . In regions not affected by man-made scene disturbances, changes in the mean backscatter power and scene decorrelation may still arise due to other sources of scene disturbance such as environmental effects as well as system noise and processing aberrations. Discrimination between these sources of scene change will depend on the nature of the disturbance and its interaction with the scene's scattering layer as well as the sensitivity of the change detection statistic.

## 4.2 Incoherent Change Detection

Incoherent change detection seeks to identify changes in the underlying mean backscatter power of a scene. An estimate of the mean backscatter power  $\sigma_f^2$  may be obtained from a single pixel by computing the pixel intensity  $I = |f|^2$ . This estimate however is corrupted by the speckle noise component, see (71), and in general some form of averaging is required to yield a good quality estimate.

In a homogeneous region, wherein the underlying scattering properties and mechanisms are uniform over the region, the mean backscatter power describing the scene in the transduced image will be constant in that region. The multiplicative speckle noise that manifests itself in each image pixel however, will vary from pixel to pixel due to the particular coherent interfering sub-resolution scattering contributions associated with each resolution cell. Each image pixel may thus be interpreted as a particular realisation of the same underlying random scattering phenomenon and may be averaged to yield an improved estimate of the mean backscatter. An estimate of the mean backscatter power obtained by spatially averaging over  $N$  resolution cells is given by,

$$I = \frac{1}{N} \sum_{k=1}^N I_k, \quad (77)$$

where  $I_k = |f_k|^2$ . Provided the  $N$  pixel realisations,  $I_k$ , are independent then  $I$  in (77) has a gamma distribution with order parameter  $N$  given by,

$$P(I|\sigma_f^2) = \frac{1}{\Gamma(N)} \left( \frac{N}{\sigma_f^2} \right)^N I^{N-1} \exp\left(-\frac{NI}{\sigma_f^2}\right). \quad (78)$$

The  $N$  look intensity average is a consistent estimator of the mean backscatter  $\sigma_f^2$  as the expected value  $E\{I\} = \sigma_f^2$ , and the variance,  $VAR\{I\} = \sigma_f^4/N$ , tends to zero as  $N$  tends

to infinity. The Equivalent Number of Looks ( $ENL$ ), defined as,

$$ENL = \frac{E^2\{I\}}{VAR\{I\}}, \quad (79)$$

indicates the number of independent observations used in a sample estimate of the backscatter. If all  $N$  samples used in (77) are independent then  $ENL = N$ . However, when the  $N$  samples are correlated via the point spread function of the SAR then the  $ENL$  will, in general, be some non-integer value less than  $N$ .

For a repeat pass SAR image pair the  $N$  look sample estimates of the mean backscatter of the primary and repeat pass image pair have density functions given by,

$$P(I_f|\sigma_f^2) = \frac{1}{\Gamma(N)} \left(\frac{N}{\sigma_f^2}\right)^N I_f^{N-1} \exp\left(-\frac{NI_f}{\sigma_f^2}\right), \quad (80)$$

$$P(I_g|\sigma_g^2) = \frac{1}{\Gamma(N)} \left(\frac{N}{\sigma_g^2}\right)^N I_g^{N-1} \exp\left(-\frac{NI_g}{\sigma_g^2}\right), \quad (81)$$

where  $I_f$  and  $I_g$  are the spatially averaged pixel intensities of the primary and repeat pass images respectively and  $\sigma_f^2$  and  $\sigma_g^2$  are the associated scene mean backscatter powers. In the absence of calibration errors such as radiometric miscalibration and antenna pointing errors, regions in the scene that remain undisturbed in the interval between collections have the same mean backscatter power i.e.,  $\sigma_f^2 = \sigma_g^2$ . Areas in which  $\sigma_f^2 \neq \sigma_g^2$ , are indicative of areas of scene change.

A common approach to detecting changes in the image intensity of non-coherent data sets (eg: passively sensed data) [39] is to consider the difference statistic,

$$D = I_f - I_g = \sum_{k=1}^N |f_k|^2 - \sum_{k=1}^N |g_k|^2. \quad (82)$$

This statistic however is found to be ill-suited to change detection in SAR imagery [23], [36] and [40]. Under the premise that the two measurements of the scene's radar reflectivity are independent [23], the variance of the difference statistic is simply the sum of the variances of the two intensity estimates,

$$var\{D\} = \frac{\sigma_f^2 + \sigma_g^2}{N}. \quad (83)$$

Therefore application of a simple threshold detector to the difference statistic to distinguish between areas of differing mean backscatter will have an error performance dependent on the mean backscatter. For example, in areas of no change in backscatter,  $\sigma_f^2 = \sigma_g^2$ , the probability of false alarm for the threshold detector (i.e., labelling a pixel pair in an unchanged scene as having changed backscatter values) will be lower in areas of lower mean backscatter power.

An alternative approach to forming a change statistic is to consider the log intensity estimate as it has a variance independent of the absolute value of the mean backscatter.

The difference of the log intensity estimates,

$$D_L = \log(I_f) - \log(I_g), \quad (84)$$

$$= \log\left(\frac{I_f}{I_g}\right), \quad (85)$$

or alternatively the ratio change statistic,

$$\hat{R} = \exp(D_L) = \frac{I_f}{I_g}, \quad (86)$$

are commonly used in SAR image change statistics. The ratio change statistic has a density function given by [41],

$$p(\hat{R}|R) = \frac{(2N-1)!}{((N-1)!)^2} \frac{R^N \hat{R}^{N-1}}{(R + \hat{R})^{2N}}, \quad (87)$$

where  $R = \frac{\sigma_f^2}{\sigma_g^2}$ . The mean and variance of  $\hat{R}$  are given,

$$E\{\hat{R}\} = \frac{N}{N-1}R, \quad (88)$$

$$Var\{\hat{R}\} = \left( \frac{N(2N-1)R}{(N-1)^2(N-2)} \right)^2, \quad (89)$$

and are dependent only on the relative backscatter ratio  $R = \sigma_f^2/\sigma_g^2$  and the number of independent samples  $N$ . The ratio statistic  $\hat{R}$  takes values in the range  $(0, \infty)$  and in practice requires two thresholds to identify scene changes causing either a reduction or an increase in the mean backscatter power. A more convenient detector proposed by Touzi [41] based on the ratio statistic is,

$$\hat{r} = \begin{cases} \hat{R}, & \text{if } \hat{R} \leq 1, \\ \hat{R}^{-1}, & \text{if } \hat{R} > 1. \end{cases} \quad (90)$$

This statistic takes values between 0 and 1 and a single threshold may be applied to generate change detections. The probability density function is given by [41],

$$p(\hat{r}|R) = \frac{\Gamma(2N)}{\Gamma(N)^2} \left( \frac{R^N}{(\hat{r} + R)^{2N}} + \frac{R^{-N}}{(\hat{r} + R^{-1})^{2N}} \right) \hat{r}^{N-1}. \quad (91)$$

Figure 18 shows simulated and theoretical density functions for the ratio statistic for an unchanged scene in the absence of calibration errors (equal mean backscatter power) and a scene with a 3 dB change in the mean backscatter power between image collections obtained using  $N = 9$  independent samples. The performance of the ratio statistic  $\hat{r}$  may be gauged by the degree of overlap of the two density functions shown in Figure 18. Using a simple threshold detector, pixel pairs with ratio values greater than some threshold  $T$ , ( $\hat{r} > T$ ), are labelled as being unchanged and pixel pairs with ratio values less than  $T$ , ( $\hat{r} < T$ ), are labelled as being changed. The probability of correctly making a change detection corresponds to the area under the changed density function in Figure 18 to the left of the ratio threshold  $T$ , while the probability of a false alarm corresponds

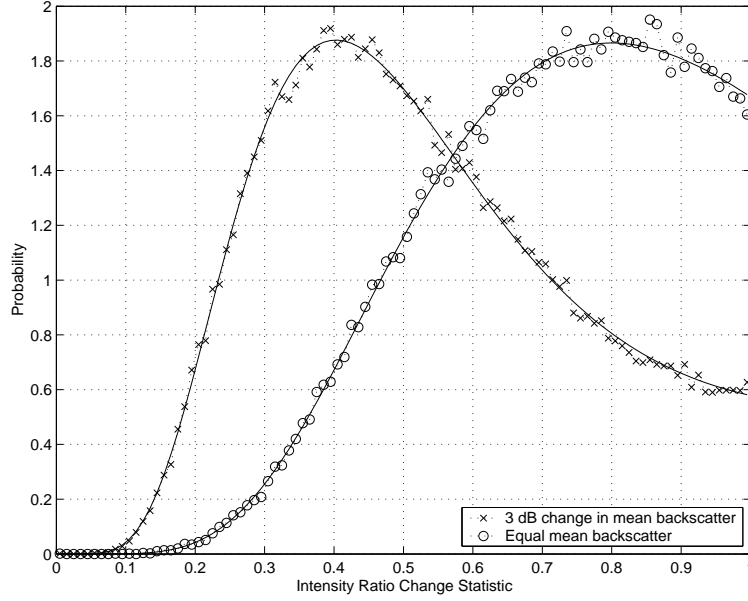


**Figure 18:** Simulated and theoretically obtained density functions for the mean backscatter ratio change statistic corresponding to an unchanged scene and a scene with a 3 dB change in the backscatter. The number of independent averages used in the intensity estimates is  $N = 9$ .

to the area under the unchanged density function to the left of the ratio threshold  $T$ . Analytical expressions for the probability of detection and the probability of false alarm may be computed by evaluating the following integrals. The probability of false alarm is given by,

$$\begin{aligned}
 P_{fa} &= \int_0^T p(\hat{r}|R = R_0)d\hat{r}, \\
 &= \frac{\Gamma(2N)}{\Gamma^2(N)} \int_0^T \left( \frac{R_0^N}{(\hat{r} + R_0)^{2N}} + \frac{R_0^{-N}}{(\hat{r} + R_0^{-1})^{2N}} \right) \hat{r}^{N-1} d\hat{r}, \\
 &= \frac{\Gamma(2N)T^N}{\Gamma(N-1)} \left( \frac{1}{R_0^N} {}_1F_2 \left( 2N, N, N-1, \frac{T}{R_0} \right) + R_0^N {}_1F_2 (2N, N, N-1, TR_0) \right), \quad (92)
 \end{aligned}$$

where  $R_0 = \sigma_f^2/\sigma_g^2$  with  $\sigma_f^2$  and  $\sigma_g^2$  taken to be the mean backscattered power in the unchanged regions of the scene. In the absence of miscalibration errors  $R_0 = 1$  however, in practice radiometric miscalibration and antenna pointing errors may yield  $R_0 \neq 1$ . The probability of detection is,

$$\begin{aligned}
 P_d &= \int_0^T p(\hat{r}|R = R_1)d\hat{r}, \\
 &= \frac{\Gamma(2N)}{\Gamma^2(N)} \int_0^T \left( \frac{R_1^N}{(\hat{r} + R_1)^{2N}} + \frac{R_1^{-N}}{(\hat{r} + R_1^{-1})^{2N}} \right) \hat{r}^{N-1} d\hat{r}, \\
 &= \frac{\Gamma(2N)T^N}{\Gamma(N-1)} \left( \frac{1}{R_1^N} {}_1F_2 \left( 2N, N, N-1, \frac{T}{R_1} \right) + R_1^N {}_1F_2 (2N, N, N-1, TR_1) \right), \quad (93)
 \end{aligned}$$

where  $R_1 = \sigma_f^2/\sigma_g^2$  with  $\sigma_f^2$  and  $\sigma_g^2$  taken to be the mean backscattered power in the changed regions of the scene in the primary and repeat pass images respectively. In equations (92) and (93)  ${}_1F_2$  is the hypergeometric function given in equation 15.3.1 in [42].

Figure 19 shows simulated and theoretical ROC curves (plots of the probability of detection versus the probability of false alarm) for the ratio detector obtained with  $R_0 = 0$  dB and  $R_1 = 1, 3, 5$  and 10 dB and  $N = 9$ . It is clear that for small changes in the mean backscatter power the detector suffers from a significant false alarm rate. To achieve a probability of detection of 0.7 for a mean backscatter power change of 3 dB the associated probability of false alarm is unacceptably high at 0.35. The false alarm rate may be reduced by increasing the estimation window size and hence the value of  $N$ . Figure 20 shows the ROC performance associated with a mean backscatter power change of 3 dB as the ENL is increased. Increasing the ENL from 9 to 36 provides approximately an order of magnitude improvement in the false alarm rate. This performance improvement however, is only realised if the scene's mean backscatter power over the estimation window is locally stationary. In the change detection application the estimation window must be commensurate with the size of the scene disturbances to be detected otherwise the change statistic local estimate contains contributions from changed and unchanged image pixels and the improvements suggested in Figure 20 are not realised.

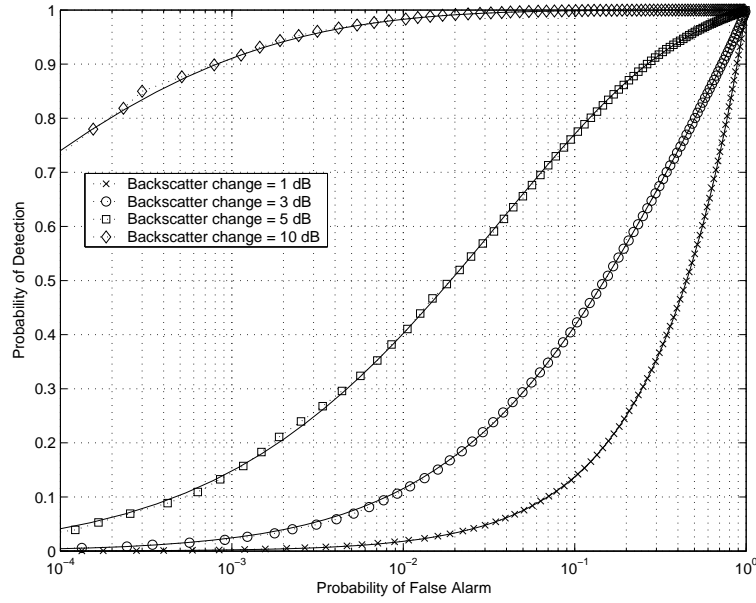


**Figure 19:** Simulated and theoretical ROC curves for the intensity ratio change statistic obtained using an  $N = 9$  and mean backscatter power changes of 1, 3, 5 and 10 dB.

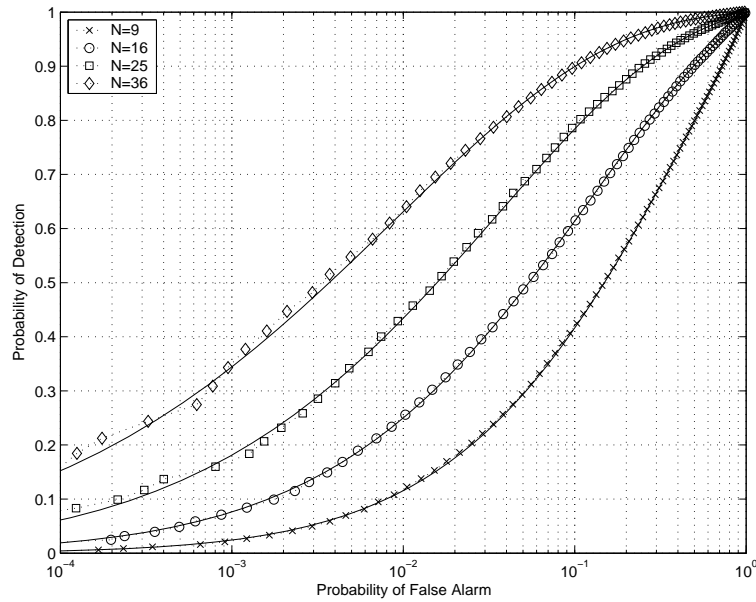


**Figure 20:** Simulated and theoretical ROC curves for the intensity ratio change statistic for a mean backscatter power change of 3 dB and values of  $N$  of 9, 16, 25 and 36.



### 4.3 Coherent Change Detection

The true underlying complex cross correlation coefficient of two complex SAR images  $f$  and  $g$  given by,

$$\gamma \exp(j\Phi) = \frac{E\{fg^*\}}{\sqrt{E\{|f|^2\}E\{|g|^2\}}}, \quad (94)$$

quantifies the extent to which the scene reflectivities and associated SAR image processors are common between the two transduced images. Provided the image pair are appropriately aperture trimmed and registered the impact of image processor mismatch may be minimised and the cross correlation is a measure of the scene disturbance between the imaging collections.

The interferometric phase  $\Phi$ , in the absence of any processing aberrations and scene disturbances, is determined by the baseline offset between the primary and repeat pass collections and the terrain topography plus any bulk displacement of the scattering scene between the two data collections. Change detection based on measurement of the phase shift associated with the bulk displacement is called differential interferometry and may be used to monitor small scale surface deformations that typically arise in glaciers or tectonic plate activity such as earthquakes [43]. For the case of random, zero mean scatterer displacement there is no bulk displacement and change detection can be performed on the associated loss in the magnitude of the cross correlation coefficient,  $\gamma$ , commonly referred to as the coherence. The coherence takes values in the range 0 to 1 and is sensitive to relatively small changes in the distribution of scatterers within a resolution cell.

For the case when the two channels are jointly Gaussian the image pair  $f$  and  $g$  may be expressed as a mean backscatter power coefficient modulated by a unit variance complex Gaussian speckle noise,

$$f = \sigma_f(m_r + jm_i), \quad (95)$$

$$g = \sigma_g(n_r + jn_i), \quad (96)$$

where  $m_r + jm_i$  and  $n_r + jn_i$  are the unit variance speckle noise components of the two channels and  $\sigma_f^2$  and  $\sigma_g^2$  are the mean backscatter powers. In analyzing a single SAR image the information bearing quantity is the mean backscatter, while the speckle noise simply indicates that the resolution cell consists of interfering contributions from a large number of scattering centres. In interferometric analysis however, the speckle noise is the source of the additional information that is provided by the joint processing of an image pair. Substituting (95) and (96) into (94) gives,

$$\begin{aligned} \gamma &= \frac{\sigma_f \sigma_g |E\{(m_r + jm_i)(n_r - jn_i)\}|}{\sigma_f \sigma_g}, \\ &= E\{(m_r + jm_i)(n_r - jn_i)\}. \end{aligned} \quad (97)$$

The correlation coefficient is thus statistically independent of the mean backscatter power  $\sigma_f^2$  and  $\sigma_g^2$  of the scene and is solely determined by the speckle noise in the two channels. The sensitivity of the coherence as a change statistic arises because the speckle component of the transduced complex reflectivity is dependent on the coherent interference of a large number of complex scattering contributions.

The sensitivity of the correlation coefficient to perturbations to the scatterers and their relative arrangement within a resolution cell has been investigated by Zebker [2]. In [2] Zebker considered the point scatterer model for a natural distributed target scene and proposed a probabilistic model for the scatterer displacement between imaging observations. Assuming that each scattering centre in the scene is subject to a random independent displacement in all three dimensions: range, azimuth and height, each described by a Gaussian probability density function Zebker found that the cross correlation coefficient is given by,

$$\gamma_{phase} = \exp \left( -\frac{1}{2} \left( \frac{4\pi}{\lambda_{eff}} \right)^2 \left( \sigma_y^2 \cos^2(\psi_2) + \sigma_z^2 \sin^2(\psi_2) \right) \right), \quad (98)$$

where,

$$\lambda_{eff} = \frac{4\pi}{k_{0g}} \cos(\psi_2), \quad (99)$$

$\psi_2$  is the repeat pass depression angle at aperture centre. and  $\sigma_y^2$  and  $\sigma_z^2$  are the variances of the random Gaussian displacements in the range and height dimensions respectively.

Figure 21 shows the cross correlation coefficient in (98) as a function of the RMS displacement, normalised by the radar wavelength ( $\sigma_y/\lambda_{eff}$ ), for a Gaussian random displacement in range only (i.e.,  $\sigma_z^2 = 0$ ). The cross correlation coefficient has been computed for depression angles of 15 and 45 degrees. It can be seen that total decorrelation of the image pair occurs for an RMS displacement of approximately 20 percent of the radar wavelength. For an X-band radar with a wavelength of the order of 3.2 cm this corresponds to a standard deviation of 0.64 cm. Man-made disturbances such as vehicle tracks across a grass field which can cause significant scatterer displacement can thus potentially cause complete loss in coherence without any appreciable change in the mean backscatter power of the scene. The detectability of such man-made disturbances however may be compromised by other sources of temporal disturbance such as wind and rain. Such disturbances can cause a change in the complex reflectivity of the scattering contributions within resolution cells as well as random perturbations in the scatterer spatial locations leading to an overall loss in the scene coherence. Change detection using the scene coherence thus relies on adequate contrast between the man-made disturbance and other sources of temporal decorrelation.

#### 4.3.1 The Sample Cross Correlation Coefficient Change Statistic

A simple threshold change detector based on the sample coherence evaluated over an N pixel window,

$$\hat{\gamma} = \frac{|\sum_{k=1}^N f_k g_k^*|}{\sqrt{\sum_{k=1}^N |f_k|^2 \sum_{k=1}^N |g_k|^2}}, \quad (100)$$

may be used to identify regions of low coherence and hence detect areas of man-made scene change. The performance of this detector however, is dependent on the statistical

properties of the sample coherence and the contrast in coherence between the disturbed low coherence areas and the unchanged partial coherence areas.

The density function of the sample coherence is given by [44],

$$\begin{aligned} p(\hat{\gamma}|\gamma, N) &= 2(N-1)(1-\gamma^2)^N \hat{\gamma}(1-\hat{\gamma}^2)^{(N-2)} {}_2F_1(N, N; 1; \gamma^2 \hat{\gamma}^2), \\ &= \frac{2(1-\gamma^2)^N \hat{\gamma}(1-\hat{\gamma}^2)^{(N-2)}}{\Gamma(N)\Gamma(N-1)} \sum_{l=0}^{\infty} \left[ \frac{\Gamma(N+l)}{\Gamma(l+1)} \right]^2 (\gamma \hat{\gamma})^{2l}, \end{aligned} \quad (101)$$

where  ${}_2F_1$  is the Gauss hypergeometric function. The density function is dependent on the underlying scene coherence  $\gamma$  and the number of independent pixels  $N$  used in the estimation window. Insight into the nature of this dependence may be obtained by computing the mean of the sample coherence which is given by,

$$E\{\hat{\gamma}\} = (1-\gamma^2)^N \Gamma(N) \frac{\Gamma\left(\frac{1}{2}+1\right)}{\Gamma\left(\frac{1}{2}+N\right)} {}_3F_2\left(\frac{1}{2}+1, N, N; 1, \frac{1}{2}+N; \gamma^2\right), \quad (102)$$

where  ${}_aF_b$  is the generalised hypergeometric function [42]. Figure 22 shows the mean of the sample coherence  $\hat{\gamma}$  as a function of the true coherence  $\gamma$  for various values for  $N$ . From Figure 22 it is clear that for low values of underlying coherence the sample coherence is significantly biased towards higher values. This reduces the contrast of the sample coherence map especially in regions of differing low coherence indicating that large values of  $N$  are required to achieve good change detection performance from the sample coherence.

The detection performance of the sample coherence change statistic may be quantified by comparing the probability density functions of the change statistic for changed and unchanged scenarios. The preceding discussion indicated that man-made changes such as vehicle tracks may be characterised by  $\gamma_{changed} = 0$ . The degree of partial coherence characterising the undisturbed regions on the other hand will depend on the nature of the distributed target, the duration between imaging passes and the severity of the temporal sources of decorrelation as well as the sensor and processing parameters.

The temporal decorrelation of a variety of different target types, sensor bands and repeat pass delays has been studied in the literature [45], [3], [36], [7] and [46]. In [7] Corr examined the coherence of tandem ERS SAR images of forested and cultivated scenes in south east England. Temporal baselines of 3, 6, 12, 21 and 69 days were obtained over the scenes during summer and a 35 day separation was recorded during winter. For temporal baselines of 35 days or more the coherence of the woodland was found to be around 0.2 irrespective of the season while the 3 day coherence was reported to be approximately 0.4. Over the cultivated fields a high scene coherence of approximately 0.9 was obtained in the 3 day coherence map and this decreased slowly to around 0.4 in the case of the 69 day temporal separation. In summer it was found the 35 day coherence was only 0.2 owing to the rapid growth of the field crops. These observations are in broad agreement with numerous other analyses reported in the literature [45], [3] over similar target types. Thus for a range of target scenes, temporal delays and environmental conditions, the “unchanged” areas of a scene may be characterised by some non-zero coherence  $\gamma_{unchanged} > 0$  thereby allowing coherent change detection to be performed.

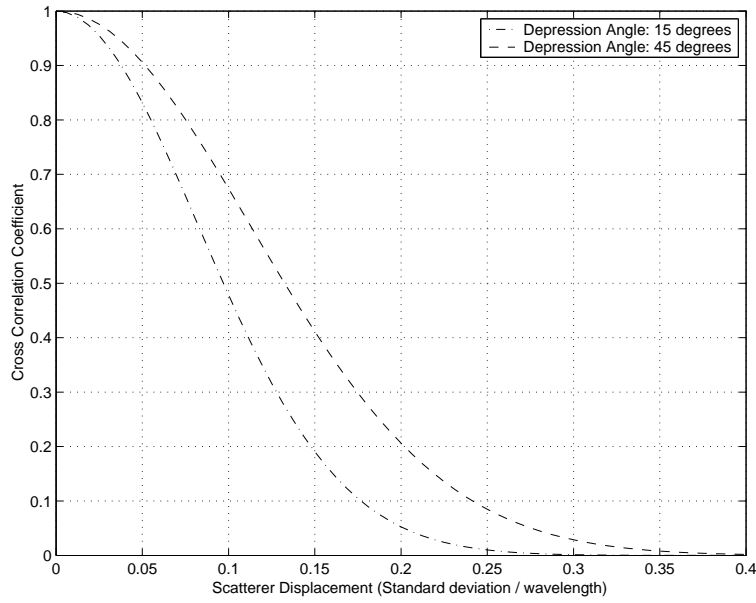


**Figure 21:** Phase component of the cross correlation coefficient of an interferometric image pair where the scatterers in the scene have been subject to a random Gaussian displacement in range and imaged with depression angles of 15 and 45 degrees. The RMS displacement has been normalised to the effective radar wavelength.

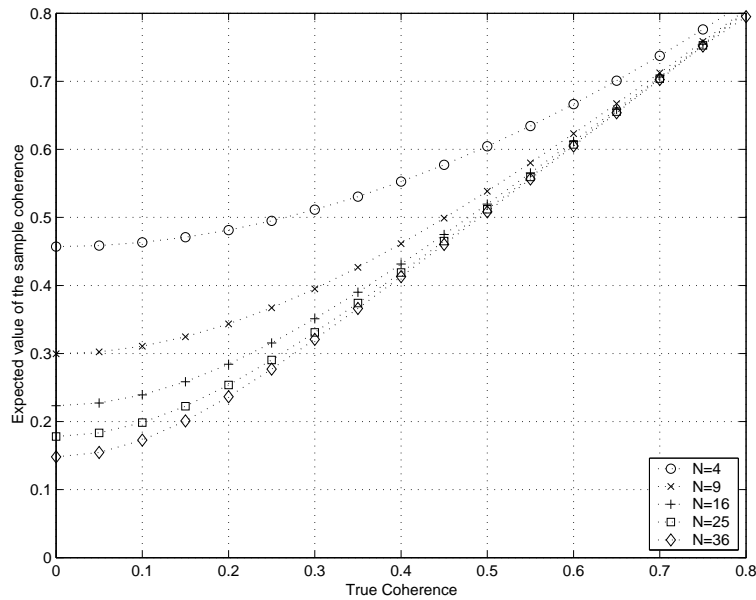


**Figure 22:** Expected value of the coherence estimate plotted against the underlying true coherence for a range of sample estimate sizes.

Figure 23 shows the density functions associated with a scene characterised by an underlying coherence of  $\gamma_{unchanged} = 0.6$  (this being the aggregate decorrelation attributed to environmental effects, processing mismatch and system noise) and a man-made disturbance characterised by a total loss in coherence  $\gamma_{changed} = 0$ .

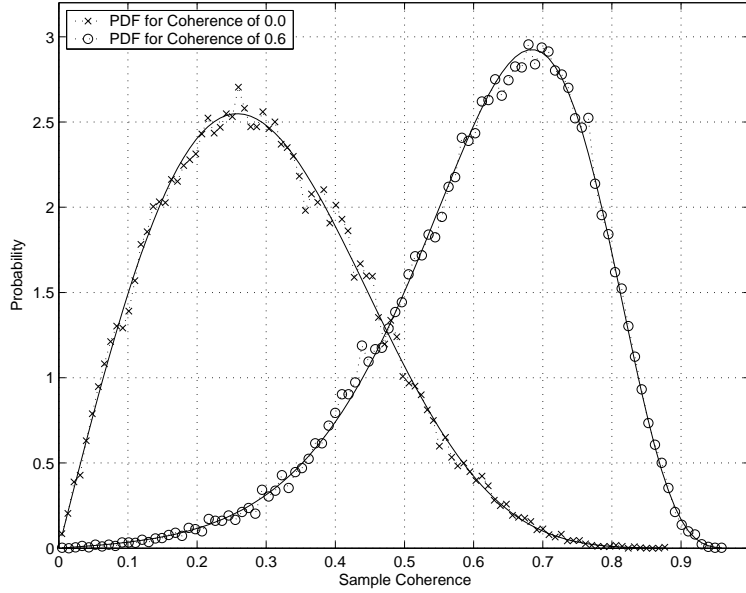


**Figure 23:** Simulated and theoretical probability density functions of the sample coherence corresponding to a true underlying coherence of 0 and 0.6. The sample estimate has been obtained by averaging over  $N = 9$  independent pixel pairs.

A simple threshold detector applied to the sample coherence may be used distinguish between the changed and unchanged regions in the scene. The performance of the detector may be evaluated by computing the associated ROC curve which indicates, for a given detection threshold  $T$ , the probability of detecting a changed pixel  $P_d$  and the corresponding probability of a false alarm  $P_{fa}$ ,

$$P_d = \int_0^T p(\hat{\gamma} | \gamma = \gamma_{changed}) d\hat{\gamma}, \quad (103)$$

$$P_{fa} = \int_0^T p(\hat{\gamma} | \gamma = \gamma_{unchanged}) d\hat{\gamma}. \quad (104)$$

Substituting the density function given in (101) into (103) and (104) gives the following series solution for the probability of detection and false alarm as a function of the number of samples  $N$ ,  $\gamma_{unchanged}$  and  $\gamma_{changed}$ ,

$$P = \frac{2(N-1)(1-\gamma^2)^N}{\Gamma(N)\Gamma(N-1)} \sum_{k=0}^{N-2} \left[ \binom{N-2}{k} (-1)^{N-2-k} \sum_{l=0}^{\infty} \left[ \frac{\Gamma(N+l)}{\Gamma(l+1)} \right]^2 \gamma^{2l} \frac{T^{2N+2l-2-2k}}{2N+2l-2-2k} \right], \quad (105)$$

where,

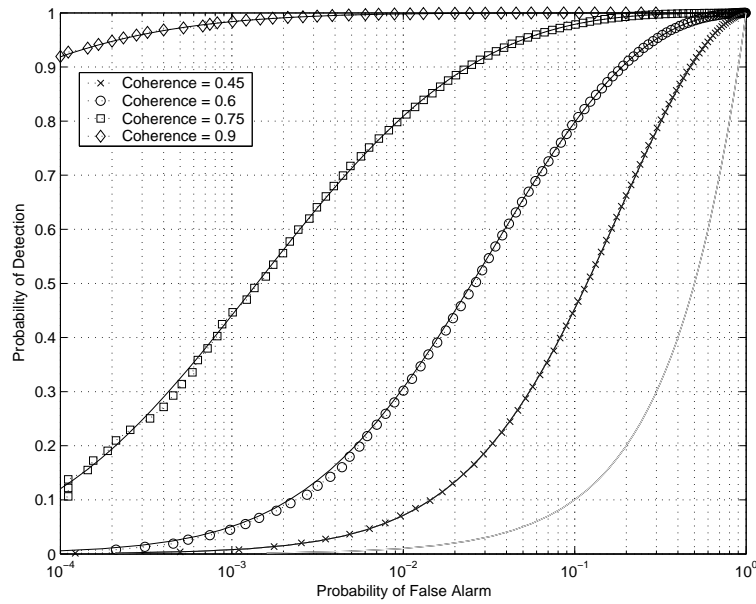
$$P = \begin{cases} P_d, & \text{for } \gamma = \gamma_{changed}, \\ P_{fa}, & \text{for } \gamma = \gamma_{unchanged}. \end{cases} \quad (106)$$

In the case when  $\gamma_{changed} = 0$  then  $P = P_d$  reduces to the following form,

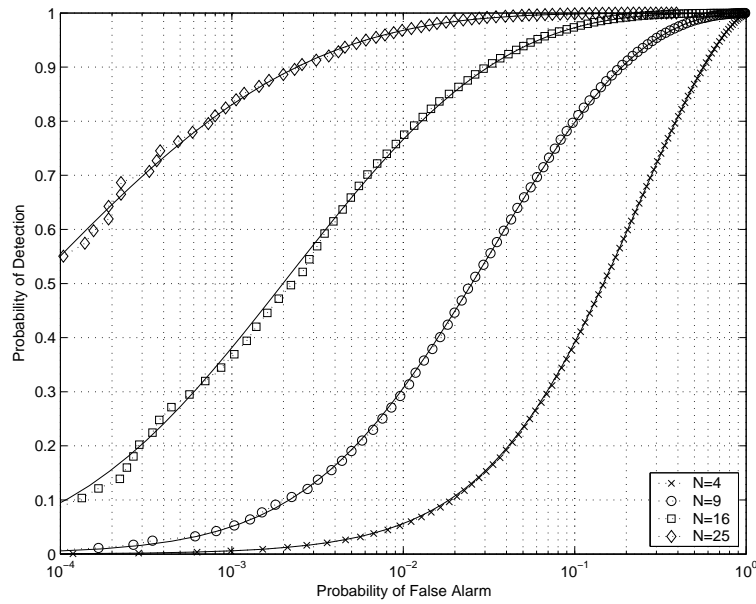
$$P = 2(N-1)^2 \sum_{k=0}^{N-2} \binom{N-2}{k} (-1)^{N-2-k} \frac{T^{2N-2-2k}}{2N-2-2k}. \quad (107)$$

Figure 24 shows the ROC curves for  $N = 9$ ,  $\gamma_{changed} = 0$  and  $\gamma_{unchanged} = 0.45, 0.6, 0.75$  and  $0.9$ . A comparison of Figure 24 with the ROC curve for the backscatter ratio change statistic in Figure 19 shows that for an estimation window size of  $N = 9$  pixels and a  $P_d = 0.7$  a change in the mean backscatter power of 5 dB and  $\gamma_{unchanged} = 0.6$  give a similar false alarm rate of 0.07.

The detection performance of the sample coherence change statistic may be improved by increasing the estimation window size. Figure 25 shows the ROC curves for  $\gamma_{unchanged} = 0.6$  and  $\gamma_{changed} = 0.0$  and increasing values of  $N$ . It can be seen that increasing the estimation window size from 9 to 16 pixels reduces the false alarm rate by an order of magnitude. The window size however must be commensurate with the size of the scene disturbances to be detected otherwise the sample coherence contains contributions from changed and unchanged pixels.



**Figure 24:** Simulated and theoretical ROC curves for sample coherence change statistic obtained with an unchanged scene partial coherence  $\gamma_{\text{unchanged}} = 0.45, 0.6, 0.75$  and  $0.9$ , a changed scene coherence of  $\gamma_{\text{changed}} = 0$  and an estimation window size of  $N = 9$  independent pixels



**Figure 25:** Simulated and theoretical ROC curves for sample coherence change statistic obtained with an unchanged scene partial coherence of  $\gamma_{\text{unchanged}} = 0.6$ , a changed scene coherence of  $\gamma_{\text{changed}} = 0$  and estimation window sizes of  $N = 4, 9, 16$  and  $25$  independent pixels

## 5 Log Likelihood Change Statistic

In the previous section it has been shown that in repeat pass interferometric SAR scene disturbances may be identified as areas of low coherence or possibly as areas of changed mean backscatter power. The performance of sample coherence as a change statistic depends on its ability to distinguish between the decorrelation due to the man-made scene disturbances as opposed to other possible sources of temporal decorrelation. While man-made changes typically cause total decorrelation in localised areas of the scene, environmental effects such as wind and rain can also lead to significant decorrelation across the scene, especially for image pairs collected with long revisit periods. As a consequence the sample coherence change detector is susceptible to high false alarm rates. The mean backscatter power of a scene on the other hand is less susceptible to environmental effects such as wind and processing aberrations. However, in order to produce a measurable change in the scene backscatter any man-made disturbances must cause a significant modification to the physical properties of the scattering layer of the scene.

The poor false alarm rate of the sample coherence and mean backscatter power ratio, in cases where there is significant temporal decorrelation or only modest changes in the mean backscatter power, may be mitigated if extensive averaging is carried out. Increased averaging via spatial windows however degrades the resolution of the change maps. Furthermore in regions of scene change local estimates of the change statistics may contain contributions from both changed and unchanged pixels leading to a degradation in the detection performance.

The analysis of the previous section also indicated that the sample coherence and mean backscatter power ratio are sensitive to different, independent properties of a SAR image. The mean backscatter power ratio is sensitive to changes in the average backscattered energy in the transduced imagery. The sample coherence on the other hand is sensitive to changes in the speckle noise pattern in the repeat pass image pair. Scene disturbances arising from man-made changes however, can potentially cause changes over a broad range of scattering properties. In [11] the sample coherence and mean backscatter power ratio were used to detect changes in repeat pass ERS-1 SAR imagery. It was found that the areas of disturbance identified by each method did not necessarily agree and each method gives complementary characterisations of scene changes. Therefore both change statistics should be considered to provide a complete description of scene changes. In the context of change detection this presents problems in fusing the detections from the two change statistics to achieve a single combined detection list in which the probability of detection is maximised whilst minimising the false alarm rate.

An alternative approach to discriminating between those regions affected by man-made scene changes and those that are not can be achieved by formulating the detection problem in an hypothesis testing framework. In this approach the change detection problem is to determine whether pixel pairs  $X_k = [f_k, g_k]^T$ ,  $k = 1 \dots N$  in a local area are realisations of a null (unchanged scene) hypothesis  $H_0$  or an alternative (changed scene) hypothesis  $H_1$ . Based on the jointly Gaussian model for a repeat pass interferometric image pair the density function for a single pixel pair  $X = [f, g]^T$  is given by,

$$p(\underline{X}) = \frac{1}{\pi^2 |Q|} \exp \left( -\underline{X}^H Q^{-1} \underline{X} \right). \quad (108)$$



where  $Q$  is the covariance matrix associated with the pixel pair and  $|Q|$  is the determinant of  $Q$ . Based on the scene change models used in the previous section, under the unchanged scene hypothesis  $H_0$  the covariance matrix takes the form,

$$Q_0 = \begin{bmatrix} \sigma_f^2 & \sigma_f \sigma_{g_0} \gamma_0 \exp(j\Phi_0) \\ \sigma_f \sigma_{g_0} \gamma_0 \exp(-j\Phi_0) & \sigma_{g_0}^2 \end{bmatrix}, \quad (109)$$

while under the changed scene hypothesis  $H_1$  the covariance matrix takes the form,

$$Q_1 = \begin{bmatrix} \sigma_f^2 & 0 \\ 0 & \sigma_{g_1}^2 \end{bmatrix}, \quad (110)$$

The mean backscatter terms  $\sigma_{g_0}^2$  and  $\sigma_{g_1}^2$  describe the mean backscatter power in the repeat pass image under the unchanged and changed scene hypotheses respectively. The scene coherence under the unchanged hypothesis is  $\gamma_0$  while under the changed hypothesis total loss in coherence is assumed.

Given a local neighbourhood of  $N$  independent pixels  $X_k = [f_k, g_k]^T, k = 1 \dots N$  a simple decision statistic for determining whether the pixels are realisations of the unchanged hypothesis or changed hypothesis is the likelihood ratio defined as,

$$\begin{aligned} L &= \frac{P(\underline{X}_1, \underline{X}_2, \dots, \underline{X}_N; H_0)}{P(\underline{X}_1, \underline{X}_2, \dots, \underline{X}_N; H_1)}, \\ &= \prod_{k=1}^N \frac{P(\underline{X}_k; H_0)}{P(\underline{X}_k; H_1)}. \end{aligned} \quad (111)$$

Substituting  $Q = Q_0$  in (108) gives the density function  $p(\underline{X}_k; H_0)$  and  $Q = Q_1$  gives  $p(\underline{X}_k; H_1)$ . Thus (111) becomes,

$$L = \left( \frac{|Q_1|}{|Q_0|} \right)^N \exp \left( -Tr \left\{ (Q_0^{-1} - Q_1^{-1}) \sum_{k=1}^N \underline{X}_k \underline{X}_k^H \right\} \right), \quad (112)$$

where  $Tr\{A\}$  denotes the trace of matrix  $A$ . Taking the log of (112) and ignoring the constant term yields the following decision statistic for discriminating between the two hypotheses,

$$\begin{aligned} z &= Tr \left\{ (Q_0^{-1} - Q_1^{-1}) \sum_{k=1}^N \underline{X}_k \underline{X}_k^H \right\}, \\ &= Tr \{ Q_d G \}, \end{aligned} \quad (113)$$

where  $G = \sum_{k=1}^N \underline{X}_k \underline{X}_k^H$  and  $Q_d = Q_0^{-1} - Q_1^{-1}$ . Discrimination between the two hypotheses is achieved by evaluating  $z$  over the local  $N$  pixel neighbourhood and applying a threshold  $T$ . For  $z > T$  the pixels are labelled as being realisations of the  $H_1$  hypothesis and for  $z < T$  the pixels labelled as being realisations of the  $H_0$  hypothesis.

Note that the matrices  $Q_0$  and  $Q_1$  describing the  $H_0$  and  $H_1$  hypotheses consist of a number of unknown parameters, thus the hypotheses are composite and  $z$  in (113) is referred to as a clairvoyant detector [47]. A clairvoyant detector yields the optimal detection performance achievable given perfect knowledge of the unknown parameters. In practice suboptimal tests are implemented in which the unknown parameters are specified by their maximum likelihood estimates obtained from the data to form a Generalised Likelihood Ratio Test (GLRT) [47].

## 5.1 PDF of Clairvoyant Log Likelihood Change Statistic

Assuming perfect knowledge of the unknown parameters in  $H_0$  and  $H_1$  the probability density function of the clairvoyant detector  $z$  in (113) may be derived by applying a linear transform  $P$  to the image pixel pair vector  $X_k = [f_k, g_k]^T$ . The matrix  $P$  is chosen such that it diagonalises the rank two matrix  $Q_d$ ,

$$\begin{aligned} P^H Q_d P &= \begin{bmatrix} \lambda_1 & 0 \\ 0 & \lambda_2 \end{bmatrix}, \\ &= \text{diag}(\lambda_1, \lambda_2), \end{aligned} \quad (114)$$

where  $\lambda_1$  and  $\lambda_2$  are the eigenvalues of  $Q_d$  and the columns of  $P$  are the corresponding eigenvectors [48]. Furthermore it may be shown that, given the forms for  $Q_0$  in (109) and  $Q_1$  in (110), one of the eigenvectors is negative while the other is positive. In the following analysis it will be assumed that the first eigenvalue is negative and  $\lambda_1$  will be taken to mean the absolute value of the first eigenvalue. (Similar forms for the density functions as those derived in the following analysis may be obtained for the case when the second eigenvalue is negative.) Defining the new transform variables  $u$  and  $v$  such that,

$$\underline{X} = \begin{bmatrix} f \\ g \end{bmatrix} = P \begin{bmatrix} u \\ v \end{bmatrix}, \quad (115)$$

the decision statistic may subsequently be written as,

$$\begin{aligned} z &= \text{Tr} \left\{ Q_d \sum_{k=1}^N \left( \begin{bmatrix} f_k^* & g_k^* \end{bmatrix} \begin{bmatrix} f_k \\ g_k \end{bmatrix} \right) \right\}, \\ &= \text{Tr} \left\{ P^H Q_d P \sum_{k=1}^N \left( \begin{bmatrix} u_k^* & v_k^* \end{bmatrix} \begin{bmatrix} u_k \\ v_k \end{bmatrix} \right) \right\}, \\ &= -\lambda_1 \sum_{k=1}^N |u_k|^2 + \lambda_2 \sum_{k=1}^N |v_k|^2. \end{aligned} \quad (116)$$

In general under the transform  $P$  the new transform variables  $u$  and  $v$  are dependent, zero mean, circular, complex Gaussian random variables with a covariance matrix of the form,

$$C = \begin{bmatrix} C_{11} & \sqrt{C_{11}C_{22}}\rho e^{j\theta} \\ \sqrt{C_{11}C_{22}}\rho e^{-j\theta} & C_{22} \end{bmatrix}, \quad (117)$$

where,

$$C = \begin{cases} P^H Q_0 P, & \text{for } u \text{ and } v \text{ realisations of } H_0, \\ P^H Q_1 P, & \text{for } u \text{ and } v \text{ realisations of } H_1. \end{cases} \quad (118)$$

Therefore the variables  $a = \lambda_1 \sum_{k=1}^N |u_k|^2$  and  $b = \lambda_2 \sum_{k=1}^N |v_k|^2$  that form the decision statistic (116) are mutually dependent Chi square random variables with  $2N$  degrees of freedom [47]. Using the joint density function of two independent Chi square random

variables derived by Lee [49] and computing the appropriate marginal distribution it can be shown that the PDF of  $z$  is, for  $z \leq 0$ ,

$$p(z) = \frac{(1 - \rho^2)^N e^{\left(\frac{z}{\alpha}\right)}}{\Gamma(N)(\alpha\beta)^N} \sum_{k=0}^{\infty} \left[ \mu_k \sum_{p=0}^{N+k-1} \left[ \binom{N+k-1}{p} \frac{\Gamma(2k+2N-p-1)}{\nu^{2k+2N-p-1}} (-z)^p \right] \right], \quad (119)$$

and for  $z > 0$ ,

$$p(z) = \frac{(1 - \rho^2)^N e^{\left(\frac{-z}{\beta}\right)}}{\Gamma(N)(\alpha\beta)^N} \sum_{k=0}^{\infty} \left[ \mu_k \sum_{p=0}^{N+k-1} \left[ \binom{N+k-1}{p} \frac{\Gamma(2k+2N-p-1)}{\nu^{2k+2N-p-1}} (-z)^p \right] \right], \quad (120)$$

where,

$$\alpha = \lambda_1 C_{11} (1 - \rho^2), \quad (121)$$

$$\beta = \lambda_2 C_{22} (1 - \rho^2), \quad (122)$$

$$\mu_k = \frac{1}{\Gamma(N+k)k!} \left( \frac{\rho^2}{\alpha\beta} \right)^k, \quad (123)$$

$$\nu = \frac{1}{\alpha} + \frac{1}{\beta}. \quad (124)$$

To obtain  $p(z; H_0)$  and  $p(z; H_1)$  the appropriate values for  $C_{11}$ ,  $C_{22}$  and  $\rho$ , defined in (117) and (118) are used.

To illustrate the detection performance of the log likelihood change statistic and compare with the sample coherence and sample mean backscatter power ratio a scene change scenario described by the following covariance matrices is considered,

Unchanged Hypothesis:

$$Q_0 = 1 \times 10^8 \begin{bmatrix} 2.2686 & 0.45 \cdot 2.0121 \cdot \exp(j\Phi) \\ 0.45 \cdot 2.0121 \cdot \exp(-j\Phi) & 1.7847 \end{bmatrix}, \quad (125)$$

Changed Hypothesis:

$$Q_1 = 1 \times 10^8 \begin{bmatrix} 2.2686 & 0 \\ 0 & 0.95070 \end{bmatrix}. \quad (126)$$

The values for the scene coherence in  $Q_0$  and the mean backscatter powers in the primary and repeat pass images in  $Q_0$  and  $Q_1$  are in fact experimental values obtained from a scene change experiment conducted with the DSTO Ingara SAR, see Section 6. Observe that under  $H_0$  there is a 1.04 dB reduction in the transduced mean backscatter power due to a radiometric miscalibration. Under  $H_1$  however, there is a 3.77 dB reduction in the mean backscatter power between the primary and repeat pass images, indicating that scene changes have caused a 2.73 dB reduction in the mean backscatter power of the scene. The coherence under  $H_0$  is 0.45 while the interferometric phase  $\Phi$  for the scene change scenario considered here has been set to zero. Figure 26 shows simulated and theoretical density functions for the decision statistic  $z$  under each hypothesis obtained using (119)

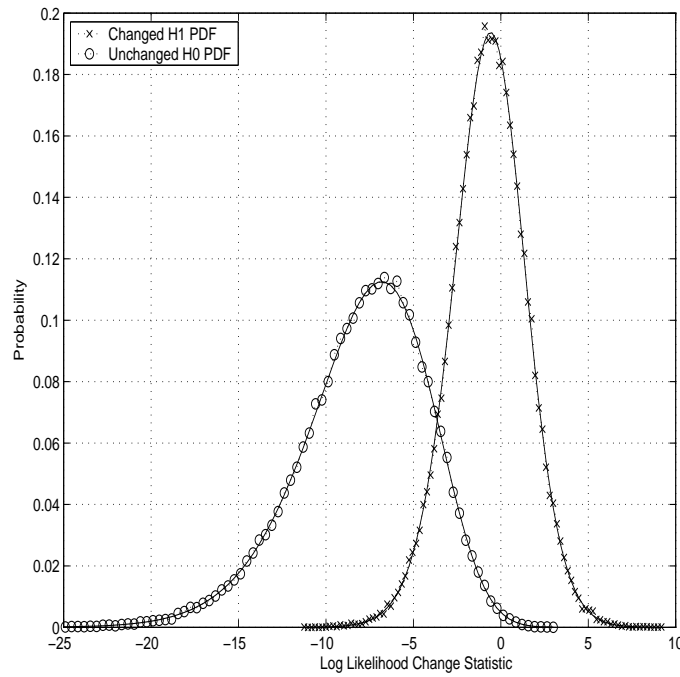


**Figure 26:** Simulated and theoretical density functions of the likelihood ratio change statistic for the unchanged  $H_0$  hypothesis and the changed  $H_1$  hypothesis. The mean backscatter ratio of the primary and repeat pass images is 1.04 dB under  $H_0$  and 3.77 dB under  $H_1$ ,  $N = 9$  and  $\gamma = 0.45$ .

and (120) with  $N = 9$ . For comparison, Figures 27 and 28 show the density functions of the sample coherence and mean backscatter power ratio change statistic for the same change scenario.

Change detections based on the log likelihood decision statistic, the sample coherence and mean backscatter ratio statistic may be obtained by evaluating the particular decision statistic over the scene, applying a threshold to the decision statistic map and assigning the values to either the changed or unchanged hypotheses. The ability of a change statistic to distinguish between the two hypotheses is determined by the degree of overlap of the density functions of the decision statistic under each hypothesis which, in turn, is predominantly dependent on the mean and “spread” of the density functions under each hypothesis. An examination of Figures 27 and 28 shows that while the mean values of the PDFs under the changed and unchanged hypotheses appear reasonably well separated, the spreads of the PDFs are large hence there is considerable overlap of the density functions. These change statistics will therefore suffer from significant false alarms and missed detections. The PDFs for the log likelihood change statistic under the changed and unchanged hypotheses shown in Figure 26 however have a much “narrower” spread and exhibit less overlap. The log likelihood statistic thus provides better discrimination between the two hypotheses. The detection performance improvement in terms of the probability of detection as a function of the probability of false alarm for a given decision threshold will be quantified in Section 5.2.

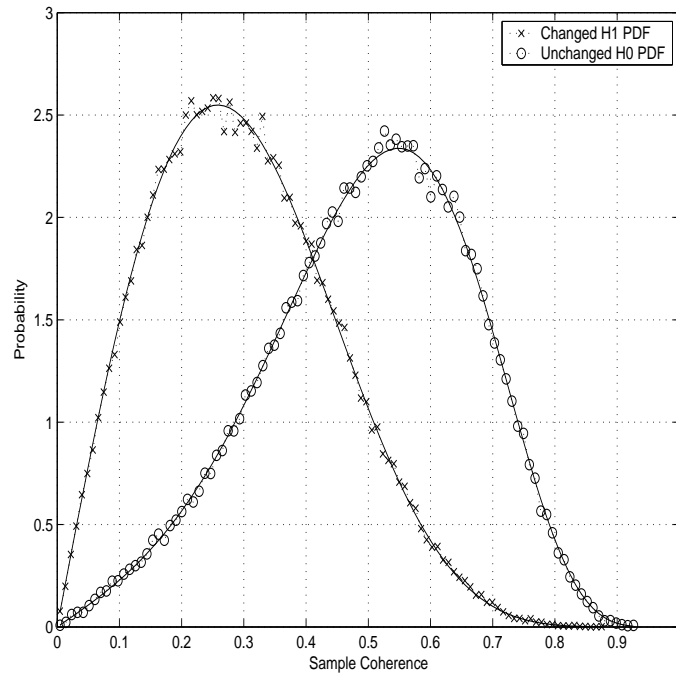


**Figure 27:** Simulated and theoretical density functions of the sample coherence for the unchanged  $H_0$  hypothesis and the changed  $H_1$  hypothesis. Under  $H_0$  the true underlying coherence is  $\gamma = 0.45$  while under  $H_1$   $\gamma = 0$  and  $N = 9$ .

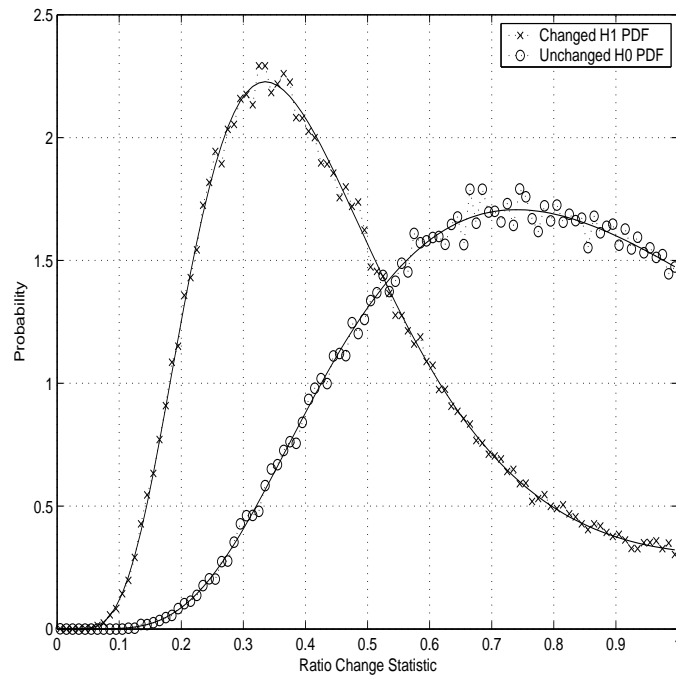


**Figure 28:** Simulated and theoretical density functions of the ratio statistic  $r$  for the unchanged  $H_0$  hypothesis and the changed  $H_1$  hypothesis. The mean backscatter ratio of the primary and repeat pass images is 1.04 dB under  $H_0$  and 3.77 dB under  $H_1$  and  $N = 9$ .

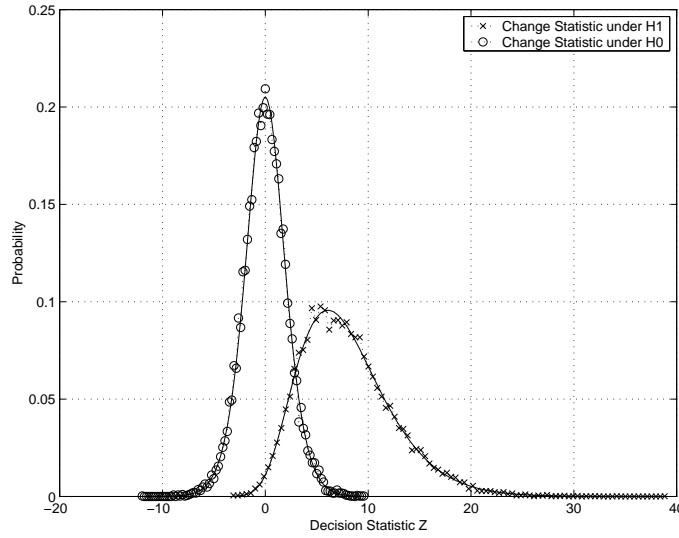


**Figure 29:** Density functions for the decision statistic under  $H_0$  and  $H_1$  for the case of equal backscatter powers  $\sigma_f^2 = \sigma_g^2$  with a partial coherence under  $H_0$  of  $\gamma = 0.45$  and  $N = 9$ .

### 5.1.1 Special Case of Equal Mean Backscatter Power

Scene disturbances arising from subtle man-made changes eg: disturbances due to the passage of vehicles through a scene, are commonly characterised by an absence of any measurable change in the mean backscatter power coupled with a complete loss in scene coherence. In such cases, for calibrated image pairs  $\sigma_f^2 = \sigma_{g0}^2 = \sigma_{g1}^2$  and a simpler closed form solution for the density function of the clairvoyant decision statistic may be derived. For  $z \leq 0$ ,

$$p(z) = \frac{\exp\left(\frac{z}{\lambda_1 C_{11}}\right)}{\Gamma^2(N)(\lambda_1 C_{11} \lambda_2 C_{22})^N} \sum_{p=0}^{N-1} \left[ \binom{N-1}{p} \frac{\Gamma(2N-p-1)}{\nu^{2N-p-1}} (-z)^p \right], \quad (127)$$

and for  $z > 0$ ,

$$p(z) = \frac{\exp\left(\frac{-z}{\lambda_2 C_{22}}\right)}{\Gamma^2(N)(\lambda_1 C_{11} \lambda_2 C_{22})^N} \sum_{p=0}^{N-1} \left[ \binom{N-1}{p} z^p \frac{\Gamma(2N-p-1)}{\nu^{2N-p-1}} \right]. \quad (128)$$

Note that these equations are general expression of the density function of  $z$ . To obtain  $p(z; H_0)$  and  $p(z; H_1)$  the appropriate values for  $C_{11}$  and  $C_{22}$ , defined in (117) are used. Figure 29 shows the density function of the decision statistic  $z$  for both  $H_0$  and  $H_1$  obtained by direct computation of (127) and (128) and also obtained via simulation for a coherence under  $H_0$  of  $\gamma = 0.45$ . Comparison of Figure 29 with the PDF of the sample coherence change statistic under the same change scenario in Figure 27 shows that the log likelihood change statistic provides better discrimination between the  $H_0$  and  $H_1$  hypotheses.

## 5.2 Detection Performance of the Clairvoyant Detector

Expressions for the probability of detection and false alarm for the clairvoyant log likelihood detector, as a function of the decision threshold  $T$ , may be derived using the probability density functions  $p(z; H_0)$  and  $p(z; H_1)$  given in the previous section by evaluating the integrals,

$$P_{fa} = \int_T^\infty p(z; H_0) dz, \quad (129)$$

$$P_d = \int_T^\infty p(z; H_1) dz. \quad (130)$$

Using (119) and (120) the  $P_d$  and  $P_{fa}$  both take the following general form for  $T > 0$ ,

$$\begin{aligned} P &= \frac{(1 - \rho^2)^N}{\Gamma(N)(\alpha\beta)^N} \sum_{k=0}^{\infty} \left[ \mu_k \sum_{p=0}^{N+k-1} \left[ \binom{N+k-1}{p} \frac{\Gamma(2N+2k-p-1)}{\nu^{2k+2N-p-1}} \int_T^\infty e^{(-\frac{z}{\beta})} (z)^p dz \right] \right], \\ &= \frac{(1 - \rho^2)^N}{\Gamma(N)(\alpha\beta)^N} \sum_{k=0}^{\infty} \left[ \mu_k \sum_{p=0}^{N+k-1} \left[ \binom{N+k-1}{p} \beta^{p+1} \frac{\Gamma(2N+2k-p-1)}{\nu^{2k+2N-p-1}} \right. \right. \\ &\quad \left. \left. \Gamma_{inc} \left( p+1, \frac{T}{\beta} \right) \right] \right], \end{aligned} \quad (131)$$

where  $\Gamma_{inc}$  is the complementary incomplete gamma function given by,

$$\Gamma_{inc}(a, t) = \int_t^\infty \exp(-x) x^{a-1} dx. \quad (132)$$

For  $T \leq 0$  the integrals giving the probability of false alarm (129) and probability of detection (130) must be partitioned into an integral from  $T$  to 0 where  $p(z)$  is given by (119) plus an integral from 0 to  $\infty$  where  $p(z)$  is given by (120). The probability of detection and probability of false alarm thus both take the following form for  $T < 0$ ,

$$\begin{aligned} P &= \frac{(1 - \rho^2)^N}{\Gamma(N)(\alpha\beta)^N} \sum_{k=0}^{\infty} \left[ \mu_k \sum_{p=0}^{N+k-1} \left[ \binom{N+k-1}{p} \frac{\Gamma(2N+2k-p-1)}{\nu^{2k+2N-p-1}} \right. \right. \\ &\quad \left. \left. \left[ \int_0^\infty e^{(-\frac{z}{\beta})} (z)^p dz + \int_T^0 e^{(\frac{z}{\alpha})} (-z)^p dz \right] \right] \right], \\ &= \frac{(1 - \rho^2)^N}{\Gamma(N)(\alpha\beta)^N} \sum_{k=0}^{\infty} \left[ \mu_k \sum_{p=0}^{N+k-1} \left[ \binom{N+k-1}{p} \frac{\Gamma(2N+2k-p-1)}{\nu^{2k+2N-p-1}} \left[ \beta^{p+1} \Gamma(p+1) \right. \right. \right. \\ &\quad \left. \left. \left. + \alpha^{p+1} \left( \Gamma(p+1) - \Gamma_{inc} \left( p+1, \frac{-T}{\alpha} \right) \right) \right] \right] \right], \end{aligned} \quad (133)$$

where the following relation has been used [42],

$$\int_0^t \exp(-x) x^{(a-1)} dx = \Gamma(a) - \Gamma_{inc}(a, t). \quad (134)$$

The values for  $C_{11}$ ,  $C_{22}$  and  $\rho$  used in the computation of  $\mu_k$ ,  $\alpha$  and  $\beta$  in (131) and (133) are defined in (118) for each hypotheses.

In the case where the primary and repeat pass images have equal mean backscatter parameters under both  $H_0$  and  $H_1$  the following simpler general forms for the probability of detection or probability of false alarm are obtained, for  $T > 0$ ,

$$\begin{aligned}
P &= \frac{1}{\Gamma^2(N)(\lambda_1 C_{11} \lambda_2 C_{22})^N} \sum_{p=0}^{N-1} \left[ \binom{N-1}{p} \frac{\Gamma(2N-p-1)}{\nu^{2N-p-1}} \int_T^\infty \exp\left(\frac{-z}{\lambda_2 C_{22}}\right) z^p dz \right], \\
&= \frac{1}{\Gamma^2(N)(\lambda_1 C_{11} \lambda_2 C_{22})^N} \sum_{p=0}^{N-1} \left[ \binom{N-1}{p} \frac{\Gamma(2N-p-1)}{\nu^{2N-p-1}} \right. \\
&\quad \left. (\lambda_2 C_{22})^{p+1} \Gamma_{inc}\left(p+1, \frac{T}{\lambda_2 C_{22}}\right) \right], \quad (135)
\end{aligned}$$

and for  $T \leq 0$ ,

$$\begin{aligned}
P &= \frac{1}{\Gamma^2(N)(\lambda_1 C_{11} \lambda_2 C_{22})^N} \sum_{p=0}^{N-1} \left[ \binom{N-1}{p} \frac{\Gamma(2N-p-1)}{\nu^{2N-p-1}} \right. \\
&\quad \left. \left[ \int_T^0 \exp\left(\frac{-z}{\lambda_1 C_{11}}\right) (-z)^p dz + \int_0^\infty \exp\left(\frac{-z}{\lambda_2 C_{22}}\right) (z)^p dz \right] \right], \\
&= \frac{1}{\Gamma^2(N)(\lambda_1 C_{11} \lambda_2 C_{22})^N} \sum_{p=0}^{N-1} \left[ \binom{N-1}{p} \frac{\Gamma(2N-p-1)}{\nu^{2N-p-1}} \right. \\
&\quad \left. \left[ (\lambda_2 C_{22})^{p+1} \Gamma(p+1) + (\lambda_1 C_{11})^{p+1} \Gamma_{inc}\left(p+1, \frac{-T}{\lambda_1 C_{11}}\right) \right] \right]. \quad (136)
\end{aligned}$$

Figures 30 and 31 give the theoretical and simulated ROC curves of the clairvoyant decision statistic for the equal backscatter power case for various values of coherence  $\gamma$  and various values of  $N$  respectively. From Figure 30 the sensitivity of the clairvoyant decision statistic to the scene coherence can be assessed. For  $N = 9$  and a probability of detection of 0.7 the probability of false alarm for  $\gamma = 0.45$  is approximately 0.05 while at  $\gamma = 0.6$  the probability of false alarm is reduced by over an order of magnitude to 0.002. Increasing the coherence to  $\gamma = 0.75$  yields false alarm rates of well below  $10^{-4}$ . From Figure 31 it can be seen that increasing the number of pixels  $N$  in the decision statistic calculation can provide significant improvements in the detection performance albeit at the expense of resolution in the change detection map. At a probability of detection of 0.7 and  $N = 4$  the probability of false alarm is approximately 0.06 while for  $N = 9$  this is reduced by over an order of magnitude to 0.002.

As Figures 30 and 31 describe the ROC performance of the log likelihood change statistic where discrimination between the hypotheses is based solely on the scene coherence under  $H_0$ , these ROC curves may be directly compared with those of the sample coherence change statistic examined in Section 4.3. A comparison of Figures 30 and 31 with the corresponding ROC curves of the sample coherence given in Figures 24 and 25 indicates that the log likelihood change statistic offers a significantly improved detection performance with false alarm rates typically an order of magnitude better than those of the sample coherence. For a probability of detection of 0.7 at a coherence of  $\gamma = 0.45$  the probability of false alarm for the sample coherence is 0.25 while for the log likelihood statistic it is 0.05. For a coherence of 0.6 the improvement is more pronounced with the probability of



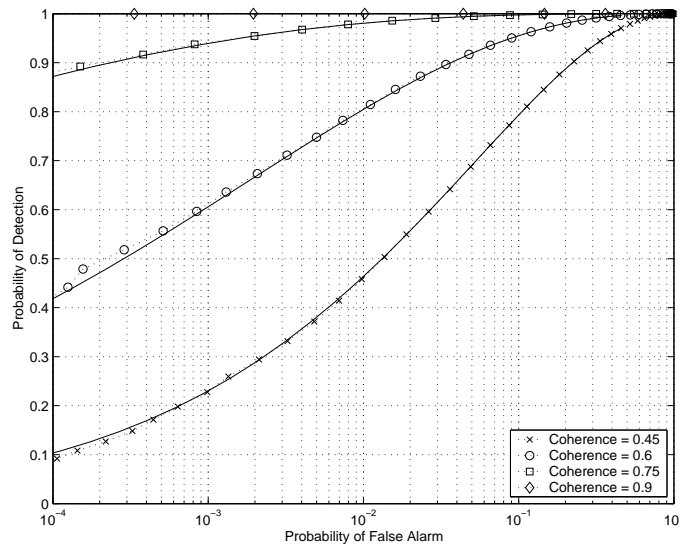


**Figure 30:** Theoretical and simulated ROC curves for equal channel powers and coherence values of 0.45, 0.6, 0.75 and 0.9 with  $N = 9$ .

false alarm for the sample coherence being 0.06 compared to 0.003 for the log likelihood statistic.

Figure 32 shows the ROC curves for the clairvoyant log likelihood decision statistic, the sample coherence and the mean backscatter ratio statistic for the experimental scene change scenario, i.e., a mean backscatter change of 1.04 dB under  $H_0$  and 3.77 dB under  $H_1$ , a coherence  $\gamma = 0.45$  for  $H_0$  and  $N = 9$ . It can be seen from Figure 32 that the sample coherence and mean backscatter ratio statistics have similar detection performance. The clairvoyant log likelihood statistic however provides a significantly better detection performance. For a probability of detection of 0.7 the probability of false alarm in the log likelihood detector is 0.03 which is almost an order of magnitude better than that of either the sample coherence or the mean backscatter ratio which is approximately 0.25.

### 5.3 Generalised Log Likelihood Change Statistic

The ROC curves considered here describe the performance of a clairvoyant detector in which perfect knowledge of the unknown covariance matrices  $Q_0$  and  $Q_1$  has been assumed. While such a detector is unrealisable, it gives an upper bound on the detection performance of any practical detector implementation.

A Generalised Likelihood Ratio Test (GLRT) is an easily implemented practical detector in which the unknown scene parameters,  $Q_0$  and  $Q_1$  in (113), are replaced with their Maximum Likelihood Estimates (MLE) obtained from the observed data. The MLE of the covariance matrices  $Q_0$  and  $Q_1$  are given by the corresponding sample covariance matrices [50], i.e.,

$$\hat{Q}_0 = \frac{1}{M_0} \sum_{k=1}^{M_0} \underline{X}_{k_0} \underline{X}_{k_0}^H \text{ and } \hat{Q}_1 = \frac{1}{M_1} \sum_{k=1}^{M_1} \underline{X}_{k_1} \underline{X}_{k_1}^H, \quad (137)$$

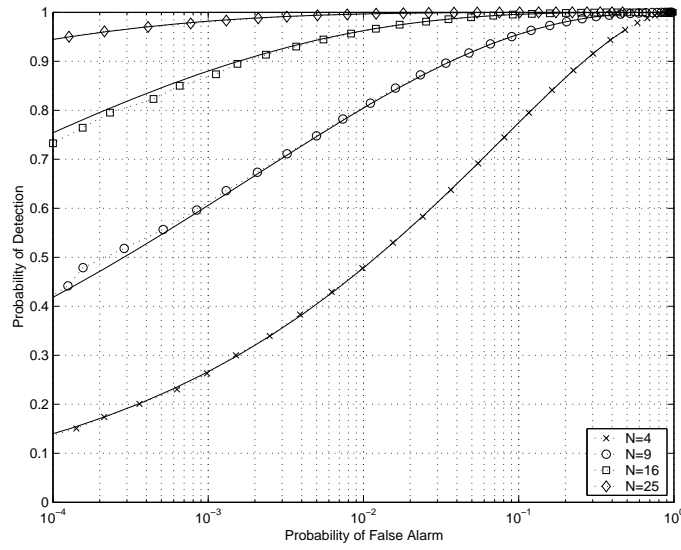


**Figure 31:** Theoretical and simulated ROC curves for equal channel powers and  $N = 4, 9, 16, 25$  with a coherence of 0.6.

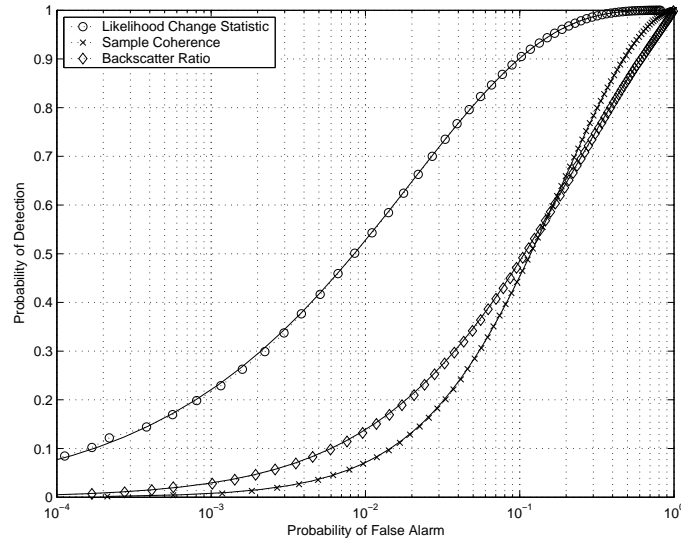


**Figure 32:** Theoretical and simulated ROC curves for a scene change scenario where the mean backscatter ratio of the primary and repeat pass images is 1.04 dB under  $H_0$  and 3.77 under  $H_1$ ,  $N = 9$  and  $\gamma = 0.45$ .

where the pixel pairs  $\underline{X}_{k_0} = [f_{k_0}, g_{k_0}]^T, k = 1 \cdots M_0$  and  $\underline{X}_{k_1} = [f_{k_1}, g_{k_1}]^T, k = 1 \cdots M_1$  are realisations of the  $H_0$  and  $H_1$  hypotheses respectively. The quality of the sample covariance estimates are dependent on obtaining a sufficient number of independent image pixels,  $M_0$  and  $M_1$ , that are characteristic of the  $H_0$  and  $H_1$  hypotheses associated with the local  $N$  pixel area under test.

In the change detection scenarios considered in this paper, such as the detection of vehicle tracks across an open field, the scene disturbances are typically localised and isolated to specific regions in the scene. Furthermore the scene changes are also typically on a significantly smaller spatial scale than variations in the underlying statistical properties of the scene's complex radar backscatter. Under these conditions large homogeneous areas for estimating the unknown covariance matrices may be readily identified. Indeed using a fine resolution sensor and processing a wide-angle collection aperture, estimation windows consisting of a statistically significant number of samples, suitable for estimating the unknown covariance matrices, may be readily obtained. Furthermore, prior knowledge regarding the nature of the scene disturbances and the backscatter characteristics of the region under test, eg: assuming  $\sigma_{g0}^2 = \sigma_{g1}^2$ , may be used to refine the sample covariance estimates.

A mathematical derivation of the detection performance of the GRLT has not been found. However, Monte-Carlo simulation techniques may be used to evaluate the average change detection performance that may be expected for sample sizes  $M_0$  and  $M_1$  used in the estimation of  $Q_0$  and  $Q_1$  respectively. Figure 33 shows the average ROC curves of the log likelihood change statistic obtained via Monte-Carlo simulation for sample window sizes of  $M_0 = M_1 = 25, 64, 121$  and  $400$  and  $N = 7$ . The change detection scenario considered in the simulation has  $\sigma_f^2 = \sigma_{g0}^2 = \sigma_{g1}^2$  and  $\gamma_0 = 0.62$ . From Figure 33 it is evident that to achieve an average detection performance comparable to that of the clairvoyant detector window sizes of the order of several hundred pixels are required.

## 6 Application to Experimental Data

Repeat pass collections have been acquired with the DSTO Ingara X-band SAR over two different scenes in which various ground truthed scene changes have occurred in the interval between collections. The first scene, shown in Figure 34, consists of an open, lightly grassed field with a building located at the bottom of the image. A sealed road runs along the right hand side of the image and an unsealed road runs along the top of the scene. An open drainage trench is visible in the upper left hand corner of the image. In this change detection experiment a 20 m by 20 m scene change was performed using a rotary hoe and a long strip was modified using a lawn mower, as indicated in Figure 34. The repeat pass collection was acquired at an incidence angle of 60 degrees with a repeat pass interval of 24 hours.

The other repeat pass acquisition was also carried out in an open lightly grassed field. The field, shown in the SAR intensity image of Figure 35, has drainage trenches approximately 1.5 m wide and 0.8 m deep that are visible as lines of low backscatter running through the field. The field is bordered by a line of trees on the right hand side and by buildings and trees on the left hand side. Azimuthal smear evident in the imagery

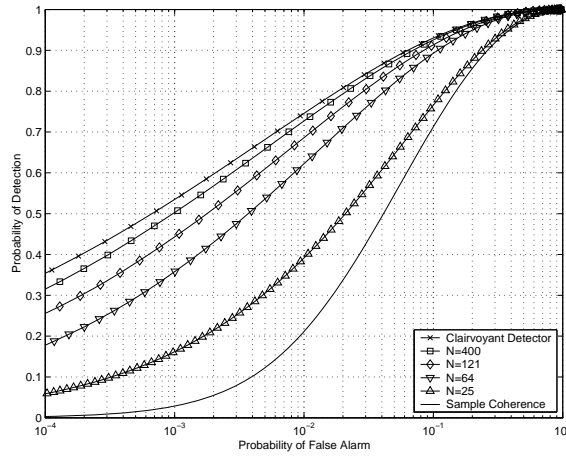


**Figure 33:** Average ROC curves for the log likelihood change statistic obtained using Monte-Carlo simulation techniques. Sample window sizes of  $M_0 = M_1 = 25, 64, 121$  and 400 have been used to estimate  $Q_0$  and  $Q_1$  and a window size of  $N = 7$  has been used to compute the log likelihood statistic. The unchanged scene coherence is  $\gamma = 0.62$  and it has been assumed that  $\sigma_f^2 = \sigma_{g_0}^2 = \sigma_{g_1}^2$ .

of the trees is due to the effects of wind moving the leaves and branches during the coherent processing interval of approximately 20 sec. The repeat pass collection was acquired at an incidence angle of 75 degrees with a repeat pass interval of 2 hours. The scene changes, shown in Figure 35, consist of a series of strips of varying lengths and widths carried out using a rotary hoe and a lawn mower.

At the time of the repeat pass interferometry experiments detailed here the Ingara airborne SAR was installed on a Beech 350 Super KingAir aircraft. (It has since been upgraded to provide a fully polarimetric X-band capability and has been rehosted onto a Beech 1900C [51].) The operating parameters for the radar, as configured for the repeat pass interferometry experiments, are detailed in Table 1.

**Table 1:** System parameters for the Ingara airborne SAR as configured for the repeat pass interferometry experiments.

Parameter	Value
Transmit waveform	LFM chirp, 400 MHz bandwidth
Transmitter power	8 kW
Polarization	HH
Radar centre frequency	9.35 GHz
Range resolution	0.5 m slant range resolution in spotlight mode
Incidence angle range	45 to 89 degrees

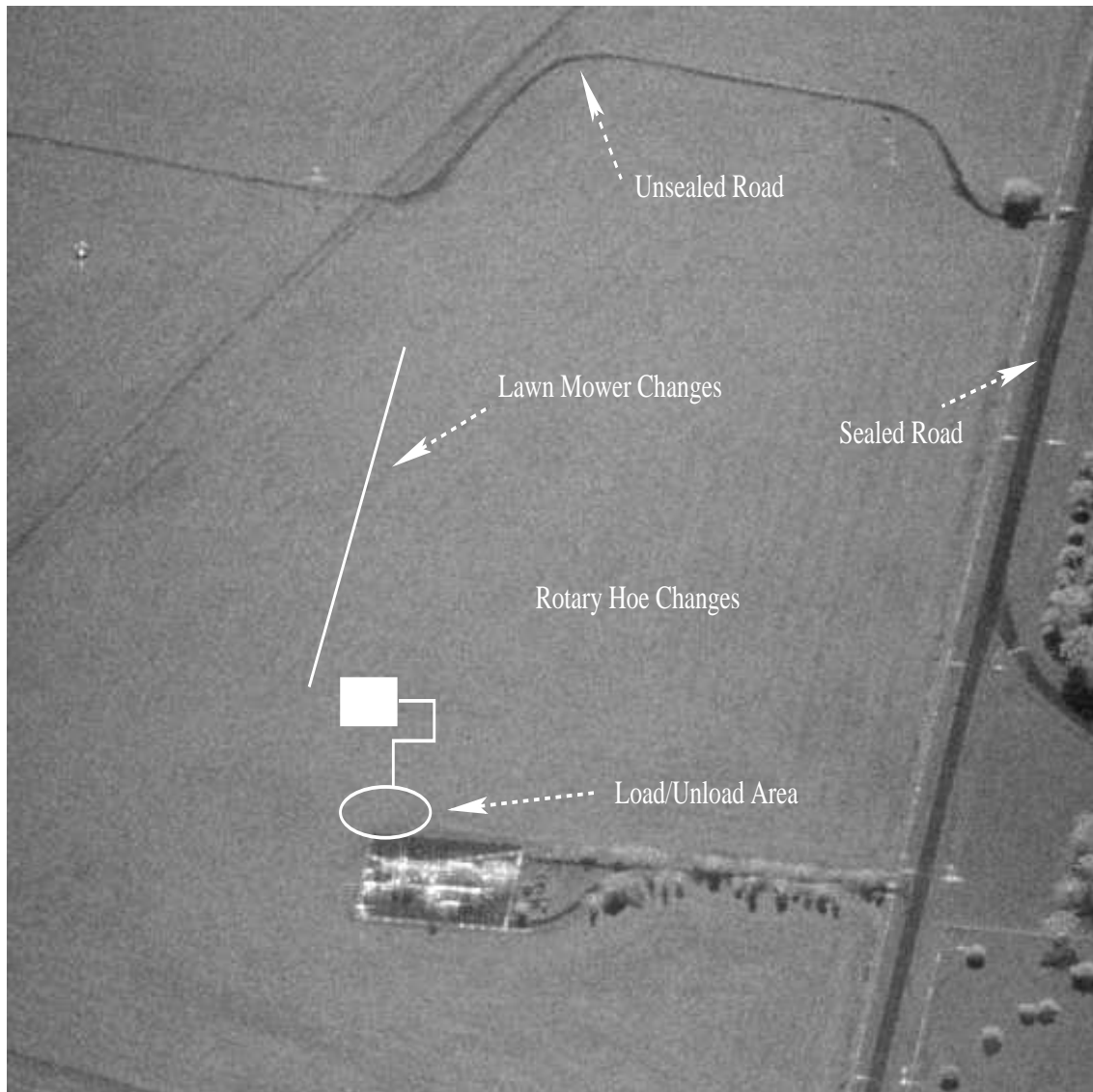


**Figure 34:** Intensity SAR image of the scene used for repeat pass interferometry experiments. Superimposed on the image is a schematic showing the scene changes carried out with the rotary hoe and lawn mower.

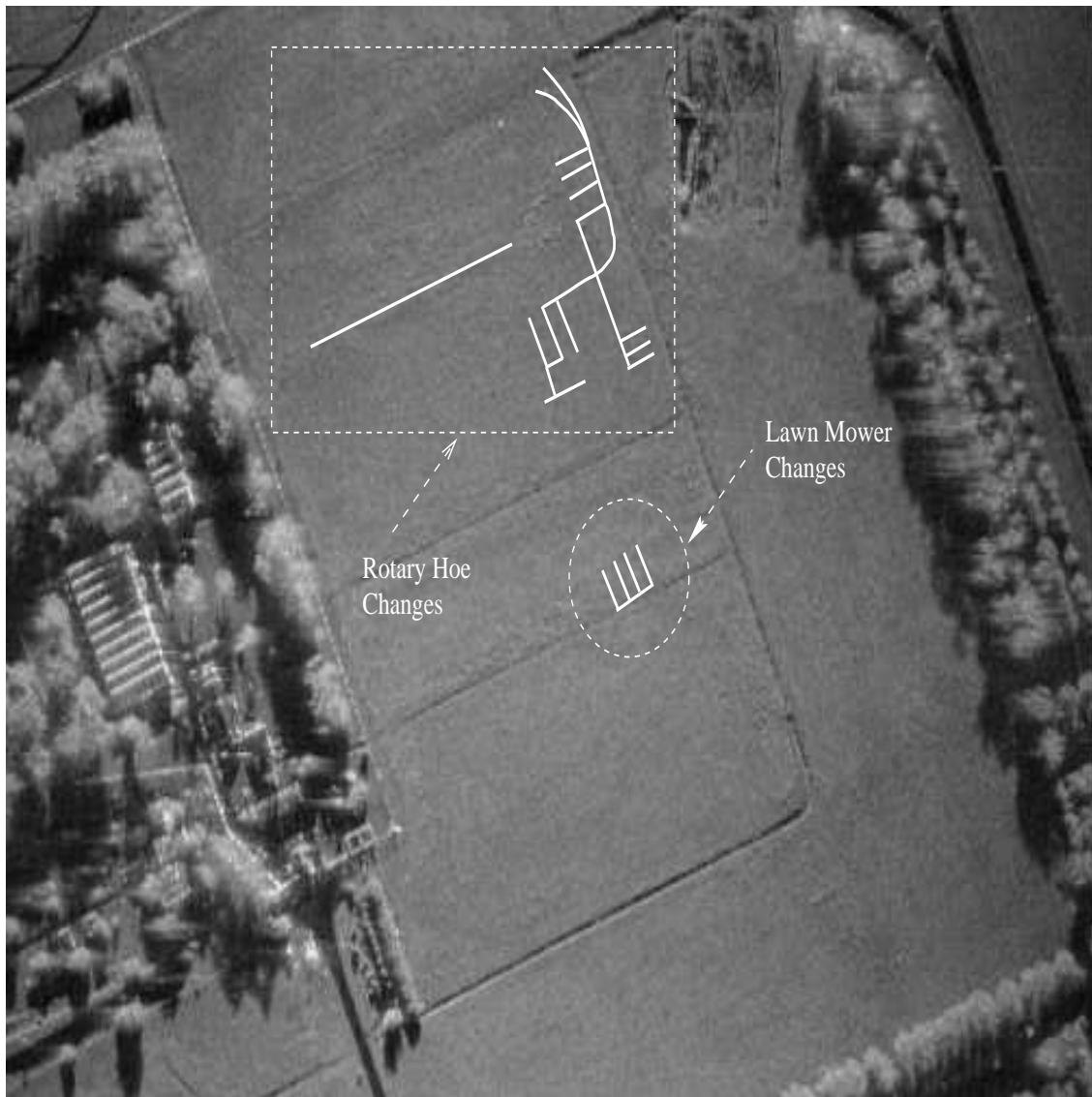


**Figure 35:** Intensity SAR image of the scene used for repeat pass interferometry experiments. Superimposed on the image is a schematic showing the scene changes carried out with the rotary hoe and lawn mower.

## 6.1 Repeat Pass Image Pair 1

Figures 36 and 37 show the primary and repeat pass intensity images for the first interferometric pair having the changes illustrated in Figure 34. The 3 dB resolution of the Single Look Complex (SLC) image pair generated by the SAR processor is 0.61 m range by 0.15 m azimuth with a Hamming window applied and the pixel spacing is 0.3 m by 0.1 m. The slant range offset and depression angle differences at the aperture midpoint are 70.94 m and 0.182 degrees respectively. The 20 m by 20 m scene change carried out using the rotary hoe is clearly observed in Figure 37 as an area of reduced mean backscatter power and is also readily seen in the mean backscatter power ratio change map in Figure 38. The mean backscatter power of the primary and repeat pass imagery has been estimated by firstly upsampling the SLC imagery generated by the SAR processor by a factor of 2 in range and azimuth (as described in Section 3.5.5) followed by application of a 6 (range) by 14 (azimuth) pixel sliding spatial estimation window. A final decimation stage by factors of 3 pixels in range and 7 pixels in azimuth has been applied giving a pixel spacing of 0.45 by 0.34 m for the resulting mean backscatter power estimates. The point spread function of the mean backscatter power imagery is determined by the autocorrelation of the Hamming window used by the SAR processor as described in Section 3.5.5. The 3 dB resolution of the mean backscatter power imagery has been evaluated numerically to be 0.64 m by 0.22 m.

Figures 39 and 40 show the coherence and interferometric phase images given by the amplitude and phase of the complex sample cross correlation coefficient. The complex sample cross correlation coefficient has been estimated using the same 3 by 7 pixel window as that used in computing the mean backscatter power. The coherence and interferometric phase images thus have the same 3 dB resolution and pixel spacing as the mean backscatter power. The modified ground truth area is clearly visible as an area of low coherence in Figure 39 and is also discernible in the interferometric phase map as an area of rapid, random phase fluctuations. Other areas of low coherence visible in the sample coherence map are evident in the region between the building and the area modified with the rotary hoe and also in the upper left corner below the unsealed road. From ground truth observations these regions correspond to areas of taller, denser, broad leaf grass cover, see Figure 41, that are more susceptible to temporal decorrelation over the 24 hr revisit period. The remaining areas of the scene have also been subject to temporal decorrelation during the revisit period. These areas are more sparsely covered (see Figure 41) and thus exhibit a modest degree of coherence estimated to be 0.45 (see Section 6.1.1). It is interesting to note that while the denser vegetation regions are clearly observed in the sample coherence map the same areas are not readily discerned in the intensity imagery of Figure 36 indicating that the coherence may be used as a statistic for scene classification applications.

### 6.1.1 Joint Statistics of the Repeat Pass Image Pair

For the purposes of applying the change detection statistics and measuring their detection performance a small image subchip, as indicated in Figure 36, has been extracted from both the primary and repeat pass SLC images. This image subchip contains the area modified by the rotary hoe while the remaining unmodified areas are essentially homoge-



**Figure 36:** Intensity SAR image generated from the primary pass collection processed to a 3 dB resolution of 0.61 m (range) by 0.15 m (azimuth) with a Hamming window applied. Also shown is the image subchip selected for further processing and change detection analysis.





**Figure 37:** Intensity SAR image generated from the repeat pass collection processed to a 3 dB resolution of 0.61 m (range) by 0.15 m (azimuth) with a Hamming window applied. Also shown is the image subchip selected for further processing and change detection analysis.

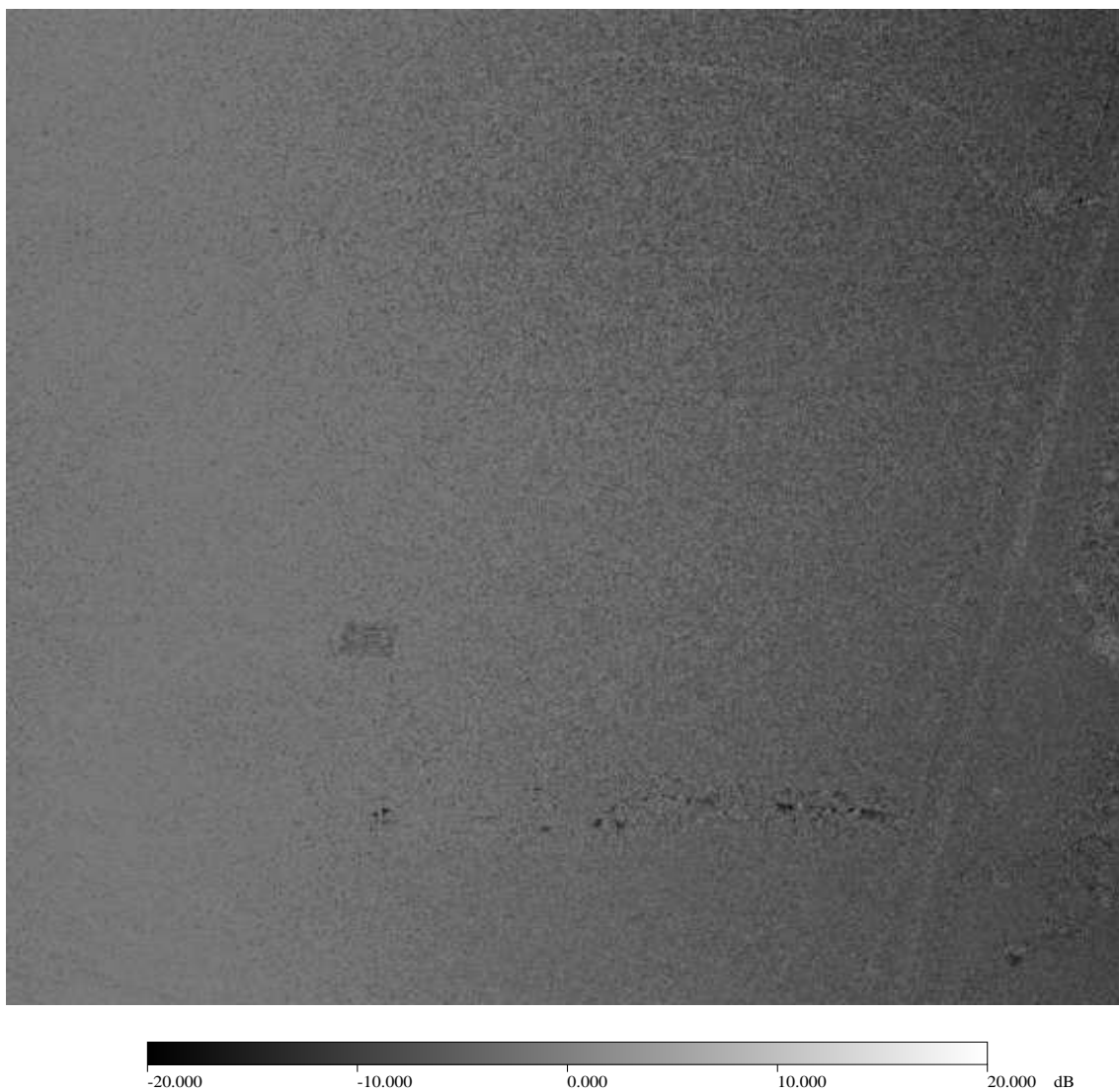


**Figure 38:** Mean backscatter power ratio change statistic evaluated over the primary and repeat pass image pair.

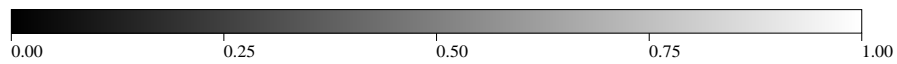


**Figure 39:** Sample coherence evaluated over the repeat pass image pair using a 3 by 7 pixel spatial estimation window.

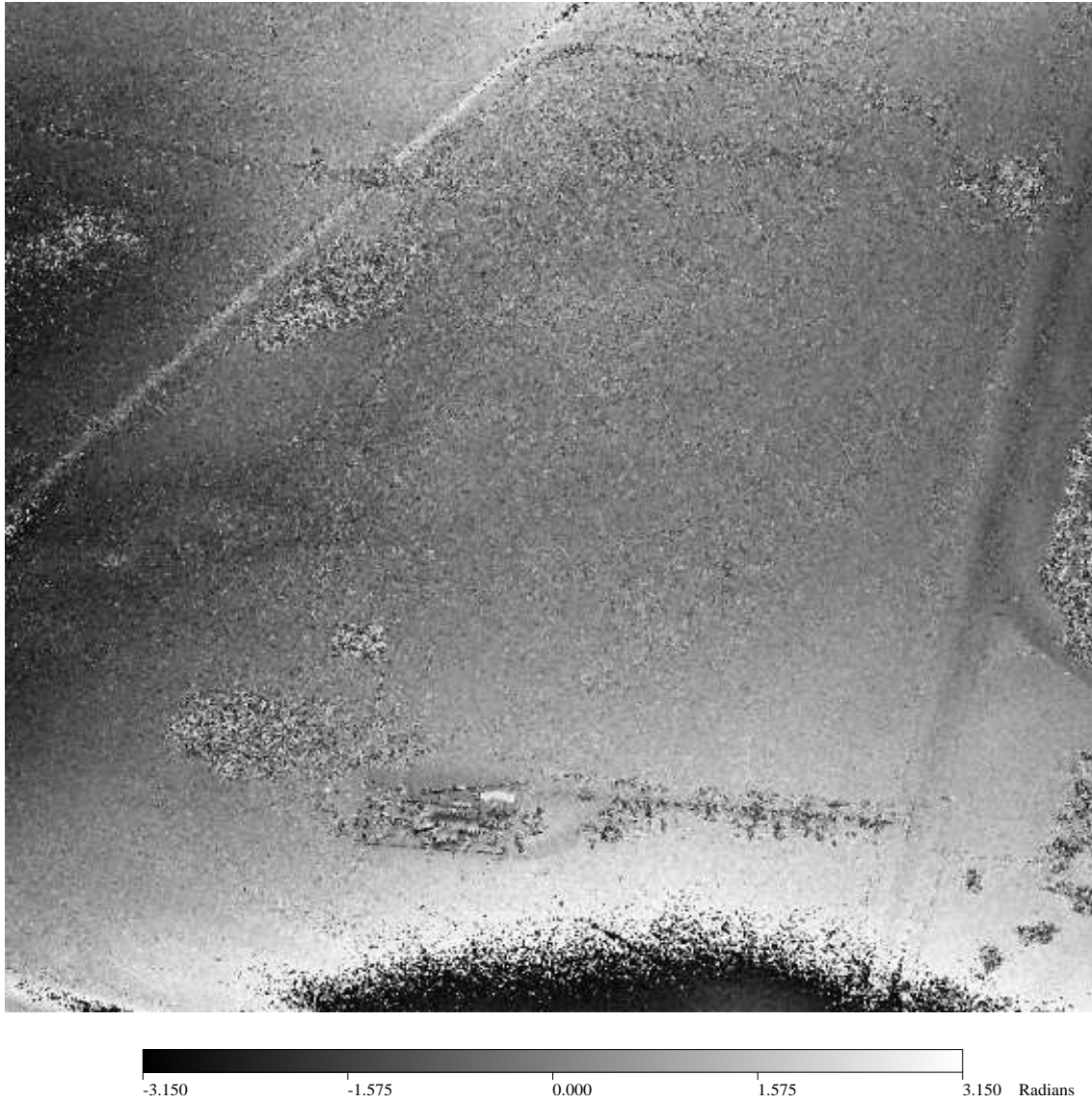


**Figure 40:** Sample interferometric phase evaluated over the repeat pass image pair using a 3 by 7 pixel spatial estimation window.

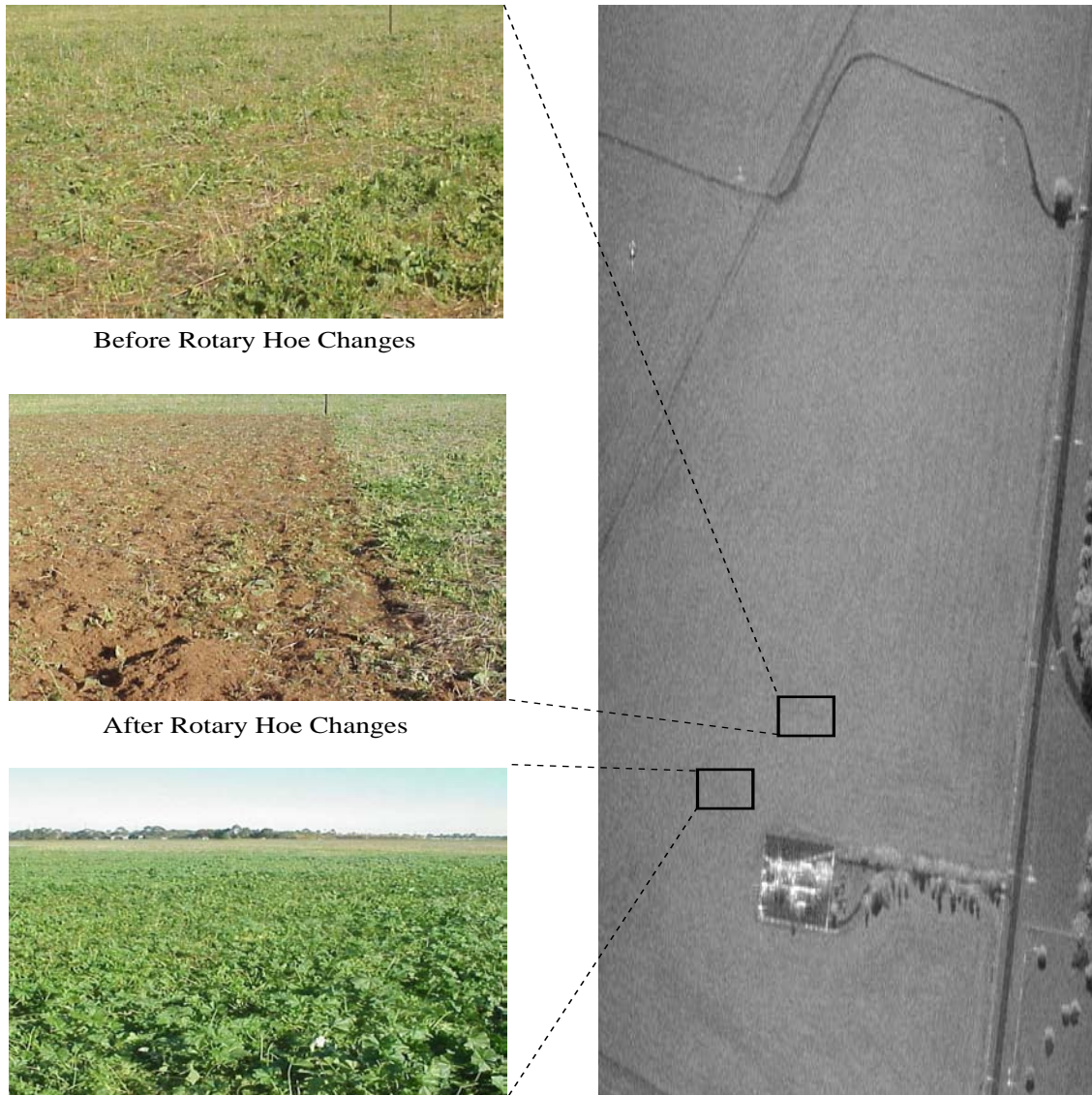


*Figure 41: Ground truth observations of the scene disturbances.*



neous in terms of their vegetation cover. In order to estimate the underlying statistical parameters of the image pair using spatial windows the extracted image subchips have been subsampled by a factor of two in range and azimuth to reduce the correlation between neighbouring pixels. While this introduces a modest degree of spatial aliasing in the imagery the sample estimates of the image statistics may then be compared to the theoretical distributions in which averaging over independent pixels is assumed. In addition the probability density functions of the change statistics described in Sections 4 and 5 were derived under the assumption of independent pixels and thus validation of the theoretical results requires independent pixels. (In the literature the presence of correlated pixels is modelled by employing the notion of an Equivalent Number of Looks (ENL) [52]. However, while this appears to be consistent with experimental data a theoretical derivation of the PDFs for the case of correlated pixels has not been derived.) The subsampled image subchip is 230 by 100 pixels in size. Averaging the image pixel intensities over the entire  $N = 23,000$  pixel subsampled primary and repeat pass image subchips gives the following estimates for the mean backscatter powers,

$$\text{Primary Image: } \hat{\sigma}_f^2 = \frac{1}{N} \sum_{k=1}^N |f_k|^2 = 2.2686 \times 10^8, \quad (138)$$

$$\text{Repeat Image: } \hat{\sigma}_g^2 = \frac{1}{N} \sum_{k=1}^N |g_k|^2 = 1.5380 \times 10^8. \quad (139)$$

For images having Gaussian backscatter characteristics the pixel amplitude is Rayleigh distributed while the phase is randomly distributed [12]. Figure 42 shows the amplitude and phase histograms of each image subchip using all the pixels in each subchip as well as the theoretical Rayleigh amplitude and uniform phase density functions. (In specifying the Rayleigh distribution the estimates of the mean backscatter power  $\hat{\sigma}_f^2$  and  $\hat{\sigma}_g^2$  have been used.) Also shown in the plots of Figure 42 is the likely range in variation of the histogram estimates of the PDF that are to be expected assuming the Rayleigh amplitude and uniform phase PDFs are accurate models. (The range of expected values shown are the  $\pm$  three standard deviations about the mean expected at each histogram sample bin, see Appendix A.) The good agreement between the amplitude and phase histograms and the theoretical density functions indicates the image subchips have a strongly Gaussian behaviour. The mean backscatter power estimated over the 20 m x 20 m modified area of the scene is  $\hat{\sigma}_g^2 = 9.5070 \times 10^7$  while the mean backscatter power for the area outside the modified region is  $1.7847 \times 10^8$ . The scene modifications have thus caused a reduction in the mean backscatter power of 2.73 dB.

The complex sample cross correlation coefficient has been computed across the subsampled subchip pair by averaging over a 3 by 3 pixel spatial estimation window. Figure 43 shows a histogram of the magnitude of the cross correlation coefficient, i.e., the coherence, obtained using sample estimates from the entire image subchip pair. The histogram consists of a mixture of modified, low coherence areas and unmodified, partial coherence areas. Superimposed on the histogram of Figure 43 is the theoretical density of the sample coherence obtained using equation (101) where a true coherence of  $\gamma = 0.45$  and an ENL of 7 have been found to provide the best fit to the experimental histogram. (Also shown in Figure 43 is the likely range in variation (three standard deviations) of the histogram estimate of the PDF that is to be expected assuming the jointly Gaussian model is correct.)

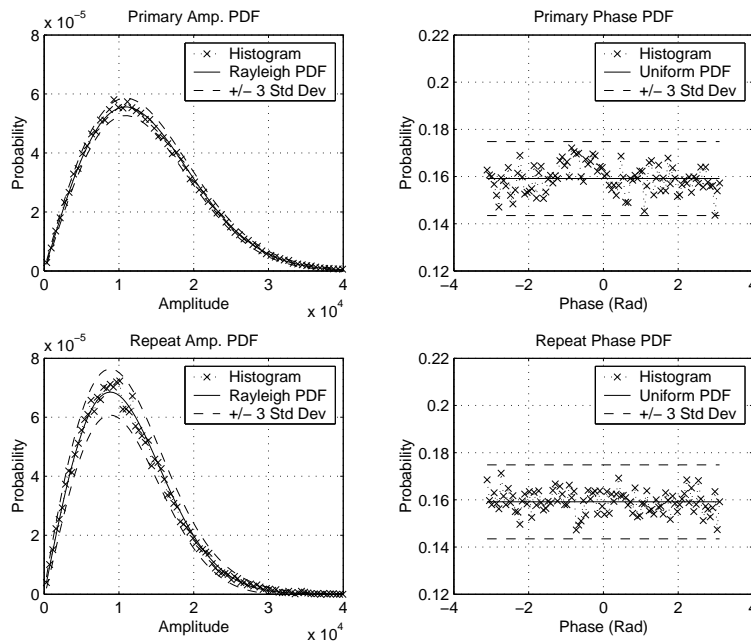


**Figure 42:** Amplitude and phase histograms for the primary and repeat pass image subchips. Superimposed on the histograms are the theoretical Rayleigh amplitude and uniform phase density functions that are associated with complex Gaussian scattering behaviour.

The histogram and theoretical density functions show reasonable agreement, and deviations between the plots, outside the anticipated histogram deviation from the theoretical PDF, may be attributed to the mixture of sample estimates obtained over both modified and unmodified regions in the image subchips used to produce the histogram. It has been found that the best theoretical fit for the observed sample coherence is obtained with an ENL of 7. This is less than the number of pixels in the spatial estimation window indicating that some residual correlation exists between neighbouring pixels in the subsampled imagery.

The interferometric phase of the repeat pass pair will vary across the scene depending on the terrain topography and the interferometric baseline. Accordingly the interferometric phase may be estimated from the phase of the complex sample cross correlation coefficient by averaging over sufficiently small regions for which the interferometric phase may be considered to be constant. For the repeat pass pair considered here it is found the image subchip may be partitioned into four equally sized non-overlapping quadrants over which the interferometric phase varies only slowly. Figure 44 shows histograms of the interferometric phase recovered from the complex sample correlation coefficient. Superimposed onto the histograms are theoretical density functions calculated using a coherence of  $\gamma = 0.45$ , ENL=7 and interferometric phase values of -0.25, 0.04, -0.02 and 0.25 radians for the four quadrants. Also shown in the plots of Figure 44 is the likely range in variation (three standard deviations) of the histogram estimate of the PDF that is to be expected assuming the jointly Gaussian model is correct. The histograms and theoretical density functions show reasonable agreement. Sources of deviation between the histograms and the theoretical density functions include variations in the underlying phase across the

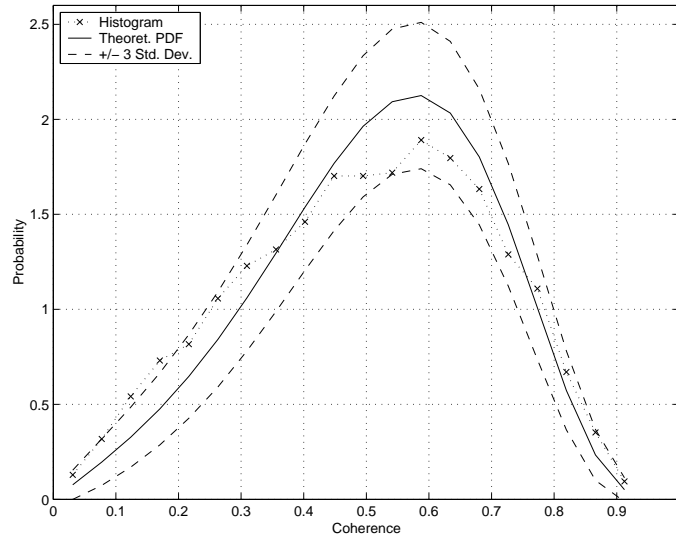


**Figure 43:** Histogram and theoretical density function of the sample coherence. The estimated true coherence and ENL used to calculate the theoretical fit are 0.45 and 7 respectively.

quadrants as well as variations in the underlying coherence across the quadrants which include both changed (low coherence) and unchanged (high coherence) regions.

### 6.1.2 Change Detection Performance

Using the values for the mean backscatter power, coherence and interferometric phase of the changed and unchanged pixels estimated in the previous section the repeat pass image subchips can be described by a jointly Gaussian random process with covariance matrix  $Q(x, y)$  given by,

$$Q_0(x, y) = 1 \times 10^8 \begin{bmatrix} 2.2686 & 0.45 \cdot 2.0121 \cdot \exp(j\Phi(x, y)) \\ 0.45 \cdot 2.0121 \cdot \exp(-j\Phi(x, y)) & 1.7847 \end{bmatrix} \quad (140)$$

for the unmodified pixels and

$$Q_1(x, y) = 1 \times 10^8 \begin{bmatrix} 2.2686 & 0 \\ 0 & 0.95070 \end{bmatrix}, \quad (141)$$

for the changed pixels, where  $\Phi(x, y)$  is the mean interferometric phase estimates identified in the previous section,

$$\Phi(x, y) = \begin{cases} -0.25 \text{ rad,} & (x, y) \text{ in Quadrant 1,} \\ +0.04 \text{ rad,} & (x, y) \text{ in Quadrant 2,} \\ -0.02 \text{ rad,} & (x, y) \text{ in Quadrant 3,} \\ +0.25 \text{ rad,} & (x, y) \text{ in Quadrant 4.} \end{cases} \quad (142)$$

For simplicity the interferometric phase will be modelled as being constant over each of the four quadrants considered in the previous section with a step change in phase across the quadrants.



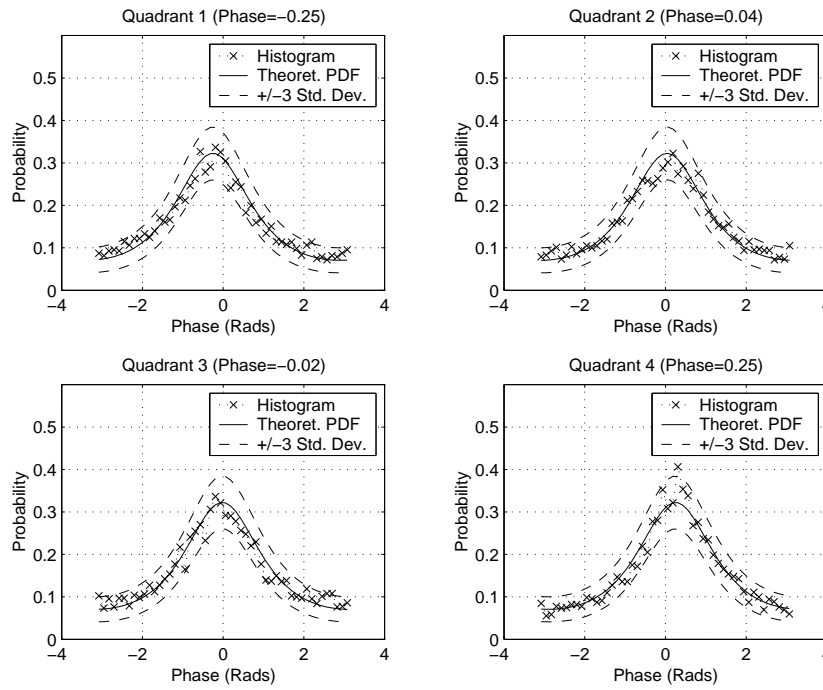


**Figure 44:** Histograms and theoretical density functions of the sample interferometric phase obtained by partitioning the image subchips into four equally sized, non-overlapping quadrants.

Using the covariance matrix estimates  $Q_0$  in (140) and  $Q_1$  in (141) and an ENL of 7 the detection performance of the mean backscatter power ratio, the sample coherence and the log likelihood change statistic may be computed using theoretical expressions for the probability of detection  $P_d$  and false alarm  $P_{fa}$  derived in Sections 4 and 5. Figure 45 shows the theoretical and simulated ROC curves for the three change statistics. It is evident that the log likelihood ratio statistic gives almost an order of magnitude improvement in the false alarm rate over both the sample coherence and mean backscatter power ratio statistics over a wide range of detection probabilities. The mean backscatter power ratio and sample coherence change statistics both give somewhat similar detection performance characteristics with the mean backscatter power ratio statistic showing a modest detection improvement over the sample coherence at values of  $P_d$  less than 0.6.

The images on the left hand side of Figure 46 shows the three change statistics evaluated over the primary and repeat pass image pair using a 3 by 3 sliding computation window. In the case of the mean backscatter power ratio and sample coherence change statistic, areas subject to some form of disturbance are associated with low values for the change statistics and thus are visible as dark pixels. On the other hand for the log likelihood change statistic scene disturbances are associated with large values of the change statistic. In Figure 46 however, the negative of the log likelihood change statistic is displayed so that changed areas are visible as dark pixels. The area of the scene modified by the rotary hoe is readily identified in the three change statistic maps however, the sample coherence and mean backscatter power ratio maps appear somewhat noisier than the log likelihood change map.

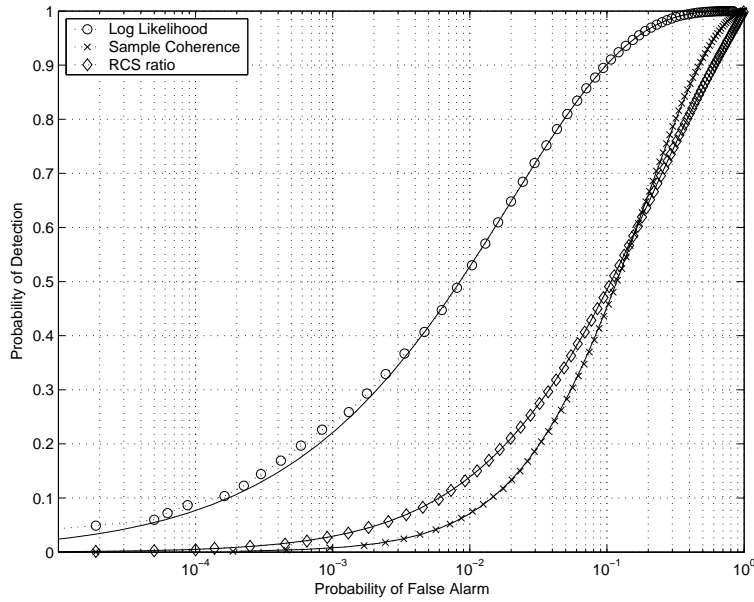


**Figure 45:** Theoretical and simulated ROC curves of the three change statistics obtained using the covariance matrix estimates given in equation (140) with an  $ENL=7$ .

On the right hand side of Figure 46 are the change detections obtained by applying a threshold to the corresponding change statistic maps. The threshold has been adjusted experimentally in each case, to achieve a fixed number of detections (false alarms) in the 2000 pixel area lying outside the modified region, thereby giving a fixed false alarm rate of 0.05. It can be readily seen that for the same total number of false detections in the region surrounding the modified area the log likelihood change statistic has generated far more detections within the modified area than either the mean backscatter power ratio map or the sample coherence, i.e., the log likelihood change statistic has generated a significant number of new detections that are not identified by either the sample coherence or the mean backscatter power ratio statistic. Furthermore the mean backscatter power ratio and sample coherence statistics do not necessarily generate false detections at the same spatial locations. Therefore a simple fusion of the mean backscatter power ratio and sample coherence detection results will not necessarily generate an improved detection performance.

The probability of detection for each change statistic may be estimated experimentally by assuming all pixels within the modified region are realisations of the  $H_1$  hypothesis, i.e., changed, and counting the total number of detections in this area. The probability of detection for each change statistic may then be compared to the theoretical performance given in the ROC curve of Figure 45. Table 2 shows the theoretical and experimentally determined detection performance and associated threshold required to achieve a false alarm rate of 0.05. There appears to be reasonably good agreement between the theoretical and experimentally determined results. The trends identified in the ROC curve of Figure 45 are evident with the log likelihood giving significantly better detection performance than both the mean backscatter power ratio and sample coherence change statistics. A number of differences between the experimental and theoretical values do

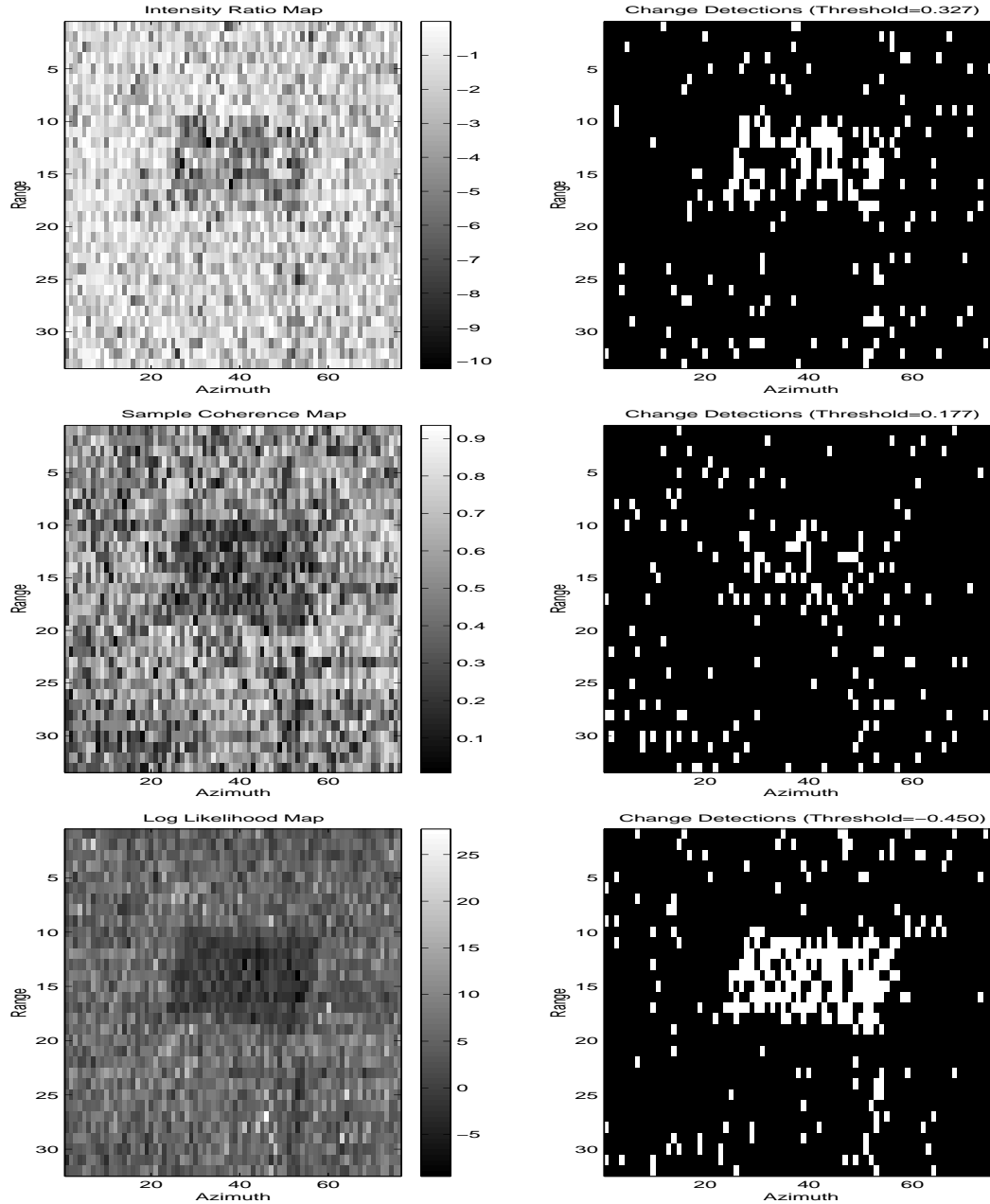


**Figure 46:** The images on the left hand side show, from top to bottom, the mean backscatter power ratio, sample coherence and log likelihood change statistic maps evaluated over the subsampled subchip image pair using a 3 by 3 pixel sliding estimation window. Scene changes are identified as dark pixels. The images on the right hand side show the detections obtained by applying a threshold to the corresponding change maps. The threshold has been experimentally selected to give a false alarm rate of 0.05.

Change Statistic	ROC threshold	Theoretical $P_d$	Expt. Threshold	Expt. $P_d$
Log Likelihood	-1.45	0.70	-0.45	0.71
Sample Corr.	0.19	0.21	0.18	0.23
Intensity Ratio	0.31	0.28	0.33	0.42

**Table 2:** Theoretical and experimental threshold levels and probability of detection values of the three change statistics corresponding to a false alarm probability of 0.05 over the 20 m by 20 m modified area.

appear. The experimentally determined threshold for the log likelihood change statistic is somewhat larger than predicted theoretically. The theoretically derived ROC performance however is an upper bound as it fails to consider the impact of the estimates of  $Q_0$  and  $Q_1$  which would tend to broaden the density functions of the change statistic under  $H_0$  and  $H_1$  leading higher false alarms for a given probability of detection. A higher detection threshold might thus be anticipated in order to maintain a desired false alarm rate. The mean backscatter power ratio statistic gives a somewhat better detection performance than predicted theoretically, possibly indicating a greater mean backscatter power change than the estimated 2.73 dB change.

## 6.2 Repeat Pass Image Pair 2

Figures 47 and 48 show the primary and repeat pass image pair selected for change detection analysis. The 3 dB resolution of the SLC images generated by the SAR processor is 0.52 m range by 0.15 m azimuth with a Hamming window applied and a pixel spacing of 0.34 m by 0.11 m. The slant range and depression angle offsets at aperture midpoint are 69.65 m and 0.035 degrees respectively. Local estimates of the mean backscatter power and complex sample cross correlation coefficient have been obtained by firstly upsampling the SLC imagery by a factor of 2, applying a 4 (range) by 12 (azimuth) pixel sliding estimation window, then decimating by factors of 2 in range and 6 in azimuth yielding pixel spacings of 0.343 m in range and 0.34 m in azimuth. The 3 dB resolution of the mean backscatter power ratio change map and the coherence and interferometric phase subsequently formed has been numerically evaluated to be 0.57 m in range and 0.22 m in azimuth.

Figure 49 shows the mean backscatter power ratio change map for the image pair while Figures 50 and 51 show the coherence and interferometric phase respectively. The scene changes carried out with the rotary hoe and lawn mower outlined in Figure 35 are difficult to discern in the mean backscatter power ratio change map however, they appear quite clearly in the coherence map as areas of low coherence and as areas of rapid, random phase fluctuations in the interferometric phase map. Other areas of low coherence (or rapid phase fluctuations) include the shadowed areas as well as the road. In these areas there is little backscattered signal evident in the transduced imagery and hence the coherence estimated is dominated by the uncorrelated radar system noise. The tree returns in the image also appear as areas of low coherence due to the movement of the leaves and branches that occurs both during data collection and in the interval between collection.



**Figure 47:** *Intensity SAR image generated from the primary pass imaging collection processed to a resolution of 0.52 m (range) by 0.150 m (azimuth) with a Hamming window applied.*



**Figure 48:** Intensity SAR image generated from the repeat pass imaging collection processed to a resolution of 0.52 m (range) by 0.150 m (azimuth) with a Hamming window applied.

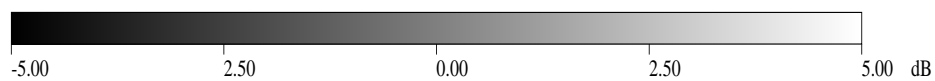
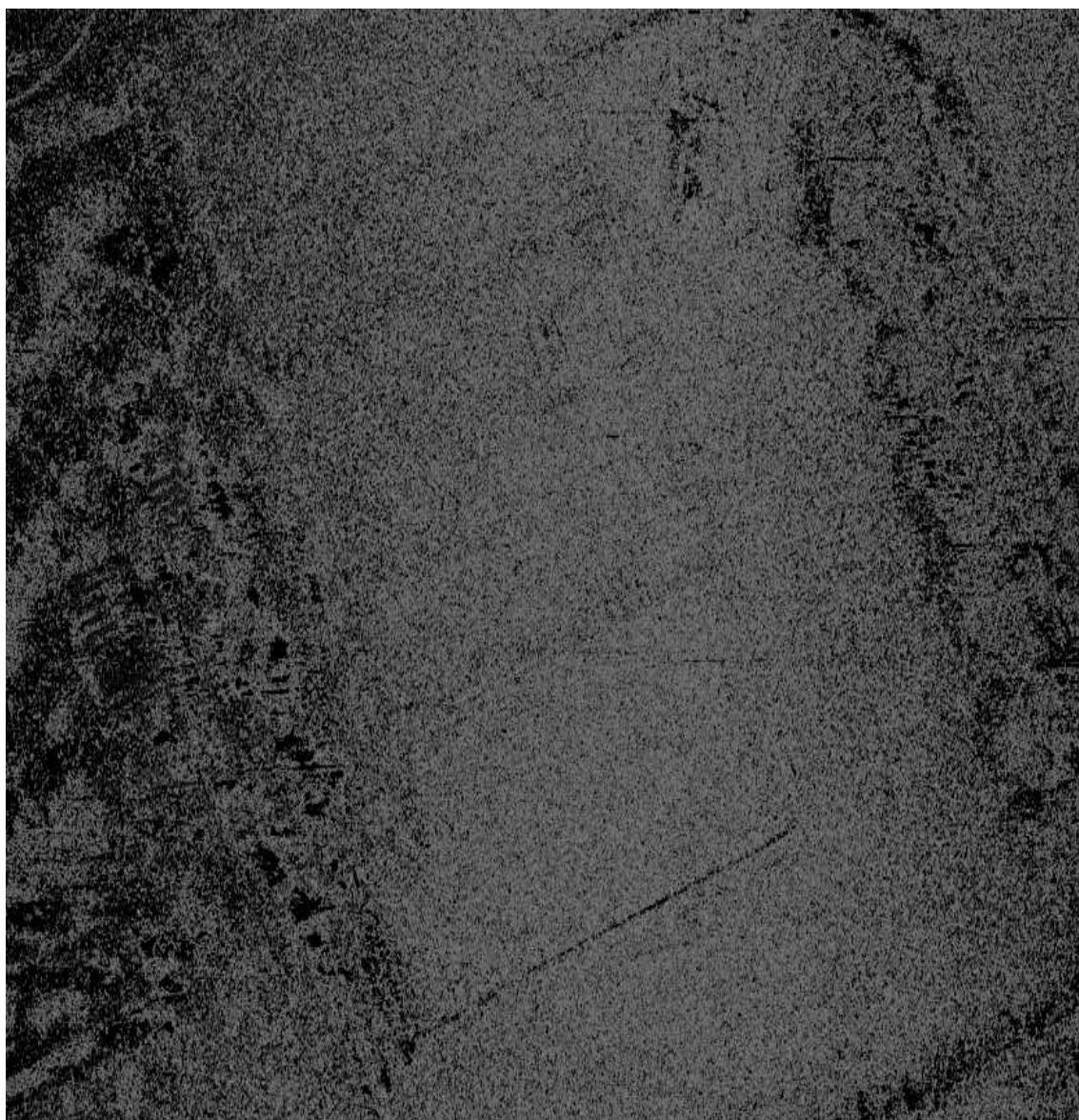


**Figure 49:** Mean backscatter power ratio change statistic evaluated over the primary and repeat pass image pair using a 2 (range) by 6 (azimuth) pixel spatial estimation window. The resolution of the estimate is 0.57 m by 0.22 m with a pixel spacing of 0.343 m by 0.34 m.

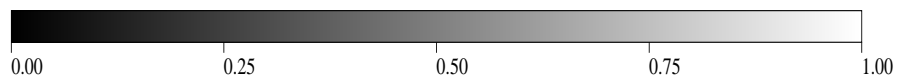
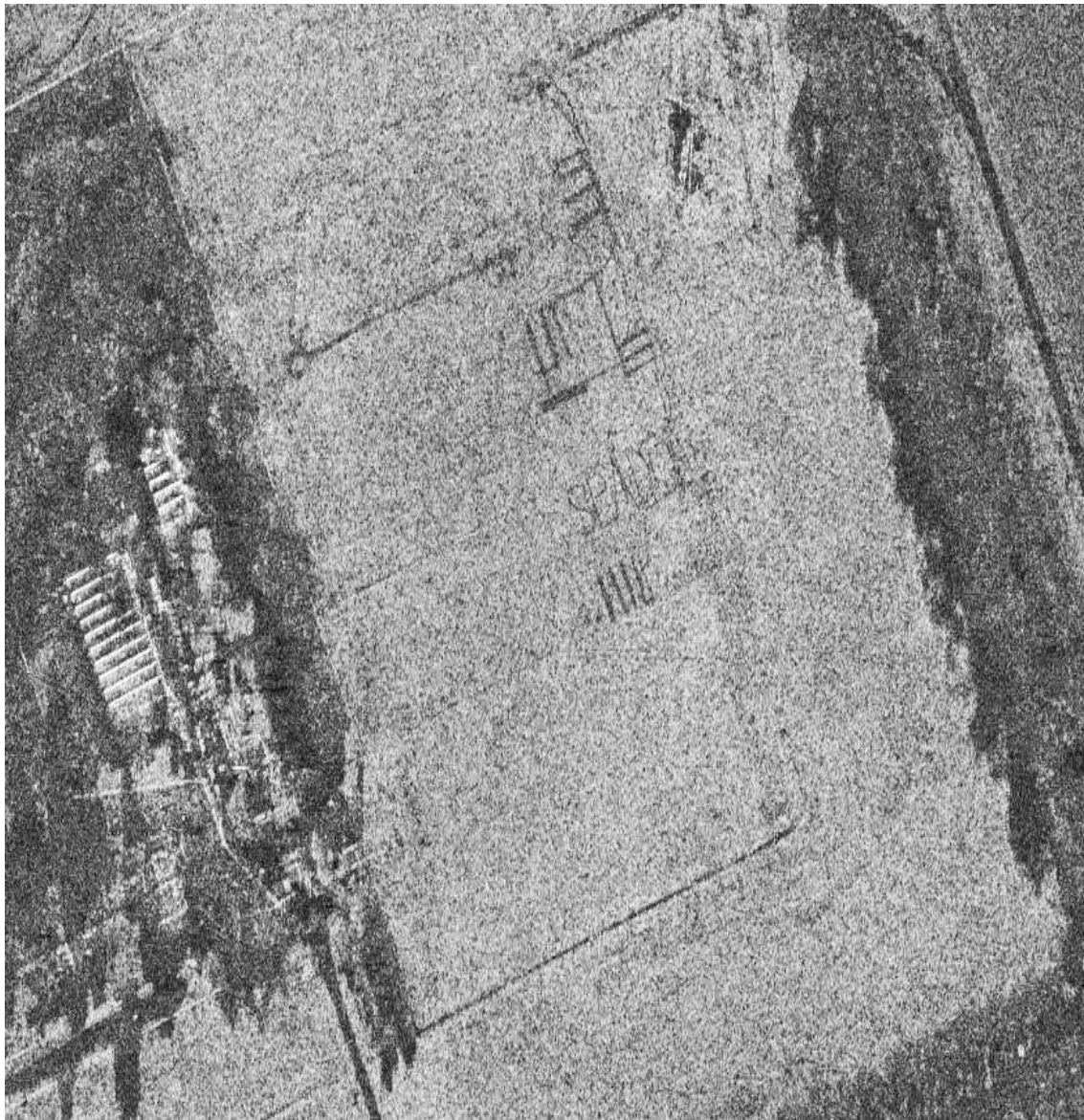


**Figure 50:** Sample coherence evaluated over the repeat pass image pair using a 2 by 7 pixel spatial estimation window. The resolution of the estimate is 0.57 m by 0.22 m with a pixel spacing of 0.343 m by 0.34 m.



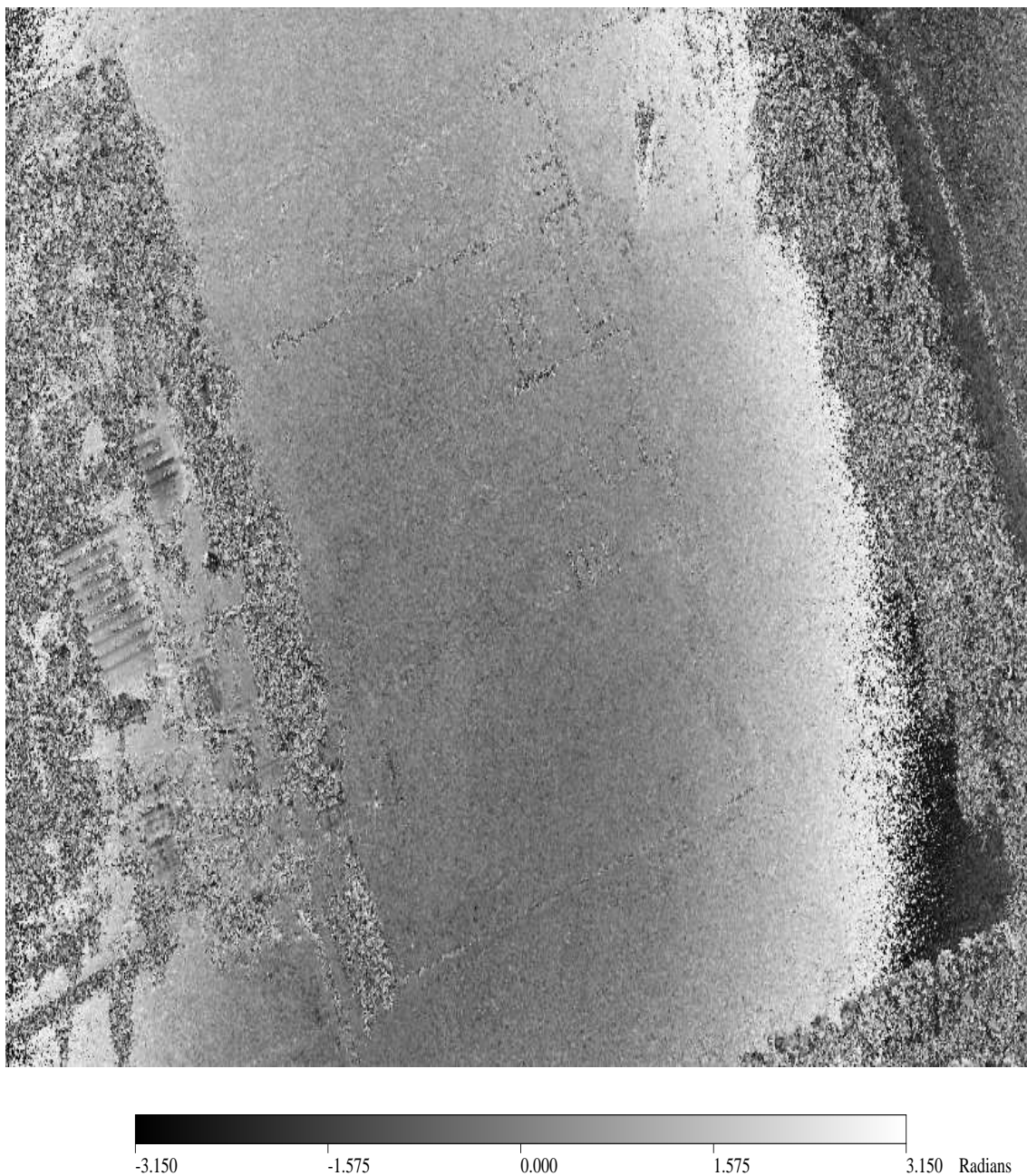


**Figure 51:** Sample interferometric phase evaluated over the repeat pass image pair using a 2 by 7 pixel spatial estimation window. The resolution of the estimate is 0.57 m by 0.22 m with a pixel spacing of 0.343 m by 0.34 m.

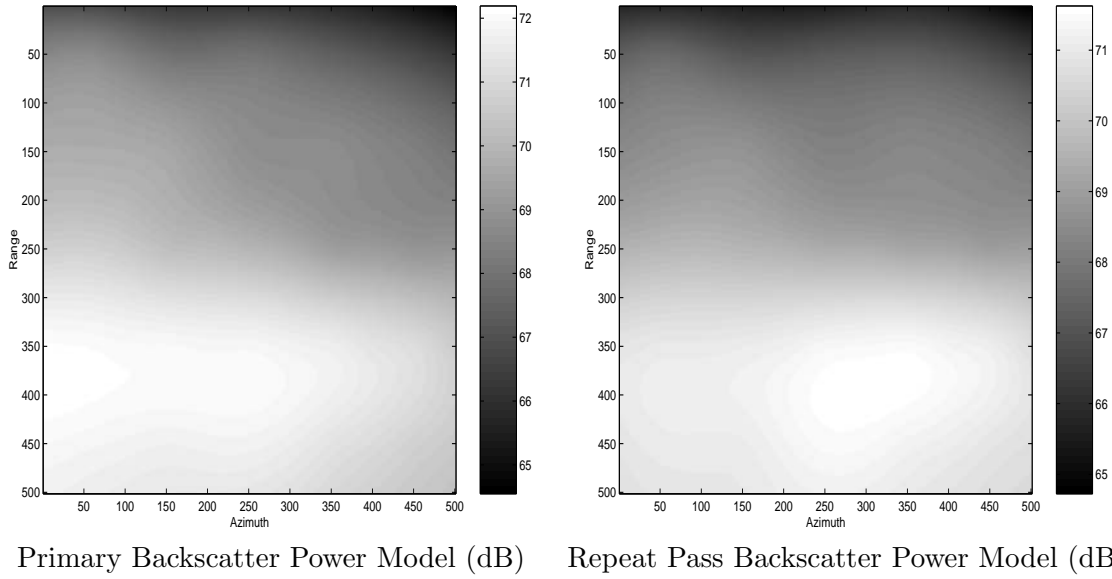


**Figure 52:** *Thin plate spline models describing the spatial variation of the mean backscatter power of the primary pass image subchip, indicated on the left and repeat pass image subchip indicated on the right.*

### 6.2.1 Joint Statistics of the Repeat Pass Pair

For the purposes of applying the change detection algorithms, image subchips, as indicated in Figure 47, have been extracted from the primary and repeat pass images. This image subchip pair encompasses a large portion of the open field including the ground truthed scene changes illustrated in Figure 35. The extracted image subchips have been subsampled by a factor of two in range and azimuth to reduce the correlation between neighbouring pixels and allow validation of the theoretical distributions of the change statistics (see Section 6.1.1). The size of the subsampled image chips is 500 by 500 pixels.

To allow for possible variation in the mean backscatter power across the subchip pair each subchip has been partitioned into 25 non-overlapping regions each 100 by 100 pixels in size over which sample estimates of the backscatter power have been computed. A thin plate spline has been fitted to both the primary and repeat pass sample estimates to model the spatial variation of the backscatter power across the scene. Figure 52 shows the thin plate spline models obtained for the mean backscatter power of the primary and repeat pass image subchips. The models indicate that the mean backscatter power across the image subchips varies by approximately 6 dB. This may possibly be due to an error in the antenna pointing accuracy resulting in an antenna beampattern variation across the scene.

The amplitude and phase statistics of one of the 100 by 100 pixel regions, having approximately uniform mean backscatter power, have been computed and compared to the Rayleigh amplitude model. Figure 53 shows the amplitude histograms of the primary and repeat pass 100 by 100 pixel image region. Superimposed on the histograms are the theoretical Rayleigh amplitude density functions that arise in the case when the scattering

may be modelled by a complex Gaussian process. Figure 54 shows the phase histograms associated with the 100 by 100 pixel regions computed for the primary and repeat pass images as well as the theoretical uniform phase probability density function. Also shown in the plots of Figures 53 and 54 are the likely ranges in variation of the histogram estimates of the PDFs, that are to be expected assuming the Rayleigh amplitude and uniform phase PDFs are accurate models. The range of expected values shown are the  $\pm$  three standard deviations about the mean expected at each histogram sample bin. The mean backscatter power coefficients required to specify the theoretical amplitude distributions have been estimated by averaging the image pixel intensities over the entire 100 by 100 pixel region,

$$\text{Primary Image: } \hat{\sigma}_f^2 = \frac{1}{N} \sum_{k=1}^N |f_k|^2 = 1.0728 \times 10^7, \quad (143)$$

$$\text{Repeat Image: } \hat{\sigma}_g^2 = \frac{1}{N} \sum_{k=1}^N |g_k|^2 = 9.6785 \times 10^6, \quad (144)$$

where  $N = 10,000$ .

The phase histograms of the primary and repeat pass image subchips in Figure 54 show good agreement with the theoretical uniform distribution. The amplitude histograms shown in Figure 53 however, exhibit a statistically significant deviation from the Rayleigh density function that is usually expected under Gaussian scattering conditions. Given that the image pair considered here have been acquired with a grazing angle of 15 degrees radar shadowing can give rise to a textural modulation across the image yielding non-Gaussian statistics. The K distribution [12] can be used to describe textured scenes and a fit to the image amplitude data is show in Figure 55. The K distribution appears to provide a much better fit to the amplitude data. Computing the K distribution order parameter  $\hat{\nu}$  using spatial estimates of the second and fourth order moments gives  $\hat{\nu} = 7.9$  and  $\hat{\nu} = 6.8$  for the primary and repeat pass images respectively. These values indicate that the statistics of the image subchips lie in the transition region between Gaussian and markedly non-Gaussian scattering behaviour, where non-Gaussian scattering is characterised by  $\hat{\nu} < 1$  and Gaussian scattering by  $\hat{\nu} > 10$ .

Assuming the textural modulation spatial variation over the scene is on a scale greater than the image resolution cell then it has been demonstrated [20], [53] that the sample correlation coefficient may be used to estimate the underlying cross correlation of the image pair in the unchanged regions. Also the sample estimate will have the same probability density function as in the Gaussian scattering case.

Ground truth observations indicate that the field in the imaged scene is relatively homogeneous with respect to the type of vegetation, its coverage and size. Therefore the scene coherence of the image subchips is expected to be constant and a histogram of sample estimates computed over the entire image subchip pair may be obtained and compared to the theoretical density function given in equation (101). Figure 56 shows the sample coherence histogram obtained using a 3 by 3 sliding estimation window applied over the entire image subchip pair. Also shown is the theoretical density function of the sample coherence where a true coherence of 0.62 and ENL of 7 have been found to provide the best fit to the experimental histogram. Also shown in Figure 56 is the likely range in variation (three standard deviations) of the histogram estimate of the PDF that is to be expected assuming the sample estimate has the same PDF as the Gaussian scattering case. The theoretical density function and experimental histogram are in excellent agreement

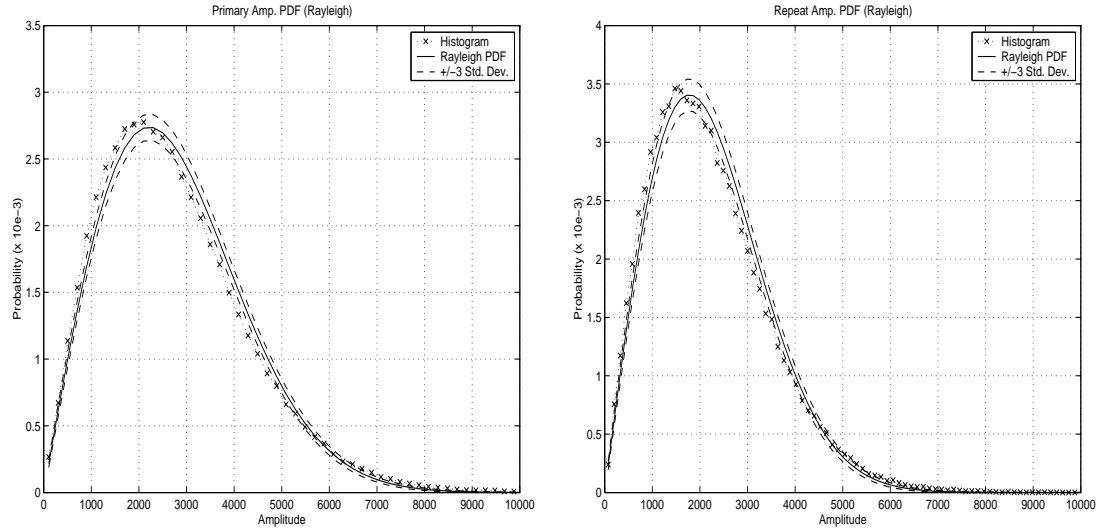
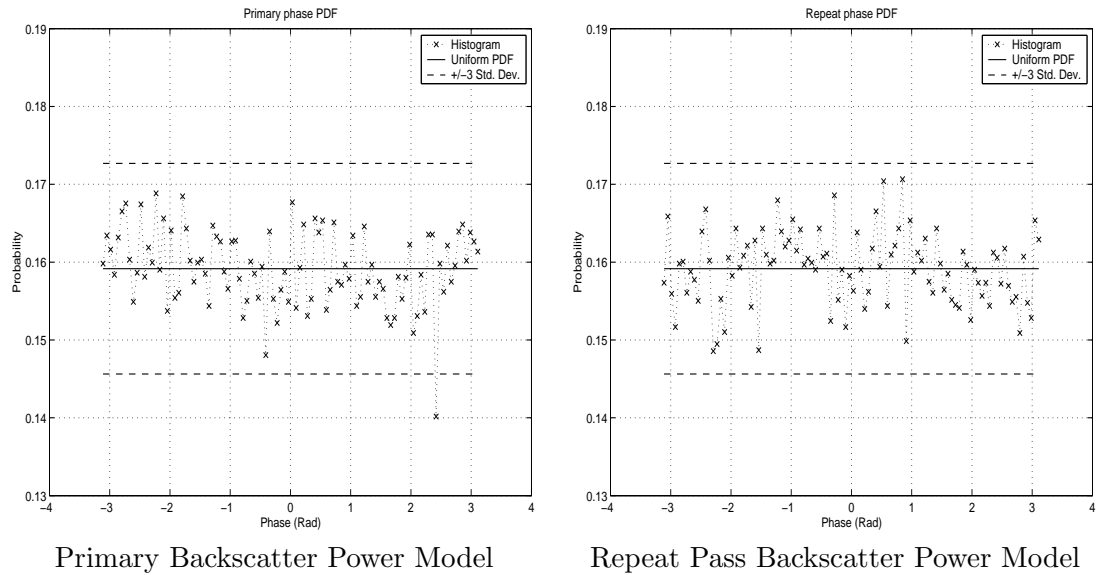


**Figure 53:** Amplitude histograms for a 100 by 100 pixel primary and repeat pass image region. Superposed on the histograms are the theoretical Rayleigh amplitude distributions corresponding to Gaussian scattering.



Primary Backscatter Power Model

Repeat Pass Backscatter Power Model

**Figure 54:** Phase histograms for a 100 by 100 pixel primary and repeat pass image region. Superposed on the histograms is the theoretical uniform phase probability density function.

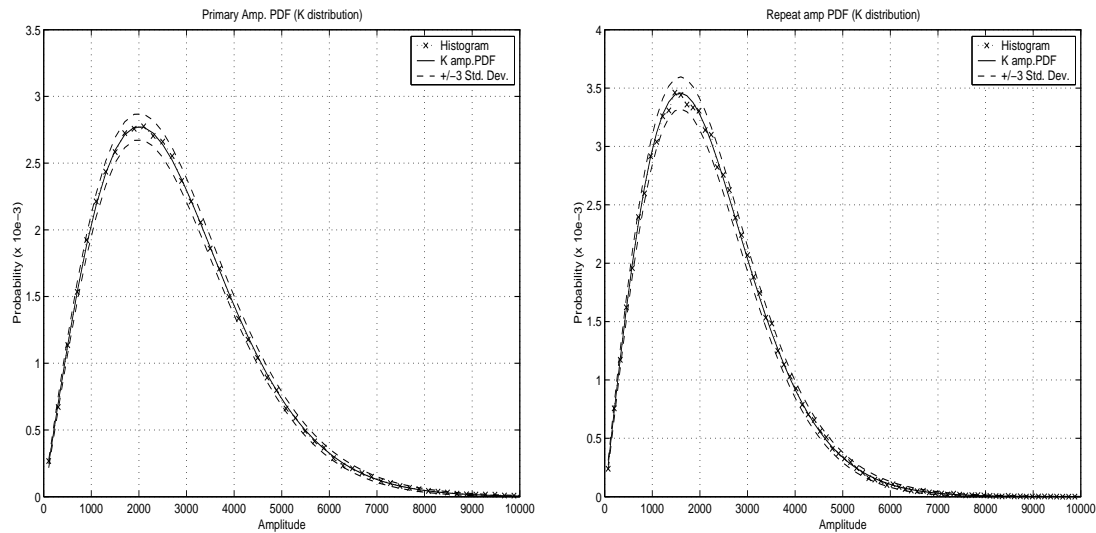


**Figure 55:** Amplitude histograms for a 100 by 100 pixel primary and repeat pass image region. Superposed on the histograms are the theoretical  $K$  amplitude distributions.

with only a slight deviation at low coherence values due to the inclusion of the modified low coherence areas in the computation of the sample coherence.

The interferometric phase may vary across the scene depending on the terrain topography and any uncompensated relative phase terms that remain after image formation. To allow for this possible spatial variation, the sample estimates of the interferometric phase obtained from the 3 by 3 pixel sliding estimation window have been used to generate a thin plate spline model of the interferometric phase variation across the image subchip pair. Figure 57 shows the sample estimates of the scene and the corresponding thin plate spline model. From the model the phase varies by 134 degrees across the image subchip scene.

### 6.2.2 Change Detection Performance

In the previous section it has been shown that the repeat pass image pair exhibit a degree of textural modulation. However, the textural modulation is only modest and the statistics of the image pair lie in the transition region between Gaussian and markedly non-Gaussian. Therefore the sample coherence and log likelihood change statistics may still be used to provide some measure of discrimination between the changed and unchanged areas of the scene. It is noted though that the detection performance may be suboptimal as the full, complete statistical description of the repeat pass pair is not being used. Describing the unchanged and changed image subchips as jointly Gaussian random processes with covariance matrices,

Unchanged Hypothesis:

$$Q_0(x, y) = \begin{bmatrix} \sigma_f^2 & 0.62\sigma_f\sigma_g\exp(j\Phi) \\ 0.62\sigma_f\sigma_g\exp(-j\Phi) & \sigma_g^2 \end{bmatrix}, \quad (145)$$

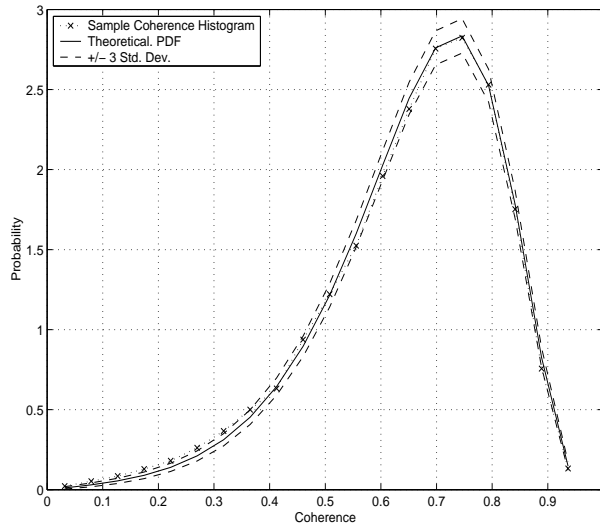


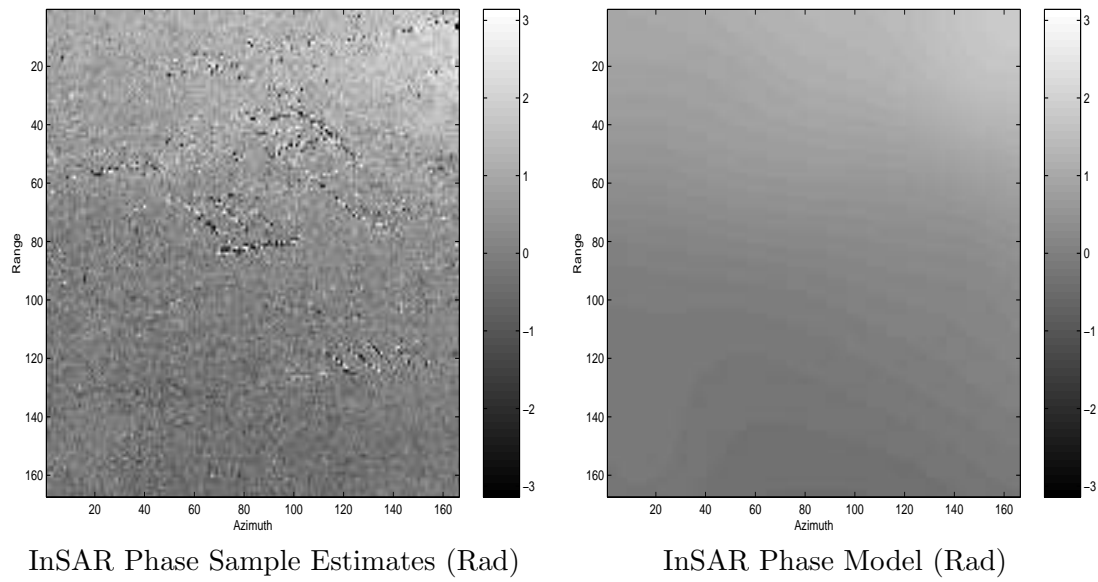
**Figure 56:** Histogram and theoretical density functions for the sample coherence evaluated from the primary and repeat pass image subchips. A true coherence of 0.62 and an ENL = 7 have been used to specify the theoretical sample coherence density function.

Changed Hypothesis:

$$Q_1(x, y) = \begin{bmatrix} \sigma_f^2 & 0 \\ 0 & \sigma_g^2 \end{bmatrix}, \quad (146)$$

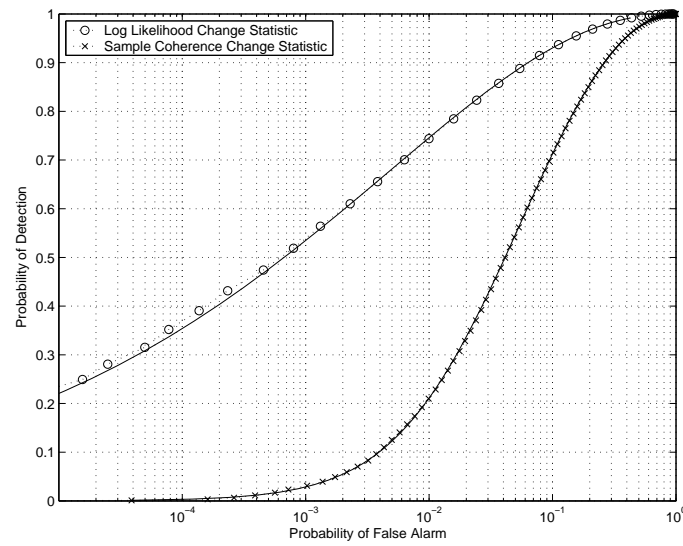
respectively, the detection performance of the sample coherence and the log likelihood change statistics may be computed using the theoretical Gaussian expressions for  $P_d$  and  $P_{fa}$  derived in Sections 4 and 5. In (145) and (146)  $\sigma_f^2$  and  $\sigma_g^2$  are the mean backscatter power models of the primary and repeat pass image subchips shown in Figure 52 and the interferometric phase  $\Phi$  is given by the model illustrated in Figure 57. Figure 58 shows the theoretical as well as simulated ROC curves for the two change statistics. It is evident that, under the jointly Gaussian scattering assumption, the log likelihood change statistic offers over an order of magnitude improvement in the detection performance over the sample coherence change statistic.

Figure 59 shows the sample coherence and log likelihood change maps evaluated over the scene using the covariance models  $Q_0$  and  $Q_1$  above. Also shown are the change detections obtained by applying appropriate thresholds to the coherence and log likelihood change maps. The thresholds applied in each case have been experimentally determined to achieve a fixed number of false alarms in an area known to have no ground changes thereby giving a  $P_{fa} = 0.018$ . It is clear that the log likelihood change statistic has a significantly better detection performance allowing the scene disturbances to be more readily discerned. While it is difficult to quantify the experimental  $P_d$  given the size and geometry of the disturbances, an estimate based on one of the modified strips yields a  $P_d$  of 0.68 for the log likelihood change statistic and 0.30 for the sample coherence. These compare favourably with the theoretical values obtained from Figure 58 of 0.795 for the log likelihood and 0.31 for the sample coherence. The experimental probability of detection for the log likelihood change statistic is slightly less than the theoretically predicted value. Possible reasons



**Figure 57:** *The image on the left hand side indicates sample estimates of the interferometric phase obtained using a 3 by 3 pixel sliding estimation window. On the right hand side is a thin plate spline fit to the sample estimates of the interferometric phase.*

for this discrepancy include deviations from the theoretical density functions due to the presence of texture in the scene imagery, small errors in the estimation of the covariance matrices  $Q_0$  and  $Q_1$  and their spatial variation, as well as inaccuracies in the estimation of the experimental  $P_d$  due to the small sample size.



**Figure 58:** Theoretical and simulated ROC curves of the sample coherence and log likelihood change statistics using the change scenario specified by the covariance matrices given in (145) and (146).



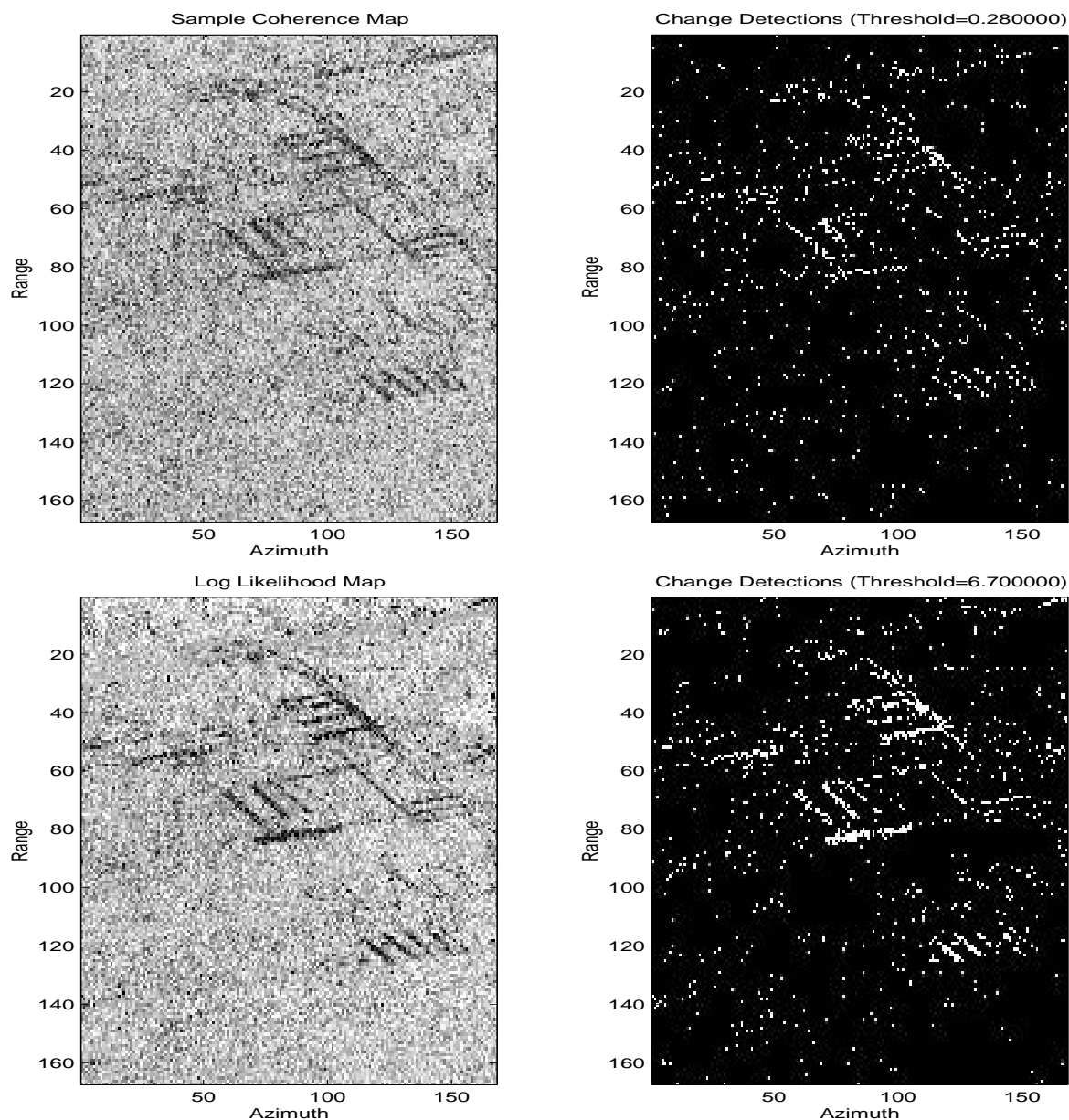


**Figure 59:** The images on the left hand side show, from top to bottom, the sample coherence and log likelihood change statistic maps evaluated over the subchip image pair using a 3 by 3 pixel spatial estimation window. The images on the right hand side show the detections obtained by applying a threshold to the corresponding change maps. The thresholds have been experimentally selected to give a false alarm rate of 0.018

## 7 Summary and Future Work

In this report the problem of detecting fine scale scene changes using repeat pass synthetic aperture radar interferometry has been examined. As SAR is a coherent imaging system two forms of change detection may be considered, namely incoherent change detection and coherent change detection. Incoherent change detection identifies changes in the mean backscatter power of a scene by comparing the average intensities of the image pair. Coherent change detection on the other hand identifies changes in the scene by quantifying changes in the transduced amplitude and phase of the image pair. Since the transduced image amplitude and phase is dependent on the scene's subresolution scattering structure, CCD can potentially detect subtle changes to the location and distribution of scattering centres within a resolution cell. In order to fully realise the potential of coherent change detection however, the SAR image pairs must be acquired with very careful control of the repeat pass imaging geometries. Furthermore additional processing steps are required to estimate and compensate for mismatch between the SAR acquisition functions and image formation processors employed to form the repeat pass images.

This report begins by describing the SAR acquisition and image formation process for the spotlight SAR mode leading to a mathematical description of a SAR image. This model for a SAR image is subsequently used in Section 3 as the basis for describing a repeat pass interferometric image pair. The additional information made available by the interferometric processing of a SAR image pair is given by the complex cross correlation coefficient. The magnitude of the complex cross correlation coefficient, commonly referred to as the coherence quantifies the similarity of the images while the phase is a function of the offset in the imaging geometries and the terrain height. Sources of image domain decorrelation in an interferometric image pair are identified and techniques for minimising the decorrelation are discussed.

The problem of detecting scene changes is then addressed in Sections 4 and 5 by considering three change statistics namely: the average image intensity ratio for detecting changes in the mean backscatter power of the scene, the sample coherence for detecting areas of interferometric decorrelation in the scene and the log likelihood change statistic in which the problem is formulated in a rigorous hypothesis testing framework. Theoretical expressions for the probability of detection versus false alarm as a function of detection threshold were derived to quantify the detection performance of the three change statistics. The log likelihood change statistic was shown to yield superior detection performance to the commonly used averaged intensity ratio and sample coherence with approximately an order of magnitude improvement in false alarm rate for a 0.7 probability of detection. Finally in Section 6 the three change statistics were applied to experimental repeat pass SAR data acquired with the DSTO Ingara X-band SAR. The detection performance of the change statistics in detecting various deliberate scene changes was shown to be in good agreement with the theoretical derivations.

### 7.1 Future Work

The detection of scene changes in this report is performed on a pixel-by-pixel basis. An examination of the sample coherence maps for the experimental scene changes however,

shows that a strong visual cue for detecting the low coherence scene changes is the spatial correlation of the disturbances. Improvements in the detection of scene changes may possibly be achieved by exploiting this spatial correlation either via a correlated neighbourhood model in the scene change hypothesis or alternatively using the change detections as input into a tracking algorithm.

Repeat pass SAR interferometric change detection uses multiple, multi-date images of a scene to distinguish between the consistent and changed scattering contributions of a scene. Improvements in resolving different scattering behaviour in a scene may be accomplished by making additional observations at different wavelengths, incidence angles and different polarisations. The potential for such additional observations to improve change detection performance warrant further investigation.

## 8 Acknowledgements

The authors wish to acknowledge the contributions of Professor Doug Gray at Adelaide University to the development of the log likelihood detection statistic and the members of the Imaging Radar Systems group in the development and operation of the Ingara imaging radar system. The authors would also like to thank Dr Paul Berry for thoroughly reviewing a draft copy of this report.

## References

1. D. G. Corr, G. E. Keyte, and S. Whitehouse, "Studies of decorrelation in multi-temporal SAR imagery," in *Proceedings of the 1995 International Geoscience and Remote Sensing Symposium*, 1995, pp. 1026–1028.
2. H. A. Zebker and J. Villasenor, "Decorrelation in interferometric radar echoes," *IEEE Transactions on Geoscience and Remote Sensing*, vol. 30, no. 5, pp. 950–959, 1992.
3. J. Askne, P. B. G. Dammert, L. M. H. Ulander, and G. Smith, "C-Band repeat-pass interferometric SAR observations of the forest," *IEEE Transactions on Geoscience and Remote Sensing*, vol. 35, no. 1, pp. 25–35, 1997.
4. J. Askne and J. O. Hagberg, "Potential of interferometric SAR for classification of land surfaces," in *Proceedings of the 1993 International Geoscience and Remote Sensing Symposium*, vol. 3, 1993, pp. 985–987.
5. D. A. Yocky, "Interferometric SAR coherence classification utility assessment," in *Proceedings of the 1998 IEEE International Geoscience and Remote Sensing Symposium*, vol. 4, 1998, pp. 1784–1786.
6. D. Geudtner, R. Winter, and P. W. Vachon, "Flood monitoring using ERS-1 SAR interferometry coherence maps," in *Proceedings of the 1998 International Geoscience and Remote Sensing Symposium*, vol. 2, 1996, pp. 966–968.
7. D. G. Corr, "Coherence change detection for urban development monitoring," in *Proceedings of the 1997 IEEE Colloquium on Radar Interferometry*, vol. 6, 1997, pp. 1–6.
8. D. G. Corr and A. Rodrigues, "Coherent change detection of vehicle movements," in *Proceedings of the 1998 International Geoscience and Remote Sensing Symposium*, vol. 5, 1998, pp. 2451–2453.
9. C. V. Jakowatz Jr., D. E. Wahl, P. H. Eichel, D. C. Ghiglia, and P. A. Thompson, *Spotlight-Mode Synthetic Aperture Radar: A Signal Processing Approach*. Kluwer Academic Publishers, 1996.
10. R. Scheiber and A. Moreira, "Co-registration of interferometric SAR images using spectral diversity," *IEEE Transactions on Geoscience and Remote Sensing*, vol. 38, no. 5, pp. 2179–2191, 2000.
11. E. J. M. Rignot and J. J. van Zyl, "Change detection techniques for ERS-1 SAR data," *IEEE Transactions on Geoscience and Remote Sensing*, vol. 31, no. 4, pp. 896 – 906, July 1993.
12. C. Oliver and S. Quegan, *Understanding Synthetic Aperture Radar Images*. Artech House, 1998.
13. L. M. Novak, G. J. Owirka, and A. L. Weaver, "Automatic target recognition using enhanced resolution SAR data," *IEEE Transactions on Aerospace and Electronic Systems*, vol. 35, pp. 157–175, 1999.

14. A. R. Brenner and J. H. G. Ender, "Very wideband radar imaging with the airborne SAR sensor PAMIR," in *Proceedings of the 2003 IEEE International Geoscience and Remote Sensing Symposium*, vol. 1, 2003, pp. 544–535.
15. H. M. J. Cantalloube and P. Dubois-Fernandez, "Airborne X-band SAR imaging with 10 cm resolution - Technical challenges and preliminary results," in *Proceedings of the 2003 International Geoscience and Remote Sensing Symposium*, vol. 1, 2003, pp. 185–187.
16. D. C. Munson, J. D. O'Brien, and W. K. Jenkins, "A tomographic formulation of spotlight-mode synthetic aperture radar," *Proceedings of the IEEE*, vol. 71, no. 8, pp. 917–925, 1983.
17. J. L. Walker, "Range-doppler imaging of rotating objects," *IEEE Transactions on Aerospace and Electronic Systems*, vol. 16, no. 1, pp. 23–52, January 1980.
18. A. Reigber and A. Moreira, "First demonstration of airborne SAR tomography using multibaseline L-band data," *IEEE Transactions on Geoscience and Remote Sensing*, vol. 38, no. 5, pp. 2142–2152, 2000.
19. M. Preiss, "Detecting scene changes using synthetic aperture radar interferometry," Ph.D. dissertation, School of Electrical and Electronic Engineering, The University of Adelaide, 2004.
20. C. H. Gierull, *Statistics of SAR interferograms with application to moving target detection*. Defence Research Establishment Ottawa, Canada, July Tech. Rep. TR2001-045, 2001.
21. —, "Unbiased coherence estimator for SAR interferometry with application to moving target detection," *Electronics Letters*, vol. 37, no. 14, pp. 913–915, 2001.
22. R. M. Goldstein, T. P. Barnett, and H. A. Zebker, "Remote sensing of ocean currents," *Science*, vol. 246, pp. 1282–1285, 1989.
23. E. J. M. Rignot and J. J. van Zyl, "Change detection techniques for ERS-1 SAR data," *IEEE Transactions on Geoscience and Remote Sensing*, vol. 31, no. 4, pp. 896 – 906, July 1993.
24. A. K. Gabriel, R. M. Goldstein, and H. A. Zebker, "Mapping small elevation changes over large areas: Differential radar interferometry," *Journal of Geophysical Research*, vol. 94, no. B7, pp. 9183–9191, 1989.
25. A. Ferretti, C. Prati, and F. Rocca, "Permanent scatterers in SAR interferometry," *IEEE Transactions on Geoscience and Remote Sensing*, vol. 39, no. 1, pp. 8–20, 2001.
26. I. I. Shapiro, S. H. Zisk, A. E. E. Rogers, M. A. Slade, and T. W. Thompson, "Lunar topography: Global determination by radar," *Science*, vol. 178, pp. 939–948, 1972.
27. S. H. Zisk, "Lunar topography: First radar-interferometer measurements of the alphonsus-ptolemaeus-arzachel region," *Science*, vol. 178, pp. 977–980, 1972.
28. —, "A new, Earth-based radar technique for the measurement of lunar topography," *The Moon*, vol. 4, pp. 296–306, 1972.

29. L. C. Graham, "Synthetic interferometric radar for topographic mapping," *Proceedings of the IEEE*, vol. 62, pp. 763–768, 1974.
30. H. A. Zebker and R. M. Goldstein, "Topographic mapping from interferometric SAR observations," *Journal of Geophysical Research*, vol. 91, pp. 4993–4999, 1986.
31. J. C. Curlander and R. N. McDonough, *Synthetic Aperture Radar, Systems and Signal Processing*. Wiley and Sons, 1991.
32. F. Gatelli, A. M. Guamieri, and F. Parizzi, "The wavenumber shift in interferometry," *IEEE Transactions on Geoscience and Remote Sensing*, vol. 32, no. 4, pp. 855–865, July 1994.
33. D. Just and R. Bamler, "Phase statistics of interferograms with applications to synthetic aperture radar," *Applied Optics*, vol. 33, no. 20, pp. 4361–4368, July 1994.
34. F. L. Bookstein, "Principal warps: Thin-plate splines and the decomposition of deformations," *IEEE Transactions on Pattern Analysis and Machine Intelligence*, vol. 11, no. 6, pp. 567–585, June 1989.
35. A. Goshtasby, "Registration of images with geometric distortions," *IEEE Transactions on Geoscience and Remote Sensing*, vol. 26, no. 1, pp. 60–64, 1988.
36. R. Touzi, A. Lopes, and P. Bousquet, "A statistical and geometrical edge detector for SAR images," *IEEE Transactions on Geoscience and Remote Scensing*, vol. 26, no. 4, pp. 764–773, 1988.
37. J. W. Goodman, *Statistical Optics*. Wiley, 2000.
38. P. Beckmann and A. Spizzichino, *The Scattering of Electromagnetic Waves from Rough Surfaces*. Norwood, Massachusetts: Artech House, 1987.
39. A. Singh, "Digital change detection techniques using remotely sensed data," *International Journal of Remote Sensing*, vol. 10, pp. 989–1003, 1989.
40. S. Quegan and I. Rhodes, "Statistical models for polarimetric data: Consequences, testing and validity," *International Journal of Remote Sensing*, vol. 16, no. 7, pp. 1183–1210, 1995.
41. R. Touzi, A. Lopes, and P. Bousquet, "A statistical and geometrical edge detector for SAR images," *IEEE Transactions on Geoscience and Remote Scensing*, vol. 26, no. 4, pp. 764–773, 1988.
42. M. Abramowitz and I. A. Stegun, *Handbook of Mathematical Functions with Formulas, Graphs and Mathematical Tables*. Dover Publications, 1972.
43. H. A. Zebker, "Studying the earth with interferometric radar," *IEEE Computing in Science and Engineering*, vol. 2, no. 3, pp. 52–60, 2000.
44. R. Touzi, A. Lopes, J. Bruniquel, and P. W. Vachon, "Coherence estimation for SAR imagery," *IEEE Transactions on Geoscience and Remote Scensing*, vol. 37, no. 1, pp. 135–149, 1999.

45. J. O. Hagberg, L. M. H. Ulander, and J. Askne, "Repeat-pass SAR interferometry over forested terrain," *IEEE Transactions on Geoscience and Remote Sensing*, vol. 33, no. 2, pp. 331–340, 1995.
46. A. Reigber and R. Scheiber, "Differential SAR interferometry using an airborne platform," in *Proceedings 4th European Conference on Synthetic Aperture Radar*, 2002, pp. 373–376.
47. S. M. Kay, *Fundamentals of statistic signal processing. Vol 2. Detection theory*. Prentice Hall, 1998.
48. H. Anton and C. Rorres, *Elementary Linear Algebra With Applications*. John Wiley and sons, 1987.
49. J. Lee, K. W. Hoppel, and A. R. Miller, "Intensity and phase statistics of multilook polarimetric and interferometric SAR imagery," *IEEE Transactions on Geoscience and Remote Sensing*, vol. 32, no. 5, pp. 1017–1027, 1994.
50. J. W. Goodman, "Statistical analysis based on a certain multivariate complex Gaussian distribution (An introduction)." *Annals of Statistical Analysis*, vol. 34, pp. 152–177, 1963.
51. N. J. S. Stacy, D. P. Badger, A. S. Goh, M. Preiss, and M. L. Williams, "The DSTO Ingara airborne X-band SAR polarimetric upgrade: First results," in *Proceedings of the 2003 IEEE International Geoscience and Remote Sensing Symposium*, 2003.
52. I. R. Joughin and D. P. Winebrenner, "Effective number of looks for a multilook interferometric phase distribution," in *Proceedings of the 1994 International Geoscience and Remote Sensing Symposium*, 1994, pp. 2276–2278.
53. I. R. Joughin, D. P. Winebrenner, and D. B. Percival, "Probability density functions for multilook polarimetric signatures," *IEEE Transactions on Geoscience and Remote Sensing*, vol. 32, no. 3, pp. 562–574, 1994.

## Appendix A   Comparison of Theoretical PDFs and Histogram Estimates

A number of statistical hypothesis tests are available in the literature to determine whether a given sample data set is consistent with a particular known theoretical distribution. For the case of binned data sets e.g. histogram data, the Chi-square test is the generally accepted hypothesis test, while for continuous data sets the Kolmogorov-Smirnov test is appropriate.

The Chi-square test computes the following test statistic,

$$\chi^2 = \sum_{i=1}^N \frac{(n_i - m_i)^2}{m_i}, \quad (\text{A1})$$

where  $n_i$  is the number of events observed in the  $i^{th}$  bin,  $m_i$  is the expected number of events in the  $i^{th}$  bin based on the hypothesized known distribution and the sum is over all  $N$  histogram bins. A large value of  $\chi^2$  indicates that the hypothesized distribution is not a good fit to the sample data set. Indeed when the number of events  $n_i$  in each bin is large then the  $\chi^2$  statistic has a Chi-square probability distribution and the decision to either accept or reject the hypothesized distribution may be made with a specified confidence level.

A simpler and somewhat less rigorous approach to determine whether a histogram of a sample data set is consistent with a known distribution is to model the number of events observed in the  $i^{th}$  bin using a binomial distribution. Given the total sample data size,  $N_T$  the probability of obtaining  $n_i$  samples in bin  $i$  is given by,

$$P(n_i) = \binom{N_T}{n_i} p_i^{n_i} (1 - p_i)^{N_T - n_i}, \quad (\text{A2})$$

where  $p_i$  is the probability of a sample occurring in the  $i^{th}$  bin which may be computed using the hypothesized known distribution. The mean number of samples and the variance in the  $i^{th}$  bin in the binomial model are given by,

$$\mu_i = N_T p_i, \quad (\text{A3})$$

$$\sigma_i^2 = N_T p_i (1 - p_i), \quad (\text{A4})$$

respectively. These values indicate the number samples that are to be anticipated in each histogram bin as well as the likely range in the number of samples about the expected value assuming that the sample data set is described by the hypothesized distribution. For the case when the number of samples in a particular bin is large the central limit theorem may be applied and the binomial distribution may be approximated by a Gaussian with the same mean and variance. Therefore a histogram bin in which the number of samples  $n_i$  is greater than three standard deviations from the mean ( $|n_i - m_i| > 3\sigma_i$ ) might be considered statistically unlikely, suggesting the hypothesized known distribution is not representative of the sample data set.



## Coherent Change Detection: Theoretical Description and Experimental Results

Mark Preiss and Nicholas J. S. Stacy

Number of Copies

**DEFENCE ORGANISATION****Task Sponsor**

DGICD	1 (printed)
DGAD	1 (printed)
DD-ES	1 (printed)
DD-MUAV	1 (printed)

**S&T Program**

Chief Defence Scientist	1
Deputy Chief Defence Scientist Policy	1
AS Science Corporate Management	1
Director General Science Policy Development	1
Counsellor, Defence Science, London	Doc Data Sheet
Counsellor, Defence Science, Washington	Doc Data Sheet
Scientific Adviser Joint	1
Navy Scientific Adviser	Doc Data Sheet and Dist List
Scientific Adviser, Army	Doc Data Sheet and Dist List
Air Force Scientific Adviser	Doc Data Sheet and Exec Summ
Scientific Adviser to the DMO	Doc Data Sheet and Dist List

**Information Sciences Laboratory**

Chief, Intelligence, Surveillance and Reconnaissance Division	1
Research Leader, Imagery Systems	1
Head, Imaging Radar Systems Group	1 (printed)
Dr Nick J. S. Stacy	1 (printed)
Dr Mark Preiss	2 (printed)
Dr Tim Payne	1

**Platform Sciences Laboratory**

Deputy Chief Defence Scientist Aerospace, PSL	Doc Data Sheet and Exec Summ
David Cox	1

**Systems Sciences Laboratory**

Chief, Electronic Warfare and Radar Division	1
--	---

Research Leader, Microwave Radar	1
Dr Brett Haywood	1
Dr Paul Berry	1 (printed)
Dr Desmond Yau	1
<b>DSTO Library and Archives</b>	
Library, Edinburgh	1
Defence Archives	1
<b>Capability Development Group</b>	
Director General Maritime Development	1
Director General Capability and Plans	Doc Data Sheet
Assistant Secretary Investment Analysis	Doc Data Sheet
Director Capability Plans and Programming	Doc Data Sheet
Director General Australian Defence Simulation Office	Doc Data Sheet
<b>Chief Information Officer Group</b>	
Head Information Capability Management Division	Doc Data Sheet
AS Information Strategy and Futures	Doc Data Sheet
Director General Information Services	Doc Data Sheet
<b>Strategy Group</b>	
Director General Military Strategy	Doc Data Sheet
Assistant Secretary Governance and Counter-Proliferation	Doc Data Sheet
<b>Navy</b>	
Director General Navy Capability, Performance and Plans, Navy Headquarters	Doc Data Sheet
Director General Navy Strategic Policy and Futures, Navy Headquarters	Doc Data Sheet
Deputy Director (Operations) Maritime Operational Analysis Centre, Building 89/90, Garden Island, Sydney	} Doc Data Sheet and Dist List
Deputy Director (Analysis) Maritime Operational Analysis Centre, Building 89/90, Garden Island, Sydney	
<b>Army</b>	
SO (Science), Deployable Joint Force Headquarters (DJFHQ)(L), Enoggera QLD	Doc Data Sheet
SO (Science), Land Headquarters (LHQ), Victoria Barracks, NSW	Doc Data Sheet and Exec Summ
<b>Air Force</b>	
SO (SCIENCE), Headquarters Air Combat Group, RAAF Base Williamtown	Doc Data Sheet and Exec Summ
SO (CD-PROJECTS), Headquarters Surveillance and Response Group, RAAF Base Williamtown	1

Khan Sharp, Aerospace Development, Russell Offices	1
--	---

### **Joint Operations Command**

Director General Joint Operations	Doc Data Sheet
Chief of Staff Headquarters Joint Operation Command	Doc Data Sheet
Commandant, ADF Warfare Centre	Doc Data Sheet
Director General Strategic Logistics	Doc Data Sheet
COS Australian Defence College	Doc Data Sheet

### **Intelligence and Security Group**

Assistant Secretary Concepts, Capabilities and Resources	1
DGSTA, Defence Intelligence Organisation	1
Manager, Information Centre, Defence Intelligence Organisation	1
Assistant Secretary Capability Provisioning, DSD	1
Director Advanced Capabilities, DIGO	1

### **Defence Materiel Organisation**

Deputy CEO, DMO	Doc Data Sheet
Head Aerospace Systems Division	1
Head Maritime Systems Division	Doc Data Sheet
CDR Joint Logistics Command	Doc Data Sheet
Program Manager Air Warfare Destroyer	Doc Data Sheet
GWEO-DDP	Doc Data Sheet

### **INTERNATIONAL DEFENCE INFORMATION CENTRES**

US - Defense Technical Information Center	1
UK - DSTL Knowledge Services	1
Canada - Defence Research Directorate R&D Knowledge and Information Management (DRDKIM)	1
NZ - Defence Information Centre	1

### **SPARES**

DSTO Edinburgh Library	5 (printed)
------------------------	-------------

**Total number of copies: printed 14, pdf 28**

<b>DEFENCE SCIENCE AND TECHNOLOGY ORGANISATION DOCUMENT CONTROL DATA</b>				1. CAVEAT/PRIVACY MARKING	
2. TITLE Coherent Change Detection: Theoretical Description and Experimental Results			3. SECURITY CLASSIFICATION Document (U) Title (U) Abstract (U)		
4. AUTHORS Mark Preiss and Nicholas J. S. Stacy			5. CORPORATE AUTHOR Defence Science and Technology Organisation PO Box 1500 Edinburgh, South Australia 5111, Australia		
6a. DSTO NUMBER DSTO-TR-1851		6b. AR NUMBER 013-634		6c. TYPE OF REPORT Technical Report	
7. DOCUMENT DATE August, 2006					
8. FILE NUMBER 2006/1018819/1		9. TASK NUMBER JTW04/002		10. SPONSOR DGICD	
11. No OF PAGES 100		12. No OF REFS 53			
13. URL OF ELECTRONIC VERSION <a href="http://www.dsto.defence.gov.au/corporate/reports/DSTO-TR-1851.pdf">http://www.dsto.defence.gov.au/corporate/reports/DSTO-TR-1851.pdf</a>			14. RELEASE AUTHORITY Chief, Intelligence, Surveillance and Reconnaissance Division		
15. SECONDARY RELEASE STATEMENT OF THIS DOCUMENT <i>Approved For Public Release</i> <small>OVERSEAS ENQUIRIES OUTSIDE STATED LIMITATIONS SHOULD BE REFERRED THROUGH DOCUMENT EXCHANGE, PO BOX 1500, EDINBURGH, SOUTH AUSTRALIA 5111</small>					
16. DELIBERATE ANNOUNCEMENT No Limitations					
17. CITATION IN OTHER DOCUMENTS No Limitations					
18. DSTO RESEARCH LIBRARY THESAURUS Synthetic aperture radar Interferometry Radar detection Ingara Radar surveillance					
19. ABSTRACT  This report investigates techniques for detecting fine scale scene changes using repeat pass Synthetic Aperture Radar (SAR) imagery. As SAR is a coherent imaging system two forms of change detection may be considered, namely incoherent and coherent change detection. Incoherent change detection identifies changes in the mean backscatter power of a scene typically via an average intensity ratio change statistic. Coherent change detection on the other hand, identifies changes in both the amplitude and phase of the transduced imagery using the sample coherence change statistic. Coherent change detection thus has the potential to detect very subtle scene changes to the sub-resolution cell scattering structure that may be undetectable using incoherent techniques. The repeat pass SAR imagery however, must be acquired and processed interferometrically. This report examines the processing steps required to form a coherent image pair and describes an interferometric spotlight SAR processor for processing repeat pass collections acquired with DSTO Ingara X-band SAR. The detection performance of the commonly used average intensity ratio and sample coherence change statistics are provided as well as the performance of a recently proposed log likelihood change statistic. The three change statistics are applied to experimental repeat pass SAR data to demonstrate the relative performance of the change statistics.					